Dynamics of microcavity polaritons at the non-linear regime crossover

Dario Ballarini

Departamento de Física de Materiales

Universidad Autónoma de Madrid

Dissertation submitted for the degree of Doctor of Philosophy at

Universidad Autónoma de Madrid

Thesis Supervisor: Luis Viña

Madrid, October 2008

Acknowledgments

Many people helped me in the work presented in this thesis, and I would like to explicitly express my gratitude to all of them. First of all, my gratitude to Luis Viña, who nicely received me in Madrid and introduced me through the physics of semiconductor microcavities, and a special thank to the members of the ultrafast spectroscopy group: Lola, Alberto y Daniele.

It is a pleasure to mention all the people who, day by day, have shared with me these four years: Veronica, Dipankar, Edgardo, Sne, Fabrice, Julien, Carmen, Kike, Ramón, Eva, Olga, Elena and Fabrice.

The experiments have been realized with the irreplaceable help of Elias, Emilio, Manolo, Valentín and Andrés.

I would like to acknowledge Pepe Calleja and Carlos Tejedor for the constant helpfulness and care.

Last but not least, I have to acknowledge Regis Andrés, Maurice Skolnick and Jaqueline Bloch, who grew and provided the sample used for these experiments.

List of publications

Quantum-fluid dynamics of microcavity polaritons

A. Amo, D. Sanvitto, D. Ballarini, F.P. Laussy, E. del Valle, M.D. Martin, A. Lemaitre, J. Bloch, D.N. Krizhanovskii, M.S. Skolnick, C. Tejedor, L. Vina

Nature (submitted)(arXiv:0711.1539v2)

Observation of long-lived polariton states in semiconductor microcavities across the parametric threshold

D. Ballarini, D. Sanvitto, A. Amo, L. Viña, M. Wouters, I. Carusotto, A. Lemaitre, J. Bloch

Phys. Rev. Lett. (submitted) ()

Optically-induced ultrafast quenching of the semiconductor quantum well luminescence

A. Amo, D. Ballarini, D. Sanvitto, E. Kozhemyakina, L. Viña, A. Lemaître, D. Bajoni, J. Bloch

Appl. Phys. Lett. **92**, 061912 (2008)

Exciton warming in III-V microcavities: probe for polariton relaxation process

A. Amo, D. Ballarini, D. Sanvitto, E. Kozhemyakina, L. Viña, M. S. Skolnick, J. S. Roberts

Superlattices and Microstructures **43**, 449 (2008)

Ultrafast tailoring of the exciton distribution in quantum wells

A. Amo, D. Ballarini, E. Kozhemyakina, D. Sanvitto, L. Klopotowski, L. Viña, D. Bajoni, J. Bloch, M. S. Skolnick, J. S. Roberts

Phys. Stat. Sol. (b) **245**, 1064 (2008)

Spatial distribution of strong and weak coupled exciton–polaritons in semiconductor microcavities

D. Ballarini, A. Amo, D. Sanvitto, L. Viña, M. Skolnick and J. Roberts

Physica E: Low-dimensional Systems and Nanostructures **40**, 2049 (2008)

Polariton and spin dynamics in semiconductor microcavities under non-resonant excitation

M. D. Martín, G. Aichmayr, A. Amo, D. Ballarini, Ł. Kłopotowski and L. Viña

J. Phys.: Condens. Matter **19**, 295204 (2007)

Transition from the strong- to the weak-coupling regime in semiconductor microcavities: polarization dependence

D. Ballarini, A. Amo, L. Viña, D. Sanvitto, M.S. Skolnick, J.S. Roberts

Appl. Phys. Lett. **90**, 201905 (2007).

Spin-Dependent Strong- to Weak-Coupling Transition in Semiconductor Microcavities

D. Ballarini, A. Amo, M.D. Martin, L. Viña, D. Sanvitto, M.S. Skolnick and J.S. Roberts

AIP Conference Proceedings **893**, 1153 (2007). Edit. W. Jantsch and F. Schäffler.

Using Phonons to Populate the Bottom of the Polariton Dispersion Relation

M. D. Martín, D. Ballarini, A. Amo, L. Viña, and R. André

AIP Conference Proceedings **893,** 1139 (2007). Edit. W. Jantsch and F. Schäffler.

Spin-dependent coexistence of weakly coupled and strongly coupled modes in semiconductor microcavities

D. Ballarini, A. Amo, M.D. Martin, L. Viña, D. Sanvitto, M.S. Skolnick and J.S.Roberts

Superlattices and Microstructures **41**, 321 (2007)

Dynamics of polaritons resonantly created at the upper polariton branch

M.D. Martín, D. Ballarini, A. Amo, L. Viña and R. André

Superlattices and Microstructures **41**, 328 (2007)

Photoluminescence of "dark" excitons in CdMnTe quantum well, embedded in a microcavity

A. Brunetti, M. Vladimirova, D. Scalbert, R. André, D. Ballarini, A. Amo, M.D. Martin and L. Viña

Superlattices and Microstructures **41**, 386 (2007)

Angular Switching of the Linear Polarization in InGaAs Microcavities.

A. Amo, M. D. Martín, D. Ballarini, L. Viña, D. Sanvitto, M. S. Skolnick and J. S. Roberts

Physica Status Solidi (c) **2**, 3868 (2005).

Striking dynamics of II-VI microcavity polaritons after linearly polarized excitation.

M. D. Martín, D. Ballarini, A. Amo, . Kopotowsi, L. Viña, A. V. Kavokin, and R. André

Physica Status Solidi (c) **2**, 3880 (2005).

Contents

Chapter 1

Introduction

Semiconductor microcavities have been designed to greatly enhance the light-matter interaction strength confining both the electromagnetic field and the electronic excitations in one direction. These structures offer an ideal system in which to study the interface between quantum optics, strong coupling, spontaneous coherence and quantum condensation.

Due to their dual light-matter nature, exciton-polaritons can be manipulated and studied through their light component, and have an effective interaction through their matter component.

The recent experimental and theoretical research in this field has been oriented into two main guidelines: firstly, the resonant pumping scheme has been motivated by the search for all-optical ultrafast switchers and amplifiers; the other direction is the non-resonant pumping scheme, aimed to the realization of a polariton laser.

Unlike many other examples of strong coupling in quantum optics, planar microcavities present a continuum of strongly coupled modes, allowing polaritons to be treated with the statistical mechanics methods of interacting bosons. Besides of the possible future applications, microcavities provide the unique possibility to investigate quantum effects, such as superfluidity and condensation, in solid-state semiconductor systems. This would not be possible, for example, in the case of quantum dots embedded in semiconductor microcavities,(1) where the strong coupling is obtained with a single excitonic resonance. Strong coupling with a single quantum-dot excitons has been realized in photonic crystal,(2, 3) micropillars,(4) and microdiscs.(5)

A closely related area of research is the strong coupling with confinement of photons in more than one direction. Besides the experiments on quantum dots and quantum well in planar microcavities, strong coupling between quantum well and

photons mode confined in two or three directions has been performed, producing 1-dimensional and 0-dimensional microcavities.(6, 7)

A number of reviews have been written on the subject of microcavity polaritons: in Refs. (8-10), the linear properties have been addressed, while Refs. (11, 12) deal with nonlinear properties of polaritons. In addition, two books (13, 14) and two special issue (15, 16) have also been published.

The aim of this work is to investigate the many-body properties of semiconductor planar microcavities both under resonant and non-resonant excitation. In particular, the optical properties of polaritons and their dynamics are studied by means of time-resolved photoluminescence. In this technique, the system is excited by an optical pulse and the emitted light dynamics is recorded and analyzed.

Chapter 2 presents a brief introduction to the fundamental aspects of semiconductor microcavities. In these heterostructures, the continuum of the available electromagnetic modes in vacuum is reduced to a discrete number of modes inside the cavity. If one of those cavity modes is close to resonance with an energy level of the excitons, which are confined in the quantum well embedded in the structure, light-matter interactions are expected to be strongly amplified. The theoretical framework necessary to the study of the strong coupling between exciton and photon is provided, and the dispersion relations of exciton-polaritons in the reciprocal space are described. The spin properties of polaritons are also presented, because they will be addressed in Chapter 4 and Chapter 5.

In Chapter 3 are illustrated the samples and the experimental techniques employed in this work. The experiments described in Chapter 4 and Chapter 5 are performed in a conventional time-resolved photoluminescence setup, employing a streak camera and a spectrograph to obtain time and energy resolution. Experiments of Chapter 6 are performed with an original configuration of the experimental setup, which allows for a more complete analysis of the photoluminescence properties.

Chapter 4 and 5 are devoted to non-resonant excitation-configuration experiments, while Chapter 6 treats the resonant case.

In Chapter 4 the polarization properties of polariton emission under non-resonant excitation are presented. The spin relaxation in semiconductor microcavities is strongly connected with the energy relaxation of polaritons, and thus results strongly dependent on the detuning between cavity and excitonic modes and on the density of polaritons in the system. The spin relaxation models employed in the literature to explain the complex polarization behavior of polaritons under non-resonant excitation are presented. A high linear polarization degree, in particular, is expected to be related with the formation of a macroscopic coherent phase of polaritons in the ground state. In our experiment we demonstrate that the linear

polarization is pinned to one of the crystallographic axis and can be conserved even under fast relaxation processes.

In Chapter 5 the transition from the strong- to the weak-coupling regime with increasing the polariton density, or, which is the same, the excitation power, is studied. In particular, the strong to weak coupling transition is analyzed taking into account the polarization properties of the emission with respect to the polarization of the exciting beam. It results that under non-resonant, circularly polarized excitation, the co- and cross-polarized polariton populations undergo a transition to the weak-coupling regime at different powers: the transition power threshold, for each spin population, directly depends on the density of polaritons with the same spin. The importance of the finite size of the excitation spot and the spatial distribution of the photoluminescence are also stressed.

In Chapter 6 we describe experimental and theoretical results on the resonant excitation of polaritons. The optical parametric amplification (OPA) and oscillation (OPO) processes are presented. The non-linear optical properties of polaritons are directly related to the effective interaction between their matter components, and the polariton parametric scattering is described. In this Chapter (6), is also discussed the relation between the stimulated scattering process under resonant and non resonant conditions and the coherence properties in both cases. The main objective of Chapter 6 is to study the response of the system in its stationary state to a weak probe perturbation. A strong slowing down of the dynamics is observed as the excitation power approaches the threshold for the switching-on of the optical parametric oscillations. The decay time can become orders of magnitude longer than the typical life time of polaritons. This observation suggests the possibility of investigating the polariton dynamics beyond the limits imposed by the intrinsic polariton life time. Good agreement between the experimental results and the theoretical model based on the generalized polariton Gross-Pitaevskii equation is found. In particular, the changes in the polariton dynamics are related with the excitation spectrum on the top of a high density phase of polaritons and support the theoretical description of polariton OPO as an example of spontaneous symmetry breaking.

Bibliography:

[1] G. Ramon, U. Mizrahi, N. Akopian, S. Braitbart, D. Gershoni, T. L. Reinecke, B. D. Gerardot, and P. M. Petroff. *Emission characteristics of quantum dots in planar microcavities*. Phys. Rev. B **73,** 205330 (2006).

[2] T. Yoshie, A. Scherer, J. Hendrickson, G. Khitrova, H. M. Gibbs, G. Rupper, C. Ell, O. B. Shchekin, and D. G. Deppe. *Vacuum Rabi splitting with single quantum dot in a photonic crystal nanocavity*. Nature **432,** 200 (2004).

[3] A. Badolato, K. Hennessy, M. Atatüre, J. Dreiser, E. Hu, P. M. Petroff, and A. Imamoglu. *Deterministic Coupling of Single Quantum Dots to Single Nanocavity Modes*. Science **308,** 1158 (2005).

[4] J. P. Reithmaier, G. Sek, A. Löffler, C. Hofmann, S. Kuhn, S. Reitzenstein, L. V. Keldysh, V. D. Kulakovskii, T. L. Reinecke, and A. Forchel. *Strong coupling in a single quantum dot-semiconductor microcavity system*. Nature **432,** 197 (2004).

[5] E. Peter, P. Senellart, D. Martrou, A. Lemaître, J. Hours, J. M. Gérard, and J. Bloch. *Exciton-Photon Strong-Coupling Regime for a Single Quantum Dot Embedded in a Microcavity*. Phys. Rev. Lett. **95,** 067401 (2005).

[6] G. Dasbach, C. Diederichs, J. Tignon, C. Ciuti, P. Roussignol, C. Delalande, M. Bayer, and A. Forchel. *Polarization inversion via parametric scattering in quasi-one-dimensional microcavities*. Phys. Rev. B **71,** 161308 (2005).

[7] W. Langbein, and J. M. Hvam. *Elastic Scattering Dynamics of Cavity Polaritons: Evidence for Time-Energy Uncertainty and Polariton Localization*. Physical Review Letters **88,** 047401 (2002).

[8] M. S. Skolnick, T. A. Fisher, and D. M. Whittaker. *Strong coupling phenomena in quantum microcavity structures*. Semicond. Sci.Technol. **13,** 645 (1998).

[9] V. Savona, C. Piermarocchi, A. Quattropani, P. Schwendimann, and F. Tassone. *Optical properties of microcavity polaritons*. Phase Transitions **68,** 169 (1999).

[10] V. Savona, L. C. Andreani, P. Schwendimann, and A. Quattropani. *Quantum well exciton in semiconductor microcavities: unified treatment of weak and strong coupling regimes*. Solid State Commun. **93,** 733 (1995).

[11] G. Khitrova, H. M. Gibbs, F. Jahnke, M. Kira, and S. W. Koch. *Nonlinear optics of normal-mode-coupling semiconductor microcavities*. Rev. Mod. Phys. **71,** 1591 (1999).

[12] C. Ciuti, P. Schwendimann, and A. Quattropani. *Theory of polariton parametric interactions in semiconductor microcavities*. Semicond. Sci. Technol. **18,** S279 (2003).

[13] Y. Yamamoto, F. Tassone, and H. Cao. *Semiconductor cavity quantum electrodynamics*. (Springer tracts in Modern Physics, volume 169) (Berlin, Springer) (2000).

[14] A. V. Kavokin, and G. Malpuech. *Cavity Polaritons*. (Thin Film and Nanostructures, volume 32) (New York, Elsevier) (2003).

[15] J. J. Baumberg, and L. Viña (editors). *Special Issue on microcavities*. volume **18** (10) of Semiconductor Science and Technology. (2003).

[16] B. Deveaud. *Special Issue: Physics of Semiconductor Microcavities*. volume **242** (11) of Phys. Stat. Sol. (b) (2005).

Introducción

Las microcavidades de semiconductores se diseñan para incrementar fuertemente la interacción luz-materia por medio del confinamiento del campo electromagnético y de las excitaciones electrónicas en una dirección. Estas estructuras ofrecen un sistema ideal para el estudio de la interconexión entre la óptica cuántica, el acoplamiento fuerte, la coherencia espontánea y la condensación cuántica.

Debido a la naturaleza dual luz-materia, los polaritons de excitones pueden ser manipulados y estudiados a través de su componente lumínica, y pueden tener una interacción efectiva a través de su componente material.

Los experimentos recientes y la investigación teórica en este campo se ha orientado en dos direcciones principales: en primer lugar, el esquema de bombeo resonante ha sido motivada por la búsqueda de interruptores y amplificadores ultrarrápidos totalmente ópticos; la otra dirección es el esquema de bombeo no-resonante, dirigido a la consecución de un láser polaritónico.

De un modo diferente a otros ejemplos de acoplamiento fuerte en óptica cuántica, las microcavidades planares presentan un continuo de modos acoplados fuertemente, permitiendo que se pueda tratar a los polaritones con los métodos de la mecánica estadística de bosones interaccionantes. A parte de las posibles futuras aplicaciones, las microcavidades ofrecen la posibilidad única de investigar efectos cuánticos, tales como superfluidez y condensación, en sistemas de semiconductores de estado sólido. Esto no sería posible, por ejemplo, en el caso de puntos cuánticos inmersos en microcavidades semiconductoras,(1) donde el acoplamiento fuerte se obtiene con una resonancia excitónica única. El acoplamiento fuerte con excitones en puntos cuánticos individuales se ha obtenido en cristales fotónicos,(2, 3) micropilares,(4) y microdiscos.(5)

Un área de investigación muy relacionada con lo que se ha mencionado anteriormente es el acoplamiento fuerte con confinamiento de fotones en más de una dirección. Además de en los experimentos en puntos cuánticos y pozos cuánticos en microcavidades planares, se ha obtenido también el acoplamiento fuerte entre pozos

cuánticos y modos fotónicos confinados en dos o tres direcciones, produciendo microcavidades uni-dimensionales o de cero-dimensiones.(6, 7)

Hasta la fecha se han escrito numerosos artículos de revisión en el tema de polaritons de microcavidades: en Refs. (8-10) se han tratado las propiedades lineales, mientras que las Refs. (11, 12) tratan de las propiedades no-lineales de los polaritons. Además se han publicado dos libros (13, 14) y dos volúmenes especiales de revistas científicas (15, 16).

La meta de este trabajo es la investigación de las propiedades de muchos cuerpos de microcavidades planares de semiconductores tanto bajo condiciones de excitación resonante como no-resonante. En particular, las propiedades ópticas de los polaritones y su dinámica se estudian por medio de fotoluminiscencia resuelta en tiempo. Con esta técnica, el sistema se estudia por un pulso óptico y se detecta y analiza la dinámica de la luz emitida.

El Capítulo 2 presenta un introducción breve a los aspectos fundamentales de las microcavidades de semiconductores. En estas heteroestructuras, el continuo de los modos electromagnéticos disponibles en el vacío se reduce a un número discreto de modos dentro de la cavidad. Si uno de estos modos de la cavidad está próximo a una resonancia con un nivel energético de excitones, que están confinados en los pozos cuánticos embebidos en la estructura, es esperable que las interacciones luz-materia se amplifiquen fuertemente. Se presenta el cuerpo teórico necesario para el estudio del acoplamiento fuerte entre excitones y fotones, y se describen las relaciones de dispersión de los polaritones excitónicos. También se tratan las propiedades de espín de los polaritones, ya que éstas se necesitarán en los Capítulos 4 y 5.

En el Capítulo 3 se describen las muestras y las técnicas experimentales empleadas en este trabajo. Los experimentos descritos en los Capítulos 4 y 5 se realizan con un sistema de fotoluminiscencia resuelta en tiempo convencional, empleando una cámara de impulso y un espectrógrafo para obtener la resolución temporal y en energía. Los experimentos del Capítulo 6 se llevan a cabo con una configuración original del sistema experimental, que permite un análisis más completo de las propiedades fotoluminiscentes.

Los Capítulos 4 y 5 se dedican a experimentos en una configuración de excitación no-resonante, mientras que el Capítulo 6 trata el caso resonante.

En el Capítulo 4 se presentan las propiedades de polarización de la emisión de polaritones bajo excitación no-resonante. La relajación de spin en microcavidades semiconductoras está fuertemente conectada con la relajación de energía de los polaritones y, por tanto depende fuertemente de la sintonización entre los modos fotónicos y excitónicos en la cavidad y de la densidad de polaritones en el sistema. Se presentan los modelos de relajación de spin empleados en la literatura para explicar los comportamientos complejos de la polarización de los polaritones bajo excitación

no-resonante. En particular, se espera que la existencia de un grado alto de polarización lineal esté relacionado con la formación de una fase macroscópica coherente de polaritones en su estado fundamental. En nuestros experimentos demostramos que la polarización lineal se ancla a uno de los ejes cristalográficos y puede conservarse incluso bajo procesos de relajación veloces.

En el Capítulo 5 se estudia la transición del régimen de acoplamiento fuerte al de acoplamiento débil al aumentar la densidad de polaritones, o, lo que es lo mismo, la potencia de excitación. En particular, se analiza la transición del acoplamiento fuerte al débil teniendo en cuenta las propiedades de polarización de la emisión con respecto a la polarización del haz de excitación. Se obtiene que bajo excitación no-resonante y polarizada circularmente, las poblaciones de polaritones co-polarizados y contra-polarizados sufren una transición al acoplamiento débil a diferentes potencias de excitación: el umbral de potencia para la transición, para cada población de spin, depende directamente de la densidad de polaritones con el mismo spin. Se destaca también la importancia del tamaño finito del haz de excitación y la distribución espacial de la fotoluminiscencia.

En el Capítulo 6 se describen resultados experimentales y teóricos bajo excitación resonante de polaritones. Se presentan los procesos de amplificación paramétrica óptica (en inglés, optical parametric amplification–OPA–) y oscilación paramétrica óptica (en inglés, optical parametric oscillation–OPO–). Se describe la relación directa entre las propiedades ópticas no-lineales de los polaritons y la interacción efectiva entre sus componentes materiales, y los procesos de “scattering” paramétrico de polaritones. En este Capítulo también se discute la relación entre los procesos de “scattering” estimulado bajo condiciones de excitación resonante y no-resonante y las propiedades de coherencia en ambos casos. El objetivo principal del Capítulo 6 es el estudio de la respuesta del sistema en su estado estacionario a una débil prueba perturbativa. Se obtiene una fuerte ralentización de la dinámica cuando la potencia de excitación se aproxima al umbral para el encendido de las oscilaciones ópticas paramétricas. El tiempo de decaimiento se vuelve órdenes de magnitud más largo que el tiempo de vida típico de los polaritones. Esta observación sugiere la posibilidad de investigar la dinámica de los polaritones más allá de los límites impuestos por el tiempo de vida intrínseco de los polaritones. Se presenta un buen acuerdo entre los resultados experimentales y un modelo teórico basado en la ecuación generalizada de Gross-Pitaevskii para polaritones. En particular, se muestra que los cambios en la dinámica de los polaritons están relacionados con el espectro de excitación en una fase de polaritones de alta densidad y se justifica la descripción teórica de un OPO de polaritones como un ejemplo de rotura de simetría espontánea.

Bibliography:

[1] G. Ramon, U. Mizrahi, N. Akopian, S. Braitbart, D. Gershoni, T. L. Reinecke, B. D. Gerardot, and P. M. Petroff. *Emission characteristics of quantum dots in planar microcavities*. Phys. Rev. B **73,** 205330 (2006).

[2] T. Yoshie, A. Scherer, J. Hendrickson, G. Khitrova, H. M. Gibbs, G. Rupper, C. Ell, O. B. Shchekin, and D. G. Deppe. *Vacuum Rabi splitting with single quantum dot in a photonic crystal nanocavity*. Nature **432,** 200 (2004).

[3] A. Badolato, K. Hennessy, M. Atatüre, J. Dreiser, E. Hu, P. M. Petroff, and A. Imamoglu. *Deterministic Coupling of Single Quantum Dots to Single Nanocavity Modes*. Science **308,** 1158 (2005).

[4] J. P. Reithmaier, G. Sek, A. Löffler, C. Hofmann, S. Kuhn, S. Reitzenstein, L. V. Keldysh, V. D. Kulakovskii, T. L. Reinecke, and A. Forchel. *Strong coupling in a single quantum dot-semiconductor microcavity system*. Nature **432,** 197 (2004).

[5] E. Peter, P. Senellart, D. Martrou, A. Lemaître, J. Hours, J. M. Gérard, and J. Bloch. *Exciton-Photon Strong-Coupling Regime for a Single Quantum Dot Embedded in a Microcavity*. Phys. Rev. Lett. **95,** 067401 (2005).

[6] G. Dasbach, C. Diederichs, J. Tignon, C. Ciuti, P. Roussignol, C. Delalande, M. Bayer, and A. Forchel. *Polarization inversion via parametric scattering in quasi-one-dimensional microcavities*. Phys. Rev. B **71,** 161308 (2005).

[7] W. Langbein, and J. M. Hvam. *Elastic Scattering Dynamics of Cavity Polaritons: Evidence for Time-Energy Uncertainty and Polariton Localization*. Physical Review Letters **88,** 047401 (2002).

[8] M. S. Skolnick, T. A. Fisher, and D. M. Whittaker. *Strong coupling phenomena in quantum microcavity structures*. Semicond. Sci.Technol. **13,** 645 (1998).

[9] V. Savona, C. Piermarocchi, A. Quattropani, P. Schwendimann, and F. Tassone. *Optical properties of microcavity polaritons*. Phase Transitions **68,** 169 (1999).

[10] V. Savona, L. C. Andreani, P. Schwendimann, and A. Quattropani. *Quantum well exciton in semiconductor microcavities: unified treatment of weak and strong coupling regimes*. Solid State Commun. **93,** 733 (1995).

[11] G. Khitrova, H. M. Gibbs, F. Jahnke, M. Kira, and S. W. Koch. *Nonlinear optics of normal-mode-coupling semiconductor microcavities*. Rev. Mod. Phys. **71,** 1591 (1999).

[12] C. Ciuti, P. Schwendimann, and A. Quattropani. *Theory of polariton parametric interactions in semiconductor microcavities*. Semicond. Sci. Technol. **18,** S279 (2003).

[13] Y. Yamamoto, F. Tassone, and H. Cao. *Semiconductor cavity quantum electrodynamics*. (Springer tracts in Modern Physics, volume 169) (Berlin, Springer) (2000).

[14] A. V. Kavokin, and G. Malpuech. *Cavity Polaritons*. (Thin Film and Nanostructures, volume 32) (New York, Elsevier) (2003).

[15] J. J. Baumberg, and L. Viña (editors). *Special Issue on microcavities*. volume **18** (10) of Semiconductor Science and Technology. (2003).

[16] B. Deveaud. *Special Issue: Physics of Semiconductor Microcavities*. volume **242** (11) of Phys. Stat. Sol. (b) (2005).

Chapter 2

Semiconductor microcavities

A semiconductor planar microcavity is a structure formed by high reflecting dielectric mirrors (Distributed Bragg Reflectors, DBR) on the two sides of a spacer layer, of length L_C, with embedded quantum wells (QWs). Such a structure constitutes a high finesse Fabry-Perot resonator where the interaction between the confined photon modes and the QW excitons can be strongly enhanced if L_C is properly tuned. In this Chapter, we will briefly describe the essential properties of semiconductor microcavities. Several works can be found in the literature on this subject, which attend many specific aspects of the theoretical basis in this field.(1-5) The main interest in semiconductor microcavities is due to their unique optical properties, described by the normal mode coupling between exciton and photon modes (exciton-polaritons). (2, 6-8) We will illustrate in this Chapter the main basic properties of exciton-polaritons following a linear semiclassical approach.(9)

2.1 – Distributed Bragg Reflector and photon modes in the cavity

A DBR is composed by alternate layers of two dielectric materials with different indexes of refraction; usually, semiconductors with high refraction index (~ 3.5) are employed. A DBR presents an enhanced reflectivity for a range of frequencies, called the stop band, which depends on the number of paired layers and on their thickness. The central wavelength λ of the high reflectivity region (stop band) is determined by four times the optical thickness of each material: an incoming light field of wavelength λ is reflected by the DBR structure if the alternating layers are grown with identical optical thickness of $\lambda/4$. An approximate expression, valid for an high number N of the

dielectric layer pairs which compose the DBR, for the normal incidence reflectivity R, where $R = |r(\omega)|^2$, is given by:(10)

$$R \approx 1 - 4\frac{n_{out}}{n_{sub}}\left(\frac{n_1}{n_2}\right)^{2N} \quad 2.1$$

where n_{out} and n_{sub} are the index of refraction of the external medium and of the substrate, and n_1, n_2 are the refraction indexes of the two alternate materials. As N is increased, both the reflectivity and the stop band region around λ are increased.

The penetration depth of the electromagnetic field inside the mirror, L_{DBR}, is given by:

$$L_{DBR} = \frac{\lambda}{2} - \frac{n_1 n_2}{n_{sub}(n_2 - n_1)}. \quad 2.2$$

A semiconductor microcavity is formed by sandwiching a cavity spacer of length L_C, usually an additional semiconductor, between two of such DBRs, resulting in a Fabry-Perot resonator with a wide stop band in which high transmission peaks originates at the energy of the photon modes confined in the cavity. If the central wavelength of the stop band is equal to the length of the cavity spacer, L_C, the condition for constructive interference in a round trip is given by

$$\left(\frac{\omega^2}{c^2}n_{cav}^2 - k_{\|}^2\right)^{\frac{1}{2}} L_{eff} = M\pi, \quad 2.3$$

where $M = 1,2,3, \ldots$, L_{eff} is the effective cavity length $\left(L_{eff} = L_C + L_{DBR}\right)$ and n_{cav} is the index of refraction of the cavity spacer. The term in the parenthesis is the component of the photon wavevector $\boldsymbol{k}$ normal to the plane of the mirrors (z axis):

$$k_z = \left(\frac{\omega^2}{c^2}n_{cav}^2 - k_{\|}^2\right)^{\frac{1}{2}}. \quad 2.4$$

The photon modes are confined in the z direction, and the allowed momenta are quantized along this axis. $k_{\|}$ is the photon wavevector parallel to the cavity plane, which can have any value, as the microcavity does not impose any confinement in such plane. At normal incidence, $k_{\|} = 0$, Eq. 2.3 imposes the appearance of cavity modes at wavelengths:

$$\lambda_M = \frac{2n_{cav}L_{eff}}{M}. \quad 2.5$$

The lowest cavity mode corresponds to a wavelength equal to twice the optical length of the effective cavity, $\lambda = 2n_{cav}L_{eff}$. In this way, the mode energy splitting is large enough to disregard any effect of other cavity modes in the optical properties. If we

consider just one of the cavity modes M, the cavity mode presents a dispersion given by:

$$E(k_{\parallel}) = \frac{\hbar c}{n_{cav}}\sqrt{k_{\perp}^2 + k_{\parallel}^2}, \qquad 2.6$$

where $k_{\perp} = n_{cav}\frac{2\pi}{\lambda_M}$ is the confined momentum along the z axis.

$k_{\parallel}$ is related to the angle of incidence ϑ of the photons outside the cavity by:

$$k_{\parallel} = k_{\perp}\tan\left[\sin^{-1}\left(\frac{1}{n_{cav}}\sin\vartheta\right)\right] = n_{cav}\frac{2\pi}{\lambda}\tan\left[\sin^{-1}\left(\frac{1}{n_{cav}}\sin\vartheta\right)\right]. \qquad 2.7$$

If $k_{\parallel} \ll k_{\perp}$, Eq. 2.6 can be expanded to obtain:

$$E(k_{\parallel}) \approx \frac{\hbar c}{n_{cav}}\left(k_z + \frac{1}{2k_z}k_{\parallel}^2\right) \qquad 2.8$$

which gives an effective photon mass $m_{ph} = \frac{2\pi\hbar}{c\lambda_M}$, which is of the order of 10^{-6} the free electron mass, m_0.

The cavity homogeneous linewidth at normal incidence $(k_{\parallel} = 0)$, which determines the life time $\left(\frac{1}{\gamma_C}\right)$ of a photon in the cavity before escaping, is

$$\gamma_C = \frac{c}{2\pi n_{cav}L_{eff}}\frac{1-R}{\sqrt{R}}, \qquad 2.9$$

where R is the reflectivity of the DBRs (assumed symmetric on both side of the cavity).

Therefore, the quality factor Q of the cavity, for the first mode M=1 (the so called $\lambda/2$ cavity), results

$$Q = \frac{\lambda}{\Delta\lambda} = \pi\frac{\sqrt{R}}{1-R}. \qquad 2.10$$

In such structures, the electromagnetic field is strongly enhanced inside the cavity spacer. Following a classical treatment,(2) the amplitude of the electric field in the center of a symmetric $\lambda/2$ microcavity is given by:

$$|F(\omega)|^2 = F_0^2\frac{1-R(\omega)}{\left(1-R(\omega)\right)^2 + 4\sqrt{R(\omega)}sin^2\left[\frac{1}{2}\left(k_zL_c + \phi_r(\omega)\right)\right]}, \qquad 2.11$$

where F_0 is the amplitude of the incoming electric field and the argument of the sine is the phase change in a round trip inside the cavity, with $\phi_r(\omega)$ being the phase of the complex reflectivity $r(\omega)$. Inside the stop band, the phase $\phi_r(\omega)$ has an approximate linear dependence on the angular frequency of the light field given by:

$$\phi_r(\omega) \approx \frac{n_{sub} L_{DBR}}{c}(\omega - \omega_m), \qquad 2.12$$

where ω_m is the frequency of the center of the stop band.

Typical values of the cavity lifetime in real semiconductor microcavities are of the order of $4\ ps$ ($R \approx 0.9982$), which gives an enhancement factor of about 500 for the electric field at the center of the cavity. If a quantum well (QW), or a series of QWs, are embedded inside the cavity spacer, at the positions where the electromagnetic field is enhanced, strong interaction between the QW exciton and the cavity photon can occur, as will be explained in the next section. This light-matter interaction dramatically changes the optical properties of the cavity and represents the main feature of semiconductor microcavities.

A reflectivity spectrum of a typical microcavity is depicted in Fig. 2.1(a). The amplitude of the electric field for a λ cavity with Bragg mirrors of 15 (left) and 21 (right) pair periods is shown in Fig. 2.1(b). Note that due to the boundary conditions imposed by the DBRs, the electromagnetic field inside the cavity is quasi-stationary. A scanning electron microscope image of an actual microcavity is presented in Fig. 2.1(c).

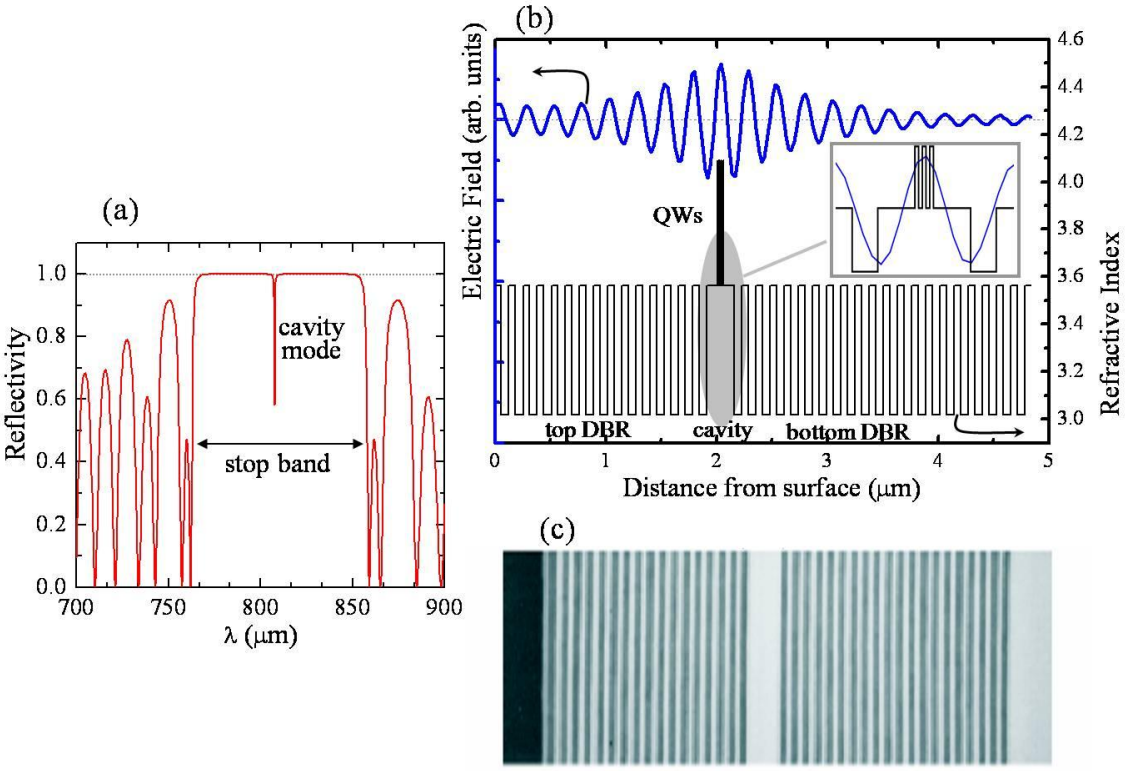

Fig. 2.1: (a) Reflectivity spectrum of a typical microcavity. (b) Black line, right scale: profile of the index of refraction of a λ microcavity. In this case three QWs have been embedded at its center. The surface is on the left side. The growth direction is given by the horizontal axis. Blue line, right scale: electric field of the bare cavity mode. Inset: close up of the cavity spacer. The electric field is maximum at the position of the QWs. (c) Scanning electron microscope image of the cross section of an actual cavity, where both the DBRs and the cavity spacer are clearly seen. The black region on the left side has a size of ~ 225 nm.

2.2 – Semiconductor microcavity and exciton-photon coupling

In a semiconductor, negatively charged electrons in the conduction band and positively charged holes in the valence band are subject to Coulomb attraction: this electron-hole interaction gives rise to bound states, called excitons. Actually, excitons are the lowest elementary excitations of the system which result when all the electronic states are considered. It has been shown that excitons are approximate bosons, and, in interaction with the electromagnetic field, the exciton field behaves as the classical polarization field.(11) The true eigenstates of the system composed by the semiconductor crystal and the electromagnetic field are called exciton-polariton, which are a mixture of exciton and photon. Polaritons constitute the real propagation modes of the electromagnetic field inside a dielectric crystal.

In bulk semiconductors, the polariton optical lifetime is infinite: no photon is really absorbed or emitted, but continuously coupled to an exciton. Interactions with some defects or interfaces of the crystal are required to decouple the polariton mode and to emit a photon from the system. This is the reason for polariton being hardly detected in bulk semiconductor.

If the symmetry of the system is broken in one or more direction, for example consider the 2D confinement of a quantum well, the conservation of momentum only apply in the quantum well plane, and excitons are free to couple to a continuous of states (the density of states of the electromagnetic field in vacuum is flat). In this case the radiative recombination rates is enhanced and can be calculated by the Fermi golden rule, which describe the coupling of a discrete level (exciton) to a continuum (electromagnetic field) in first order perturbation theory. The golden rule is a good approximation when the interaction matrix element between the discrete level and the continuum is small compared with the energy broadening of the continuum modes.

The polaritonic effects are in general negligible, but when the QW is embedded in a microcavity, with a cavity mode resonant with the excitonic transition, strong changes in the optical properties of the system can occur.

We have seen in the previous section how the electromagnetic field can be modified inside a microcavity. In particular, the density of states becomes peaked around the cavity resonance (we consider for sake of simplicity only one cavity mode). Moreover, the dipole matrix element of the golden rule is proportional to the local density of states (product between the density of states and the normalized amplitude of the electromagnetic field at the QW position) and, inside an actual microcavity, the amplitude of the electric field at the energy of the photonic resonance is greatly enhanced at the antinode positions as compared to the value of the field outside the

cavity. Still, the golden rule applies if the width of the cavity mode is larger than the interaction matrix element. This situation is called weak-coupling regime (WC). If, on the contrary, the exciton-photon interaction energy is greater than any homogeneous or inhomogeneous broadening of the bare photon or exciton mode, the system is in the strong-coupling regime and the interaction is no longer described by a purely dissipative process and the Fermi golden rule does not apply. In the strong coupling regime (SC), the energy is exchanged between the exciton and the cavity mode several times, before being dissipated outside the cavity. In both regimes, the polariton formalism provides the most suitable description of the exciton-radiation interaction in microcavities, but it is in the strong coupling regime when the concept of exciton-polariton plays the central role in explaining the optical properties of the system.

In a semiconductor microcavity, a QW with the first excitonic resonance close in energy to the cavity mode is placed at the antinode position of the electromagnetic field inside the cavity. The 2D confinement localizes excitons in the region where the electromagnetic field is stronger, and enhances the exciton oscillator strength with respect to the bulk case; therefore an important light-matter interaction is expected inside the cavity.

In a quantum description, exciton and photon constitute a system of two bosonic oscillators coupled through light-matter interaction, which are described by the following Hamiltonian:

$$H_{pol} = \sum_{k_\parallel} \hbar\omega_c(k_\parallel)\hat{a}^\dagger_{k_\parallel}\hat{a}_{k_\parallel} + \sum_{k_\parallel} \hbar\omega_x(k_\parallel)\hat{B}^\dagger_{k_\parallel}\hat{B}_{k_\parallel} + \sum_{k_\parallel} \hbar\Omega_R\left(\hat{a}^\dagger_{k_\parallel}\hat{B}_{k_\parallel} + \hat{a}_{k_\parallel}\hat{B}^\dagger_{k_\parallel}\right), \quad 2.13$$

where $\hat{B}_{k_\parallel}$, $\hat{B}^\dagger_{k_\parallel}$ $\left(\hat{a}_{k_\parallel}, \hat{a}^\dagger_{k_\parallel}\right)$ are the exciton (photon) annihilation and creation operators with in-plane wave vector $k_\parallel$, $\hbar\omega_{x(c)}(k_\parallel)$ is the in-plane energy dispersion of the excitons (cavity photons) and $\hbar\Omega_R$ is the exciton-photon dipole interaction. In the simplest case of a single QW, Ω_R is given by:

$$\Omega_R^2 = \frac{\left(1+\sqrt{R}\right)^2}{2\sqrt{R}}\frac{c\Gamma_0}{n_{cav}L_{eff}}, \quad 2.14$$

where Γ_0 is the exciton radiative lifetime in the absence of the cavity and it is proportional to the exciton oscillator strength, f_{exc}^{osc}, as:(12)

$$\Gamma_0 = \frac{1}{4\pi\epsilon_0}\frac{\pi}{n_{cav}}\frac{e^2}{m_0 c}f_{exc}^{osc}, \quad 2.15$$

with ϵ_0 the dielectric constant of the vacuum.

If $k_{\|} \ll k_z$, Ω_R can be considered independent of $k_{\|}$.(7) In the case of N QWs, and assuming no polariton coupling between them, then $\Omega_{\mathrm{R,N}} = \Omega_R\sqrt{N}$.(13, 14)

In the exciton-photon basis, the Hamiltonian 2.13 can be rewritten:

$$H_{pol}(k_{\|}) = \begin{pmatrix} \hbar\omega_c(k_{\|}) & \hbar\Omega_R \\ \hbar\Omega_R & \hbar\omega_x(k_{\|}) \end{pmatrix}. \qquad 2.16$$

Matrix 1.16 can be diagonalized by a transformation into the polariton basis, given by the following polariton operators:

$$\begin{aligned} \hat{p}_{k_{\|}} &= X_{k_{\|}}\hat{B}_{k_{\|}} + C_{k_{\|}}\hat{a}_{k_{\|}} \\ \hat{q}_{k_{\|}} &= -C_{k_{\|}}\hat{B}_{k_{\|}} + X_{k_{\|}}\hat{a}_{k_{\|}}. \end{aligned} \qquad 2.17$$

$\hat{p}_{k_{\|}}$ and $\hat{q}_{k_{\|}}$ are the lower and upper polariton operators, while $X_{k_{\|}}$ and $C_{k_{\|}}$ are the Hopfield coefficient,(11) which weight the photonic and excitonic content of the upper and lower polaritons with a particular in-plane momentum $k_{\|}$.

The eigenenergies E_{LPB} and E_{UPB} correspond respectively to the lower (LPB) and upper (UPB) polariton branch and are given by

$$\begin{aligned} E_{LPB}(k_{\|}) &= \frac{\hbar\omega_c(k_{\|}) + \hbar\omega_x(k_{\|})}{2} \\ &\quad - \frac{1}{2}\sqrt{4\hbar^2\Omega_{\mathrm{R}}^2 + \left[\hbar\omega_c(k_{\|}) - \hbar\omega_x(k_{\|})\right]^2} \\ E_{UPB}(k_{\|}) &= \frac{\hbar\omega_c(k_{\|}) + \hbar\omega_x(k_{\|})}{2} \\ &\quad + \frac{1}{2}\sqrt{4\hbar^2\Omega_{\mathrm{R}}^2 + \left[\hbar\omega_c(k_{\|}) - \hbar\omega_x(k_{\|})\right]^2} \end{aligned} \qquad 2.18$$

The polariton dispersion is defined by 2.18 as a function of $k_{\|}$ and shows a gap, at every $k_{\|}$, between the UPB and the LPB, which depends on the detuning δ, defined as the energy difference at $k_{\|} = 0$ of the bare cavity and exciton mode ($\delta = \hbar\omega_c(0) - \hbar\omega_x(0)$), as shown in Fig. 2.2.

As can be seen from the corresponding Hopfield coefficients (Fig. 2.2), with a proper choice of $k_{\|}$ and δ, both lower and upper polaritons have a 50% exciton and photon component: the polariton states are quantum mixtures of the exciton and photon states. When $\delta \approx 0$, the equal mixture of exciton and photon occurs for $k_{\|} \approx 0$; at this points the energy difference between the UPB and the LPB reaches its minimum. This energy gap, called Rabi splitting, is analogous to the normal mode splitting observed in

atoms inside cavities.(15, 16) The Rabi splitting is the fundamental parameter to characterized the exciton-photon coupling in a microcavity, and is defined precisely from the minimum value of energy difference between the UPB and the LPB, which is obtained at $\delta = 0$:

$$Rabi\ Splitting = E_{UPB}(k_{\parallel} = 0) - E_{LPB}(k_{\parallel} = 0) = 2\hbar\Omega_R \qquad 2.19$$

The exciton-photon coupling term, $\hbar\Omega_R$, and the Rabi splitting are proportional to the square root of the exciton oscillator strength, as follow from Eq. 2.14 and 2.15.

The dispersion relations, near $k_{\parallel} = 0$, can be approximate by a parabolic dispersion (see Eq. 2.8), from which the polariton effective mass can be calculated to be of the order of 10^{-6} the free electron mass m_0. The shape of polariton dispersion, which presents a deep trap in the LPB at $k_{\parallel} = 0$, and its small effective mass play a fundamental role in stimulating the parametric scattering and allowing the Bose-Einstein condensation of polaritons (see Chapter 5 and 6).

In the previous description, only the real part of the dispersion was taken into account: the exciton and cavity homogeneous linewidths were supposed to be vanishing. The cavity homogeneous linewidth is defined in 2.9, while the exciton homogeneous linewidth (γ_x) is the width of the exciton resonance due to dephasing, assuming that no defects are present. Despite the high quality of the heterostructures grown by current epitaxial techniques, interface and composition fluctuations are present in the QWs, and this irregular environment modifies the exciton resonance and determines the inhomogeneous broadening of the exciton linewidth (γ_{inh}). In the present discussion we consider with γ_x the total non-radiative exciton linewidth, homogeneous or inhomogeneous. Whether exciton and photon are in the strong-coupling or weak coupling regime is mainly determined by their linewidths.

Including the exciton (γ_x) and cavity (γ_c) linewidth, which correspond to consider the complex polariton dispersion, the Rabi splitting is modified as:

$$Rabi\ Splitting = 2\sqrt{\hbar^2\Omega_{\mathrm{R}}^2 - \frac{\hbar^2}{4}(\gamma_c - \gamma_x)^2}. \qquad 2.20$$

If $2\hbar\Omega_R < (\gamma_c - \gamma_x)$, the term in the square root would be purely imaginary, resulting in two modes with the same energy: this is the weak-coupling regime, where the decay rate can be calculated in the framework of the Fermi golden rule without great changes with respect to the polariton picture. In the opposite case, when $2\hbar\Omega_R > (\gamma_c - \gamma_x)$, the Rabi splitting is real, and a gap opens between the UPB and LPB energies. This is the situation of the strong coupling regime, where polaritonic effects cannot be ignored. In the strong coupling regime the exchange rate between the photon and exciton is much faster than their decoherence rate, and thus the system is

properly described in terms of new quasi-particles, the polaritons, which are quantum exciton-photon mixture that represents the fundamental excitation of the system.

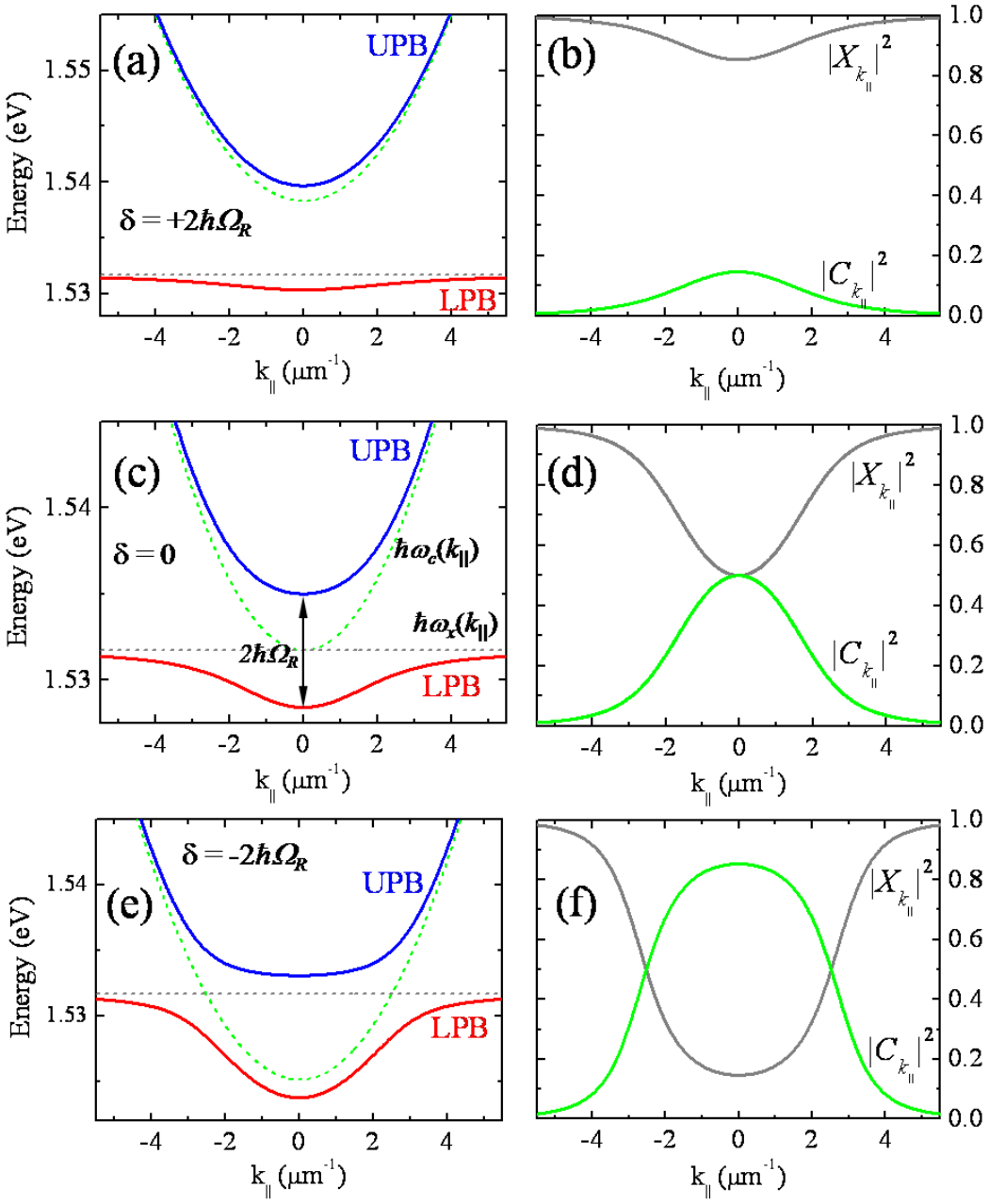

Fig. 2.2: Left panels: calculated bare exciton and cavity mode dispersions (dashed lines) as well as the polariton dispersions (solid lines) for different exciton cavity detunings δ in a microcavity with Rabi splitting of 6.6 meV. Right panels: corresponding Hopfield coefficient. Detunings: (a)-(b) $\delta = 2\hbar\Omega_R$, (c)-(d) δ=0, (e)-(f) $\delta = -2\hbar\Omega_R$.

The linewidths of the polariton resonances, γ_{UPB} and γ_{LPB}, are given by a linear combination of γ_x and γ_c, mediated by the Hopfield coefficients:(12)

$$\gamma_{UPB}(k_{\parallel}) = \left|X_{k_{\parallel}}\right|^2 \gamma_x + \left|C_{k_{\parallel}}\right|^2 \gamma_c$$
$$\gamma_{LPB}(k_{\parallel}) = \left|C_{k_{\parallel}}\right|^2 \gamma_x + \left|X_{k_{\parallel}}\right|^2 \gamma_c. \qquad 2.21$$

The dependence of the linewidths and of the polariton energies on the reflectivity of the mirrors is reported in Fig. 2.3, as calculated in ref (12), where the transition from the weak to the strong coupling as the reflectivity increases is clearly evidenced.

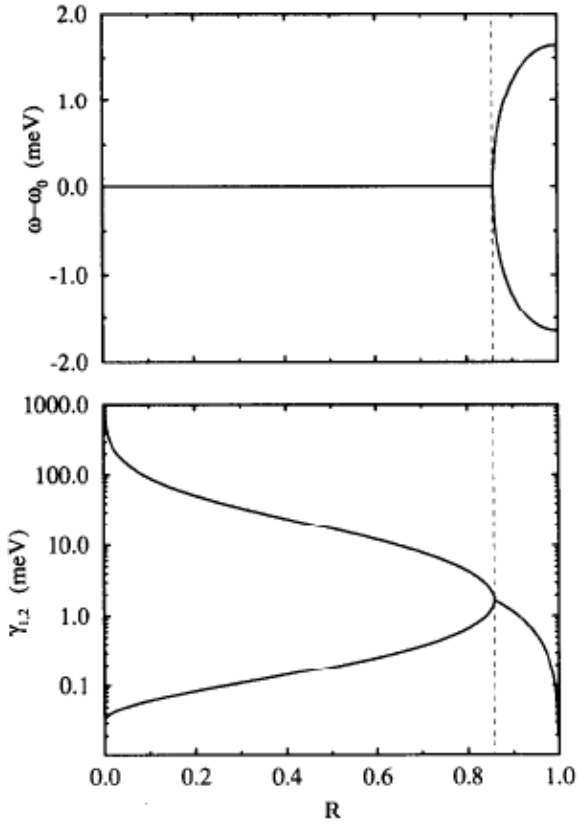

Fig. 2.3: Crossover between weak and strong coupling regime in the case of δ=0, calculated in ref [12] as a function of the DBR reflectivity R. The dashed line indicates the boundary between the two regimes. In the upper panel, ω is the frequency of the resonance of the system, i.e. degenerate exciton and cavity modes (ω_0) in the weak coupling regime and UPB and LPB in the strong coupling regime. In the lower panel, $\gamma_{1,2}$ are the exciton and cavity linewidths, which collapse in a single value in the strong coupling regime due to the symmetry of the Hopfield coefficient $\left(\delta = 0 \Longrightarrow \left|X_{k_{\parallel}}\right|^2 = \left|C_{k_{\parallel}}\right|^2 = 0.5\right)$.

2.3 – Polarization properties

The polarization properties of polaritons are determined by those of their components. In a microcavity, the symmetry is broken in the direction perpendicular to the QW plane, and it is convenient to use this axis as the main axis of the system, called z direction, to define the polariton polarizations. The third component J_z of total

angular momentum, $\hat{J} = \hat{L} + \hat{S}$, is a good quantum number along the z axis and will be called spin in the following.

In Fig. 2.4 are presented all the possible spin states of an exciton formed binding an electron with a heavy or light hole. Only transitions within the same subband index are considered. Actually, because of the parity of the wavefunction and their overlapping, these transitions are the strongest ones.

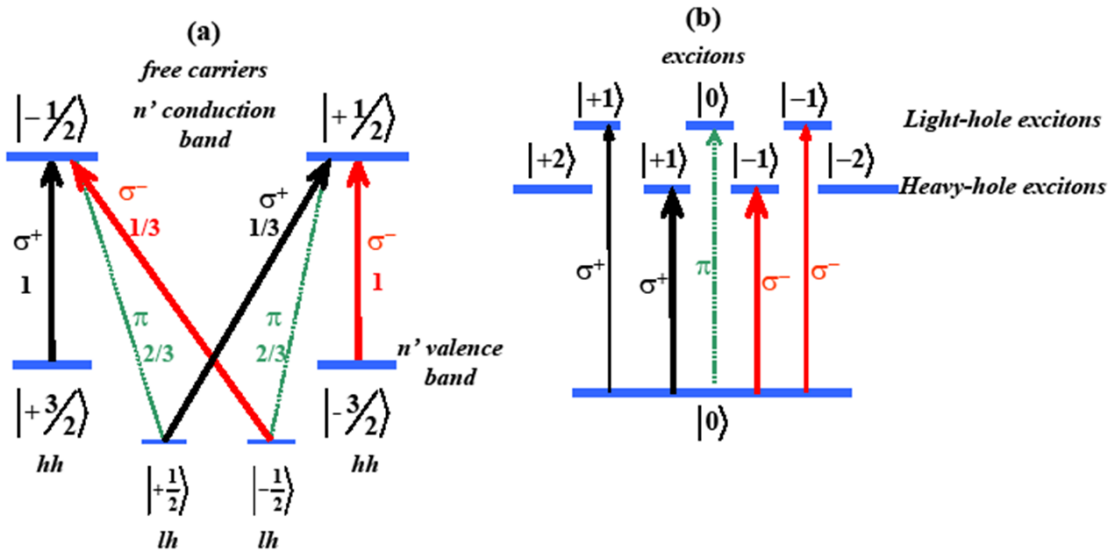

Fig. 2.4: (a) Polarization and relative intensity of the matrix element associated to the electric dipole allowed transitions from the heavy- and light-hole subbands to the conduction subband with the same index n'. (b) Same as (a) for the resonant creation and recombination of heavy- and light-hole excitons.

Exciton with spin $J_z = 0,1,2$ can be formed, however only exciton with $J_z = 1$ can couple to light (light-hole exciton with $J_z = 0$ can couple to linear polarized light with propagation direction in the plane of the QW, and will not be considered here). Heavy hole exciton with spin ± 2 are optically inactive and for this reason they are called dark states. Note also that, despite an optically active exciton is formed by two fermions, an electron and a hole, its total angular momentum is one. For this reason, exciton can be described as bosons (composite bosons), as long as their density is small enough to allow disregarding the fermionic nature of their components.

The angular momentum conservation imposes that only excitons and photons with the same spin can couple. In the case of a circularly polarized σ^+ (σ^-) beam, the third component of the angular momentum of the incident photons is +1 (-1). In this case, polaritons will be excited with spin +1 (-1). Thus, when the photonic part of the polariton leaks out of the cavity, destroying the polariton, it emits a circularly polarized photon. This is the situation at $k_{||} = 0$, in which the system is symmetric about the growth axis. When $k_{||} \neq 0$, the polarization properties of polaritons are more

complicated, because the cavity mode presents a small energy anisotropy between the modes linearly polarized along and perpendicularly to the direction of propagation inside the cavity. Linear superposition of these states gives rise to elliptical or linear polarization, and polariton emission can in principle show any polarization.

Bibliography:

[1] J. Rarity, and C. Weisbuch (editors). *Microcavity and photonic bandgaps: physics and applications*. NATO ASI Series. Kluwer Academic Publisher (1996).

[2] V. Savona, C. Piermarocchi, A. Quattropani, P. Schwendimann, and F. Tassone. *Optical properties of microcavity polaritons*. Phase Transitions **68,** 169 (1999).

[3] V. Savona, Z. Hradil, A. Quattropani, and P. Schwendimann. *Quantum theory of quantum-well polaritons in semiconductor microcavities*. Phys. Rev. B **49,** 8774 (1994).

[4] S. Jorda. *Theory of Rabi splitting in cavity-embedded quantum wells*. Phys. Rev. B **50,** 18690 (1994).

[5] S. Jorda. *Dispersion of exciton polaritons in cavity-embedded quantum wells*. Phys. Rev. B **51,** 10185 (1995).

[6] J. J. Baumberg, and L. Viña (editors). *Special Issue on microcavities*. volume **18** (10) of Semiconductor Science and Technology. (2003).

[7] V. Savona, F. Tassone, C. Piermarocchi, A. Quattropani, and P. Schwendimann. *Theory of polariton photoluminescence in arbitrary semiconductor microcavity structures*. Phys. Rev. B **53,** 13051 (1996).

[8] A. V. Kavokin, and G. Malpuech. *Cavity Polaritons*. Film and Nanostructures. Academic Press (2003).

[9] V. Savona, C. Permarocchi, A. Quattropani, P. Schwendimann, and F. Tassone. *Optical properties of microcavity polaritons*. Phase Transitions **68,** 169 (1999).

[10] M. Born, and E. Wolf. *Principles of optics electromagnetic theory of propagation, interference and diffraction of light*. Pergamon Oxford 6th edition (1980).

[11] J. J. Hopfield. *Theory of the contribution of exciton to the complex dielectric constant of crystal*. Phys. Rev. **112,** 1555 (1958).

[12] V. Savona, L. C. Andreani, P. Schwendimann, and A. Quattropani. *Quantum well exciton in semiconductor microcavities: unified treatment of weak and strong coupling regimes*. Solid State Commun. **93,** 733 (1995).

[13] R. Houdré, C. Weisbuch, R. P. Stanley, U. Oesterle, P. Pellandini, and M. Ilegems. *Measurament of cavity-polariton dispersion curve from angle-resolved photoluminescence experiments*. Phys. Rev. Lett. **73,** 2043 (1994).

[14] C. Weisbuch, M. Nishioka, A. Ishikawa, and Y. Asakawa. *Observation of the coupled exciton-photon mode splitting in a semiconductor quantum microcavity*. Phys. Rev. Lett. **69,** 3314 (1992).

[15] M. G. Raizen, R. J. Thompson, R. J. Brecha, H. J. Kimble, and H. J. Carmichael. *Normal-mode splitting and linewidth averaging for two states atoms in an optical cavity*. Phys. Rev. Lett. **63,** 240 (1989).

[16] Y. Zhu, D. J. Gauthier, S. E. Morin, Q. Wu, H. J. Carmichael, and T. W. Mossberg. *Vacuum Rabi splitting as a gfeature of linear dispersion theory: analysis and ezxperimental observation*. Phys. Rev. Lett. **64,** 2499 (1990).

Chapter 3

Samples and experimental setup

3.1 - Samples

3.1.1 – CdTe-based microcavities

The sample studied in the experiments described in Chapter 4 was grown by molecular beam epitaxy at the University "Joseph Fourier" Grenoble 1 (France) by the group of Dr. Regis André. The sample is a $Cd_{0.4}Mg_{0.6}Te$ λ-microcavity with top (bottom) distributed Bragg reflectors consisting of 17.5 (23) pairs of alternating $\lambda/4$-thick layers of $Cd_{0.4}Mg_{0.6}Te$ (thickness of 763 Å, refractive index $n = 2.81$) and $Cd_{0.75}Mn_{0.25}Te$ (thickness of 678 Å, $n = 2.5$). In each of the antinodes of the electromagnetic field there are two $CdTe$ QWs of 90 Å thickness ($n = 3.40$), separated by a barrier of 90 Å of $Cd_{0.4}Mg_{0.6}Te$. The Rabi splitting is of 10 meV. A sketch of the sample, on a 0refractive index scale, is reported in Fig. 3.1, where the substrate ($Cd_{0.88}Zn_{0.12}Te$) and the buffer layer ($Cd_{0.75}Mn_{0.25}Te$) are depicted as well.

The exciton-photon resonance, at 5 K, is at 1.625 meV (7630 Å), which yields an effective cavity length (see chapter 1.1.1) of $\sim$ 1520 Å, thus giving a penetration depth of the electromagnetic field inside the mirrors of ~ 73 Å.

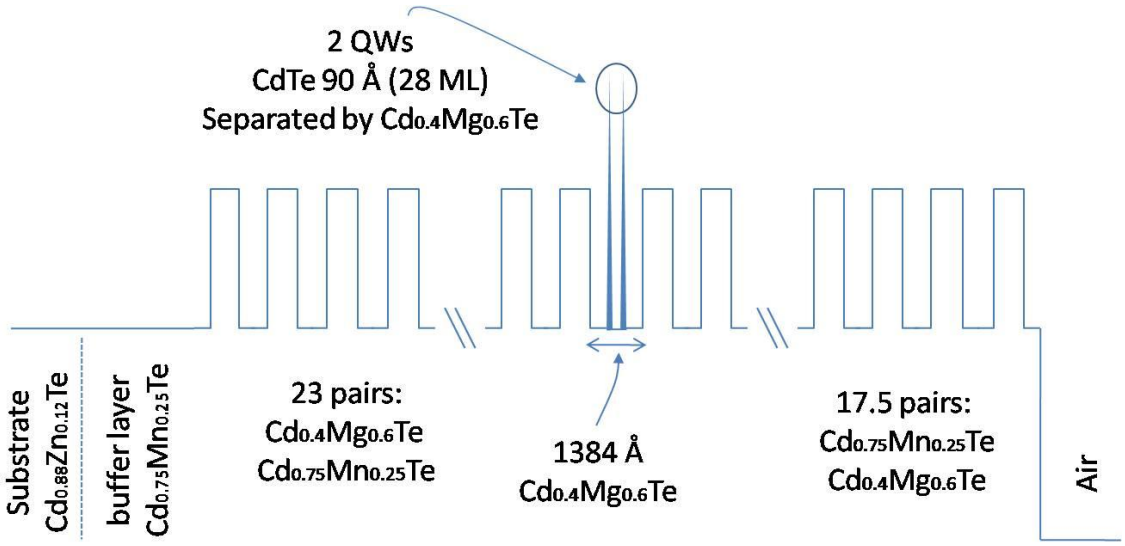

Fig. 3.1: Sketch of the sample on a refractive index scale. Each monolayer (ML) corresponds to 3.22 Å.

3.1.2 – GaAs-based microcavities

The microcavity employed in the non-resonant excitation experiments described in Chapter 5 was grown at the University of Sheffield (U.K.) by the group of Prof. Maurice S. Skolnick and Dr. John S. Roberts.

The sample was grown by metal organic vapor-phase epitaxy. The top (bottom) Bragg reflector is composed by 17 (20) pair of alternate $Al_{0,1}Ga_{0,9}As/AlAs$ layers. The $Al_{0,1}Ga_{0,9}As$ layers are 616 Å thick and the $AlAs$ layers 699 Å. The $GaAs$ cavity spacer has a ${}^{3\lambda}/_{2}$ configuration, with a nominal width of ~ 1500 Å. The cavity spacer presents a wedge across the sample that enables the tuning of the cavity-mode energy by changing the position of the excitation spot on the sample. Two groups of three $In_{0,06}Ga_{0,94}As$ QWs, each of them 10 nm wide, are embedded in the $GaAs$ cavity at the antinodes of the electromagnetic field. Within each group, the QWs are separated by 100 Å thick $GaAs$ barriers. The exciton-photon resonance is at 1.453 meV (8533 Å).

The cavity and excitonic linewidths, measured at very negative and positive detunings respectively, are, both, of about 1 meV. The cavity lifetime is of the order of $4\ ps$. The Rabi splitting, measured by PL experiments under non resonant excitation, at low power and low temperature (5 K), is 6.6 meV (see Fig. 3.2).

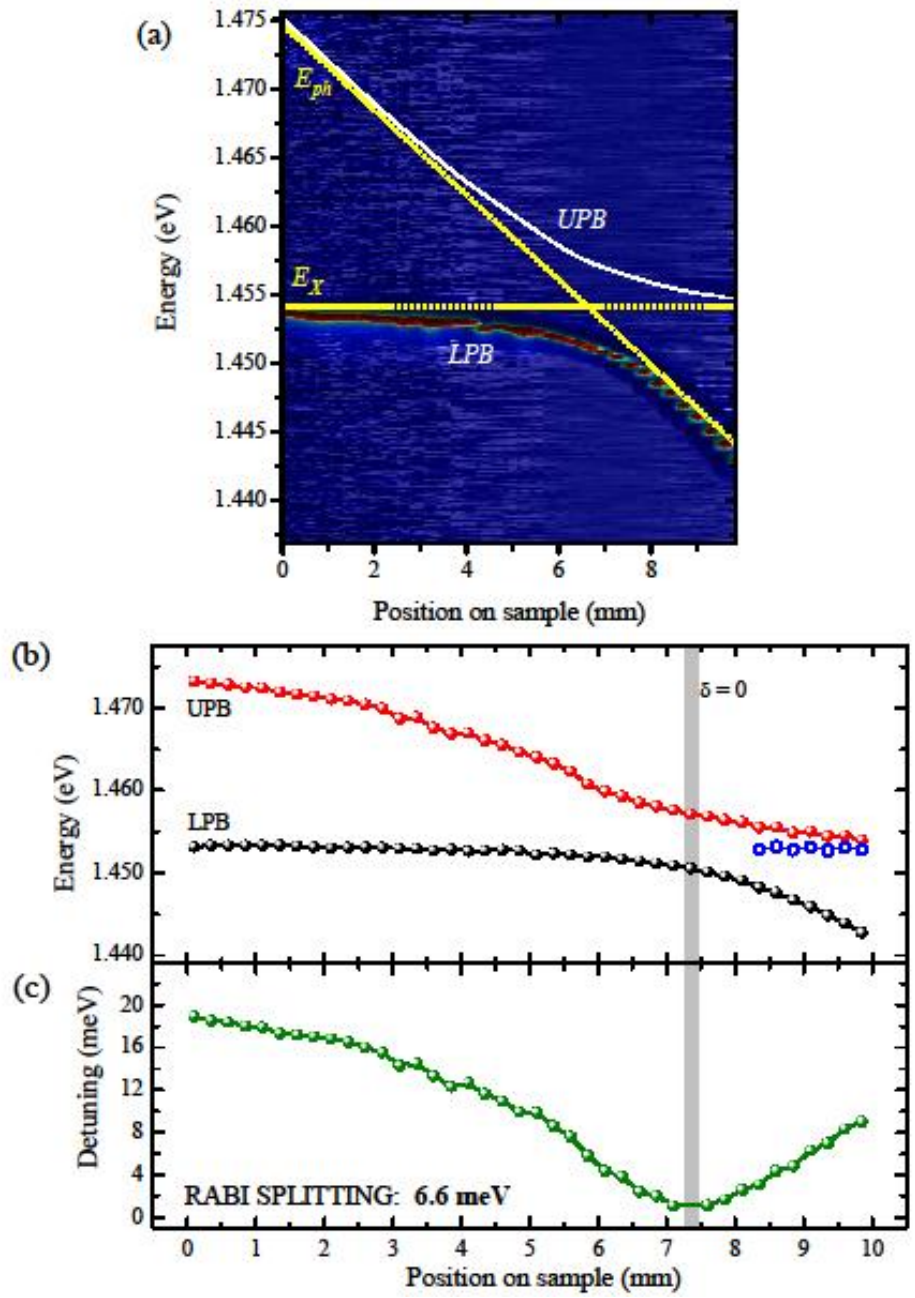

Fig. 3.2: (a) Colour map of the $k = 0$ emission from the $InGaAs/AlAs$ microcavity under non resonant CW excitationat 5 K. The horizontal axis indicates the position in millimeters along a straight line parallel to the cavity wedge of the sample. The dashed line depicts the energy of the bare exciton and cavity modes. (b) Energy of the UPB and LPB peaks extracted from (a); the open points depict the emission from uncoupled excitons, visible at slightly negative detunings. (c) Detunings δ as a function of the position on the sample calculated by $\delta = \sqrt{(E_{UPB} - E_{LPB})^2 - (\hbar\Omega_R)^2}$, where Ω_R is the Rabi splitting, extracted from (b): minimum energy difference between the UPB energy (E_{UPB}) and LPB energy (E_{LPB}), which occurs at $\delta = 0$.

The microcavity employed in the resonant excitation experiments described in Chapter 6 was grown at the Laboratoire de Photonique at de Nanostructures (CNRS, Paris, France) by the groups of Jacqueline Bloch and Aristide Lemaître. The sample was grown by molecular beam epitaxy. The top (bottom) Bragg reflector is composed by 15.5 (24) pairs of alternate $Al_{0,15}Ga_{0,85}As/AlAs$ layers, with thickness of 572 Å for the

$Al_{0,15}Ga_{0,85}As$ layer and of 675 Å for the $AlAs$ layer. The AlAs cavity spacer has a $\lambda/2$ configuration, with a nominal width of 1200 Å (M=2 in Eq. 1.2, that correspond to the second cavity mode) and analogously to the sample previously described, presents a wedge that allow for tuning the energy of the cavity mode by changing the position of the excitation across the sample, as shown in Fig. 3.3.

One 20 nm wide $GaAs$ QW is embedded in the spacer, at the center, where there is an antinode of the electromagnetic field. This is the QW whose exciton resonances couple to the cavity mode. One additional narrow QW, 2.6 nm wide, is present at each side of the wide QW, separated by an AlAs layer of 10 nm. The excitonic resonances of these QWs are much higher in energy than any of the polariton energies considered in the experiments described in Chapter 5, and will not affect the polariton physics presented in this work.

The use of a single, wide QW results in very narrow exciton linewidths, as the effects of the interfaces fluctuations and width distributions are greatly suppressed. In this case tha heavy-hole QW exciton presents a low temperature linewidth of about 0.3 meV, while the cavity-mode lifetime is still of the order of about 4 ps. The Rabi splitting, in the case of the heavy-hole exciton coupled to the cavity mode, is 4.4 meV. The exciton-photon resonance is at 1.530 meV (8104 Å).

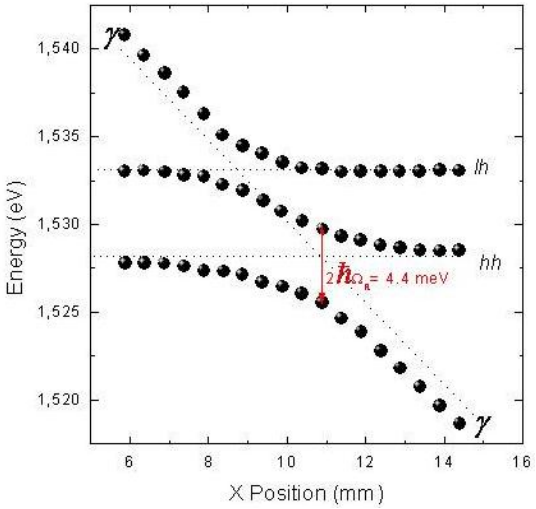

Fig. 3.3: Polariton energy versus the position of the excitation across the GaAs sample. The dashed lines correspond to the energy of the cavity mode (γ), light hole exciton (lh) and heavy hole exciton (hh). The Rabi splitting is also shown at the anticrossing position between hh and γ.

3.2 - Experimental set-up

In the experiments presented in this work two different excitation sources were employed:

- A continuous wave (CW) $Ti{:}Al_2O_3$ (Spectra Physics model 3900S) laser, pumped by a CW Ar^+ laser (Spectra Physics Beam Lok 2060). The wavelenght of the laser can be tuned between 720 nm and 860 nm
- A pulsed $Ti{:}Al_2O_3$ (Spectra Physics Tsunami) laser, pumped by a CW diode-laser (SP Millenia). The wavelenght of the pulses (2 ps long) can be tuned between 680 nm and 950 nm.

For the detection, were employed:

- a high resolution CCD (Princetone Instruments, model PIXIS: 1024F)
- a synchroscan Hamamatsu streak camera, composed by

  - main unit (C5680): input optics, streak tube, video output (inter-line CCD C4742-95, with effective number of pixel 756 (H) x 485 (V).)

  - synchroscan sweep unit (M5675), whose frequency is selected to match that of the tsunami laser (82.1 MHz)

In Fig. 3.4, the principles of operation of the streak camera are depicted.

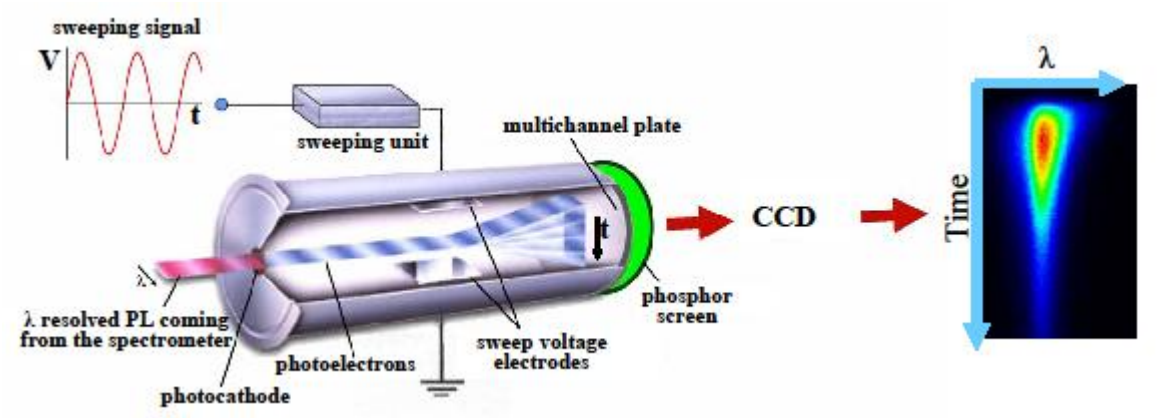

Fig. 3.4: Principle of operation os a synchroscan streak camera. See details in the text.

The light impinges upon a photocatode and excites photoelectrons inside the streak tube. The photoelectrons are accelerated by an accelerator mesh (not shown). Then they travel inside the tube through a region, between the electrodes, in which

there is an electric field whose strength varies in time. Early photons excite photoelectrons which are deviated upwards by the electric field. Photoelectrons created by later arriving photons encounter a field deflecting them in different vertical directions (downwards). In this way, the vertical direction behind the electrodes acquires the meaning of time evolution.

After the electrodes, a multichannel plate multiplies the number of electrons impinging upon it. Finally, the amplified photoelectrons hit a phosphor screen whose light is recorded by a CCD. In the CCD, the vertical direction corresponds to the time evolution while the horizontal direction reflects the horizontal dimension of the light arriving at the photocathode, which can be wavelength, when the gratings of the spectrometer is used as a dispersive element, or spatial dimension, when the grating is set for zero order detection and behaves as a mirror, allowing for real- or momentum-space images to be obtained (see next section).

The sweeping-voltage that deviates the photoelectrons has a sinusoidal shape, but only the linear part of the sinusoidal is employed. The sweeping-voltage frequency is synchronized with excitation pulses via a fast photodiode and presents, therefore, the same repetition rate as the pulses. In this way, millions of identical measurements (one per excitation pulse) can be performed and a signal can be obtained even in very low-emission intensity conditions.

There are four time ranges for the displayed sweep time, increasing the time window from time range 1 to time range 4. The largest time-window (time range 4) of the streak camera has a size of $2100\ \mathrm{ps}$ with a resolution of about $30\ \mathrm{ps}$. However, the resolution can be improved below $10\ \mathrm{ps}$ by operating the camera in the shortest time window (time range 1, $160\ \mathrm{ps}$). Time range 2 and 3 cover $800\ \mathrm{ps}$ and $1500\ \mathrm{ps}$, respectively. When the streak camera is coupled to the spectrometer, in the real space configuration (explained in detail later), the final energy resolution is of $0.25\ \mathrm{meV}$.

Alternatively, the emission can be visualized by the high resolution CCD camera PIXIS: 1024F (Princeton Instrument, see Fig. 3.5), optimized for detection in the near infrared region, NIR $(750\ \mathrm{nm} < NIR < 1150\ nm)$. The screen is composed by a 1024×1024 imaging array, with pixel dimensions of $13\ \mu\mathrm{m} \times 13\mu\mathrm{m}$.

Fig. 3.5: Picture of the Princetone Instruments PIXIS 1024F CCD.

Both the CCD and the streak camera are coupled to a spectrometer: the output signal of the spectrometer can be switch towards the CCD or the streak camera thanks to a mobile mirror whose position is controlled by software. The spectrometer actually employed in our experiments is a Princetone Instruments Acton Spectra Pro 2500i triple monochromator/spectrograph, with mechanical scan range of $0 - 1400$ nm. The grating (1200 groove/mm), whose size is of 68×68 mm, provide a linear dispersion of 1.52 nm/mm (at 435.833 nm), with an optical dispersing path of 1 m and wavelength accuracy of $\pm$ 0.2 nm (repeatability of $\pm$ 0.05 nm). The maximum final resolution on the PIXIS CCD is of 0.06 nm.

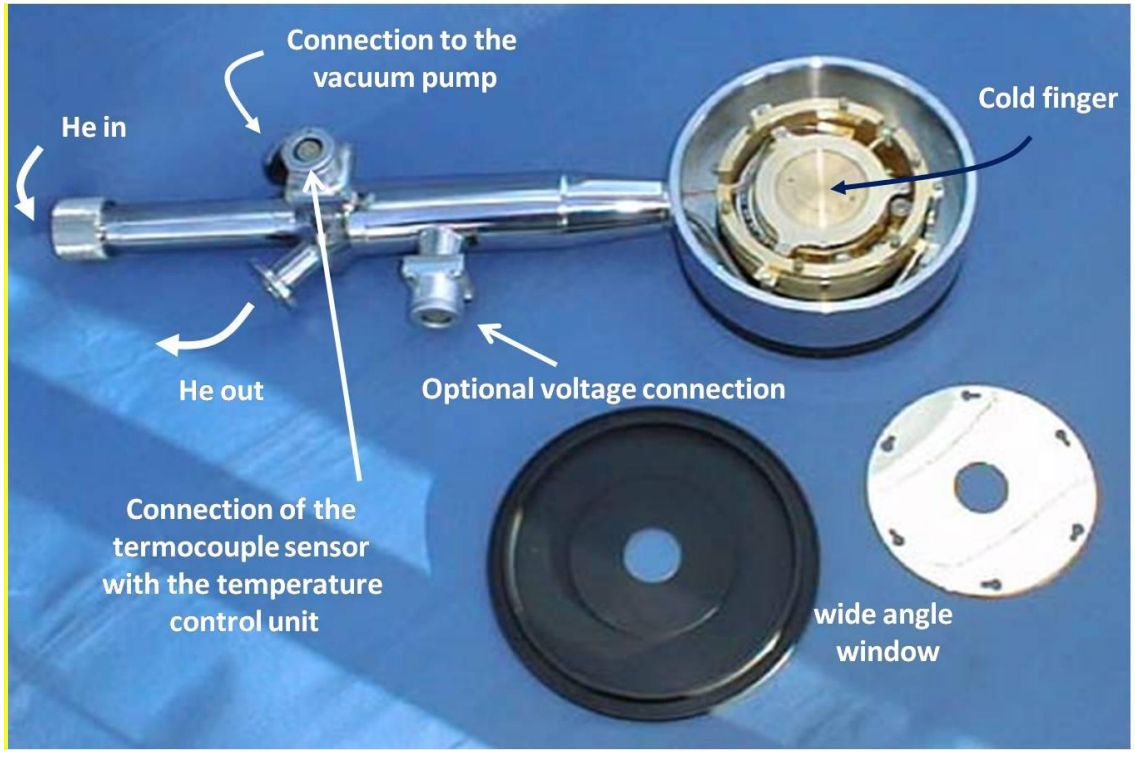

Fig. 3.6: Picture of the disassembled CryoVac wide-angle cryostat

All measurements have been performed at low temperature (5-10 K): the samples were pasted by silver paint in a cold finger cryostat cooled by a continuous flow of He and the temperature was controlled by a thermocouple sensor inserted in the cryostat. Two different cryostat have been employed: a cold-finger cryostat (Oxford Instruments), with temperature range from 4 K to 350 K, and a cold-finger, wide-angle cryostat (CryoVac, 4 K-350 K), in which the sample is accessible in an angular range of 0°-30° with respect to the direction normal to the sample surface. In Fig. 3.6, the disassembled wide-angle cryostat is shown.

3.3 - Time-resolved PL set-up

The time-resolved experimental set-up employed for the experiments of Chapter 4 and 5 is depicted in Fig. 3.7.

In general, the pulsed excitation beam is tuned at the first minimum of the stop band of the microcavity (non-resonant experiment), in order to minimize the reflection and allow the non-resonant creation of electron-hole pairs, which then relax and couple with the cavity mode forming the exciton-polaritons. The pulsed beam impinges on the sample with a small angle from the direction normal to the surface (growth direction). The CW beam is used for the sample characterization. The sample is kept in a cold finger cryostat where the temperature can be varied between $5\ \mathrm{K}$ and room temperature. The temperature sensor is placed very close to the sample holder, where the sample is attached with silver paint to ensure a good thermal contact.

The light is collected using the focusing lens (F), in reflection geometry, and focused, with a second lens (A), on the entrance slit of the spectrometer. It is important to stress that lens A is positioned at the same distance, equal to its focal length, f_A, both from the spectrometer and from the Fourier plane of lens F. The spectrometer, which obtains the energy resolution in these experiments, is coupled to the streak camera.

For the experiments of Chapter 4, where the PL is analyzed into its two linearly polarized components, polarization optics are added to the excitation and detection paths. The direction of the linear polarization of the excitation beam is controlled by a linear polarizer and a $\lambda/2$-plate, while in the detection path a linear polarizer select the PL component with the desired direction of linear polarization. The PL intensity analyzed in its orthogonal linear polarizations, recorded in subsequent repetitions of the experiments, is compared to obtain the linear polarization degree. A λ/4-plate is placed after the linear polarizer, at the entrance slit of the spectrometer, to overcome the polarization sensitivity of the grating.

For the experiments described in Chapter 5, the circular polarization degree is obtained adding a set of quarter waveplate and linear polarizer in both the excitation and detection paths.

In order to select the PL coming from different k-states of the microcavity, a pinhole has been included in the detection arm at the Fourier plane. The pinhole is mounted on a translational stage, and blocks all light except that coming with a particular direction. In the momentum space, a given k-state corresponds to one direction, and it can be select just by moving the pinhole perpendicularly to the optical axis. The in-plane momentum of a polariton state and the angle of emission of that state are related by

$$k_{\parallel} = k_z \tan\left[\sin^{-1}\left(\frac{1}{n_{cav}}\sin\vartheta\right)\right],$$

Where $k_{\parallel}$ is the in plane momentum, $k_z = \frac{2\pi}{\lambda}$ is the confined momentum in the growth direction (with λ being the cavity mode wavelenght at $k = 0$), n_{cav} is the refraction index of the cavity and ϑ is the emission angle.

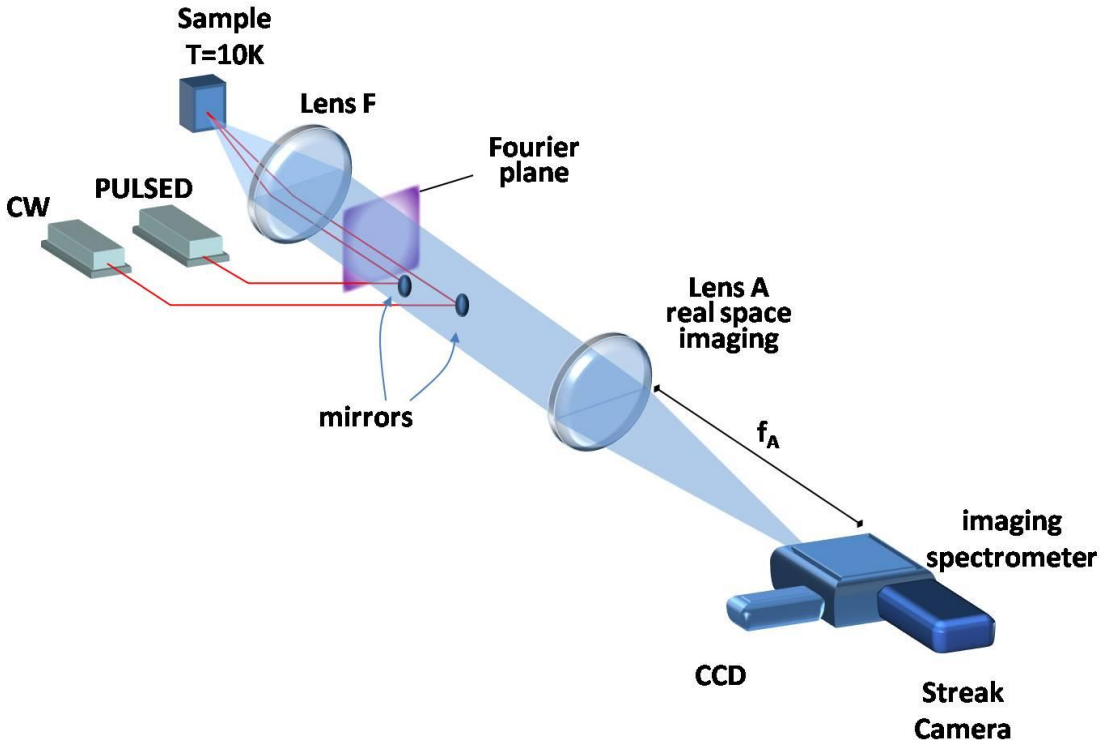

Fig. 3.7: General experimental setup for time-resolved PL under non resonant excitation.

In the experiments described in Chapter 6, the sample is resonantly excited with CW and pulsed beams. As shown in Fig. 3.8, each excitation beam is directed towards the sample by an independent mirror. By positioning them at different distances from the optical axis (Δx) of the focusing lens F, the angle of incidence θ_{inc} of each beam can be selected ($\theta_{inc} = \arctan\left(\frac{\Delta x}{f_F}\right)$, where f_F is the focal length of the focusing lens F).

For momentum-space detection, a third lens (B) is added to the set-up and lens A forms an image of the Fourier plane on the entrance slit of the spectrometer, as shown in Fig. 3.8. The Fourier plane of the lens F is perpendicular to the optical axis and located at the focal plane of this lens, symmetric to the sample (see Fig. 3.8). All rays coming out from the sample at a given angle (which corresponds to a well defined in-plane momentum, as $k_{\parallel} = \frac{E}{\hbar c}\sin\left[\arctan\left(\frac{\Delta x}{f_F}\right)\right]$) form a point in the Fourier plane.

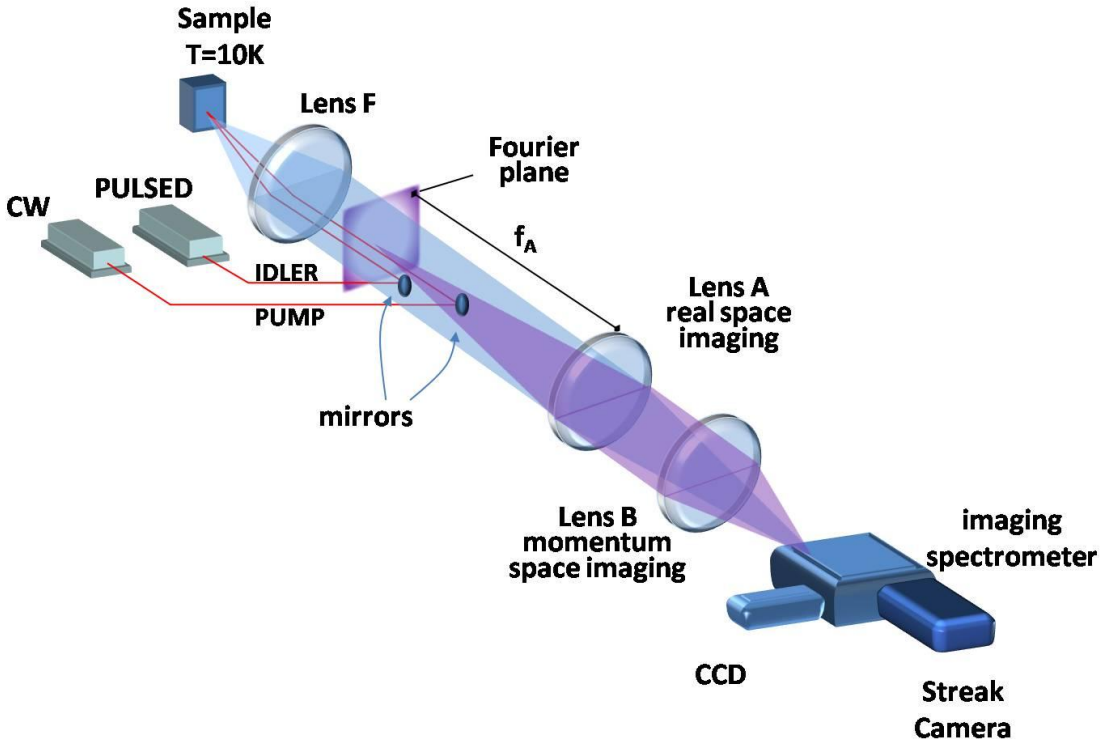

Fig. 3.8: Setup for the experiment described in Chapter 5, with resonant excitation of both the CW and pulsed beams. With this configuration, energy-resolved and momentum-resolved images can be obtained.

The Fourier plane is therefore a map of the angular emission from the sample. Along the entrance slit of the spectrometer, a slice of the momentum space image of the emission is selected and imaged either on the CCD or on the input slit of the streak camera (with the spectrometer set at zero order, working as a mirror).

Additionally, the spectrometer allows dispersing in energy the light arriving at the entrance slit. In this way, the energy distribution (energy versus in-plane momentum) of the polariton emission can be directly recorded by the CCD camera, as shown in Fig. 3.9.

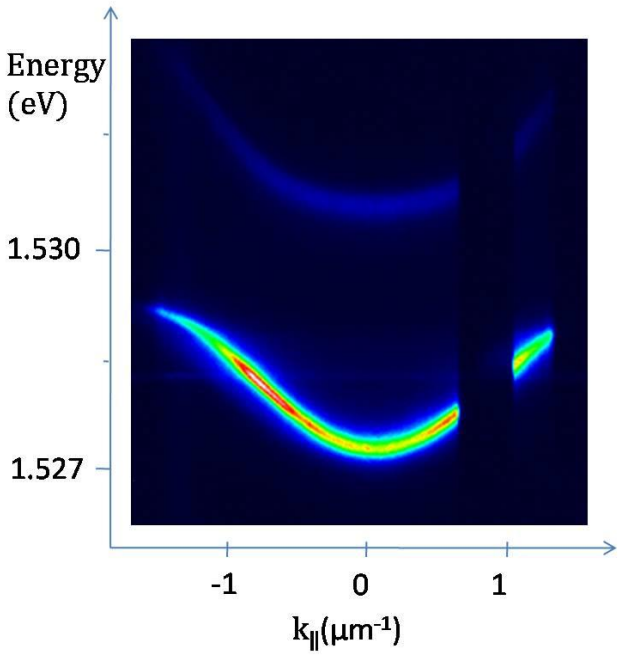

Fig. 3.9: CCD image of the polariton dispersion of a GaAs-based microcavity obtained from the light emission in the momentum space configuration. It reflects a slice of the polariton energy distributions along a direction of the Fourier plane. The dark region in the image is the shadow of the mirror used to excite the sample.

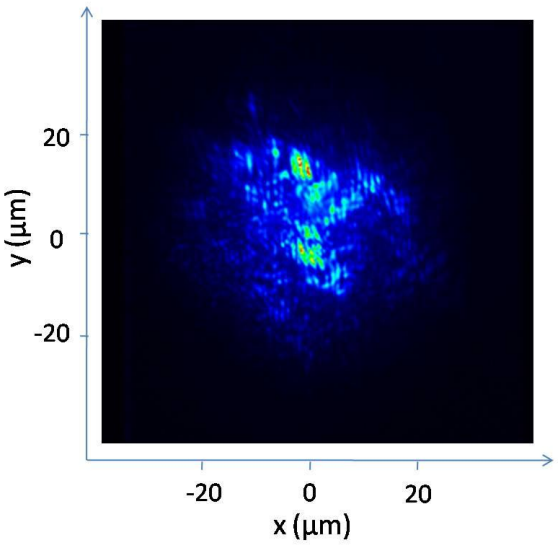

Fig. 3.10: Real space imaged on the CCD with the spectrometer set at zero order. The reflection of the laser beam on the sample surface has been blocked and the spatial distribution (inside the spot) of the energy-integrated polariton emission of a GaAs-based microcavity is obtained.

Analogously, both momentum-space and real-space images can be obtained in 2D, without any energy resolution, just opening the entrance slit of the spectrometer. As an example, a CCD image in real-space configuration of the PL emission from a GaAs-based microcavity is shown in Fig. 3.10.

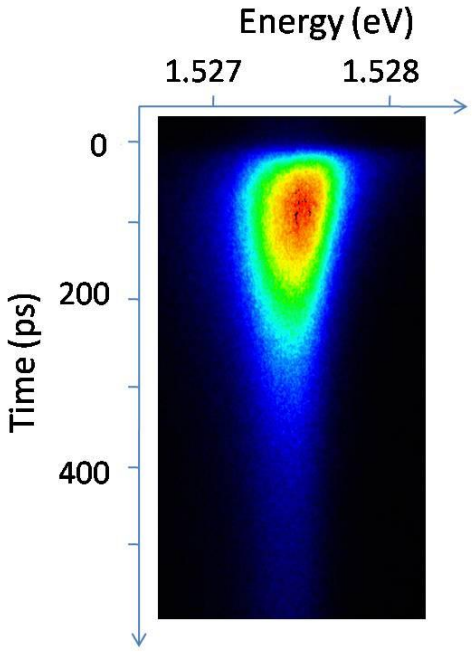

Fig. 3.11: Streak camera image of the PL of a GaAs-based microcavity, obtained in real space configuration, with energy represented in the horizontal direction and time evolution in the vertical one.

The streak camera allows for detecting the time evolution of the emission both in real space configuration, where the horizontal and vertical direction represent energy and time, respectively, and in momentum space configuration, where the horizontal and vertical direction represent momentum and time, respectively (in the latter case the spectrometer must be set at zero order). In Fig. 3.11, an energy- and time-resolved image of the PL of a GaAs-based microcavity after a pulsed excitation is shown.

Chapter 4

Pinning of the polarization of the light emission

4.1 – Spin relaxation in semiconductor microcavities

Among the principal mechanisms of spin relaxation of charge carriers in semiconductors, the most important are the Elliott-Yafet (EY)(1, 2), Bir-Aharonov-Pikus (BAP)(3), and D'yakonov-Perel (DP)(4) mechanisms connected with the intrinsic symmetry properties of crystals, spin-orbit and exchange interactions. The EY mechanism is only important for small gap semiconductors and will be disregarded here. In the case of excitons, the most efficient spin relaxation mechanism is BAP. In these mechanisms, an effective magnetic field, around which the carrier's or exciton's spin precesses, appears due to: (a) the splitting of different spin-polarized carrier states that comes from the spin-orbit interaction and the existence of non-quadratic terms in the bands (DP); (b) the splitting between excitons having orthogonal dipole-momentum orientations (BAP).(5) The orientation of this effective field is dependent on the wave vector direction. The scattering of particles changes their wave vector direction and therefore also the rotation axis. This interplay between scattering and spin precession results in a fast loss of the collective spin orientation.

For the case of exciton-polaritons, they exhibit, in the optical active region of the reciprocal space, a longitudinal-transverse splitting (TE-TM energy splitting, between exciton-polariton states having their dipole moments perpendicular and parallel to the in-plane wave-vector).(6) The TE-TM splitting acts as an effective magnetic field in the plane of the QW and gives rise to rotation of the polariton polarization. This splitting could be very large, and should provoke a very fast spin

relaxation, but, surprisingly, a complete different behavior has been experimentally observed: long living spin polarizations in the emission of microcavities have been reported both under resonant and non resonant excitation. In particular, stimulated scattering of polaritons is able to conserve a collective spin orientation.(7, 8)

In microcavities, the spin dynamics of the polaritons can be accessed through the study of the polarization of the light leaking out of these systems: bright polaritons have the same spin states as those of the emitted light, with the spin component along the growth direction of the microcavity which can attain the values +1 or -1.(9, 10) Linear combinations of these sates give rise to elliptical or linear polarization, and, in principle, the polariton emission can show any polarization.

A circularly polarized (σ^+) excitation light will create a population of +1 spin polaritons. After that, a −1 spin population will appear as a result of the spin-flip mechanisms, which eventually equalize both spin populations. The recombination of this −1 spin population will result in a σ^--polarized emission. Since there is no mechanism that changes the spin of its photonic part, the spin relaxation of polaritons occurs through the spin relaxation of their excitonic component.

In recent years, the spin of microcavity polaritons has elicited a lot of interest, and many efforts have been devoted to investigate the role of polariton-polariton interactions on the spin dynamics, both with resonant and non-resonant excitation. Clearly, spin properties of microcavities in the strong coupling regime, when bosons (exciton polaritons) govern the polarization of the emission, are drastically different from the spin dynamics in the weak coupling regime, dominated by spin relaxation of fermions (electrons and holes).(11, 12)

In the strong coupling regime, under resonant excitation of the LPB, the spin dynamics show a very complex behavior: the polarization properties of the emission are determined by the scattering processes involved in the polariton relaxation. In the optical parametric oscillator configuration, in which the excitation is close to the inflection point of the LPB, resonant scattering of pump polaritons into signal and idler states can be stimulated by final state occupation.(13-15) The difficulty in the stimulated regime is that spin and energy relaxation cannot be decoupled. In the experiments of Ref (13), which was the first observation of stimulated polariton scattering in semiconductor microcavities, a circularly polarized pump excited the cavity at the so-called “magic angle”, and generated a coherent polariton population at the inflection point of the LPB. Then a circularly polarized probe pulse generated polaritons in the ground state, which stimulated polariton-polariton scattering from the pump state to the signal and idler states. In the first instance, it seemed that the scattering of polaritons from the pumped states towards the ground state could only happen if the pump and probe were co-circularly polarized. In the case of cross-circularly polarized light, no stimulation should happen, at least if the spin-flip

processes are not ultrafast, as confirmed separately.(16) It seemed possible to describe all the intermediate situations where both pump and probe were elliptically polarized by simply decomposing the pulse pump into left and right circular polarization components, one of which is strongly scattered and the other which is not scattered at all.

However, in pump-probe experiments in III-V microcavities,(8) in the case of a linearly polarized pump pulse, impinging at the angle of inflexion of the LPB, and circularly polarized probe pulse, at normal incidence, it has been found that the signal ($k = 0$) was linearly polarized but with a plane of polarization rotated by 45° with respect to the pump polarization. In the case of circularly polarized pump pulses, the polarization of the signal was also circular but its intensity was half that found for a linear pump. The polarization of the idler emission emerging at roughly twice the pump angle showed a similar behavior, although in the case of a linear polarized pump the idler polarization was rotated by 90° with respect to the pump polarization.

Kavokin et. al. (17) proposed an explanation of the observed polarization plane rotations of the emission which is based on a pseudospin model and reflects the energy splitting between spin-polarized excitonic populations. As any two-level system, the optically active exciton doublet can be characterized by a pseudospin whose projections on the coordinate axes can be expressed via the elements of excitonic density matrix. It describes both the exciton-spin state and its dipole moment orientation: the normal-to-plane pseudospin component characterizes the excitonic spin polarization, while its in-plane components describe the exciton dipole moment orientation. In particular, the authors of Ref. (17) considered the modification to propagation through the QW caused by optical pumping and the diffraction of the pump pulse on the optical grating induced by the pump and probe pulses at the QW (four wave mixing process). The in-plane components of the signal electromagnetic field would be determined, in this model, by the sum of three different terms: the isotropic optical response of the system, the in-plane anisotropy induced by a linearly polarized component of the pump pulse (which reflects the energy splitting of the exciton resonance in two states with different orthogonal linear polarization, along X and Y direction in the QW plane) and the gyrotropy induced by a circularly polarized component of the pump pulse (which reflects the energy splitting between two excitonic populations with opposite spin, +1 and -1).

Indeed, under resonant excitation, the pump pulse generates large coherent circularly polarized polariton populations (left and right circularly polarized, σ^- and σ^+, respectively). If the σ^+ population exceeds the σ^- one, it provokes a blueshift of the σ^+ exciton resonance and a redshift of the σ^- exciton resonance. This renormalization, which is due to the repulsive exchange interaction between two spin-polarized excitonic populations, is not specific for semiconductor microcavities and it has been

observed by Viña et. al.(18) and theoretically described by Fernandez-Rossier et. al.(19) and Savasta et. al.(20) This shift is responsible for a giant Faraday rotation of the polarization plane of light during its propagation within the cavity.(21)

In the pseudospin model, the splitting between circularly polarized polariton states induces an effective magnetic field in the growth direction (z axis). Under the influence of this field, the linear component of an elliptically polarized polariton state rotates about the z axis (self induced Larmor precession).

The optically induced splitting of the exciton resonance in X- and Y-linear polarizations has, according to Kavokin and co-workers, a huge influence on the signal polarization for linear pumping. It should present the same features as the optically induced splitting of circular polarization, namely, the exchange interaction between two exciton population with different pseudospin projection (in the case of circular polarization splitting, the exchange interaction involves excitonic populations with opposite spin, in the case of linear polarization splitting, the exchange interaction involves excitonic populations with different dipole momentum but with the same spin).(17)

In addition, the polariton polarization can be rotated by polariton-polariton scattering: the formation of a signal and an idler population is indeed due to exciton-exciton interactions, and, since the dipole-dipole interaction is strongly anisotropic, the polarization of the two resulting polaritons will be oriented along a preferential direction.

Once that the spin dynamics under resonant excitation has been adequately described by the pseudospin formalism,(22, 23) the same model has been applied for non resonant excitation conditions.(24, 25)

Under non-resonant excitation, polariton emission also show non trivial polarization dynamics,(7, 26) which has attracted a lot of interest. Indeed, in 1996, the concept of polariton laser, based on a microcavity, has been proposed (27). In such a laser, light would be emitted spontaneously by a Bose-Einstein condensate (BEC) of exciton-polaritons and it has been predicted that the spontaneously condensed polariton states at $k = 0$ must show linear polarization. Several experimental evidences of this behavior have been provided, (28, 29) however non negligible degrees of linear polarization have been observed at $k = 0$ also below the condensation threshold,(30) due to crystallographic anisotropies of the sample.

The spin dynamics under non-resonant excitation has a big interest because it mimics the situation that will be found under electrical injection and therefore it constitutes an intermediate step in the fabrication of potential spintronics devices. However, there is a major disadvantage for non-resonant excitation: a bottleneck in the relaxation of polaritons towards $k = 0$ states. For small polariton populations, the

non-resonantly created polaritons accumulate in the bottleneck region, hindering the energy relaxation. However, for large enough populations, strong polariton-polariton interactions trigger the stimulated relaxation to $k = 0$. This polariton final-state stimulated scattering has proven to be very efficient in overcoming the bottleneck, allowing the observation of very interesting non-linear effects, such as polariton stimulated emission,(31, 32) optical gain (33) and very recently the formation of a condensed phase.(34)

In the quest for polariton lasing, a very important issue is the polarization dynamics in microcavities under non resonant excitation, which is strongly dependent on how the polariton-polariton interactions occurring near the bottleneck region affect the spin properties. We have mentioned above that a spontaneous build-up of a linear polarization in the emission of polariton lasers has been predicted theoretically [6]. According to this theory, the direction of linear polarization would be spontaneously chosen by the system, and it would vary randomly from one experiment to another.

In the present chapter we show experimentally that the linear polarization of emission of polaritons is pinned to one of the crystallographic axes. This pinning comes from the optical anisotropy of microcavities which may be caused either by a small birefringence in the mirrors and cavity, by the exciton localization at QW interfaces or by the QW intrinsic anisotropies.

4.2 – Polarization degrees

In microcavities, spin relaxation of exciton-polaritons is correlated with their momentum relaxation. This makes microcavities a unique laboratory for studies of spin-polarized bosons. This correlation leads, in certain cases, to conservation and even build-up of a given polarization in a given quantum state.(7, 35) Photoluminescence experiments on the polarization dynamics in microcavities, excited resonantly or non-resonantly by a polarized laser light, have revealed a number of interesting effects, such as the self-induced Larmor precession,(8) quantum beats between dark excitons and polaritons,(36) and inversion of the polarization degree.(17, 37, 38)

In the case of linear polarization experiments, polaritons can be polarized along the transverse-electric (TE) and transverse-magnetic (TM) directions. In the TE mode, the light is polarized perpendicular to the direction of propagation of polaritons in the plane of the microcavity, while in the TM mode, light is linearly polarized parallel to the propagation direction.

As shown in Fig. 4.1, TE modes can be excited with light linearly polarized perpendicular to the plane of incidence (green arrow), while TM modes will be excited by light linearly polarized parallel to that plane (red arrow, orange component parallel to the propagation direction inside the cavity).

TE and TM configurations are well defined by the orientation of the linearly polarized light and by the angle of incidence of the exciting beam. Under TM excitation, the degree of linear polarization $\wp_{lin}$ of the emission is defined as:

$$\wp_{lin} = \frac{I^{TM} - I^{TE}}{I^{TM} + I^{TE}}, \qquad 4$$

where I^{TM} (I^{TE}) indicates the intensity of the emission linearly polarized parallel to the TM (TE) direction.

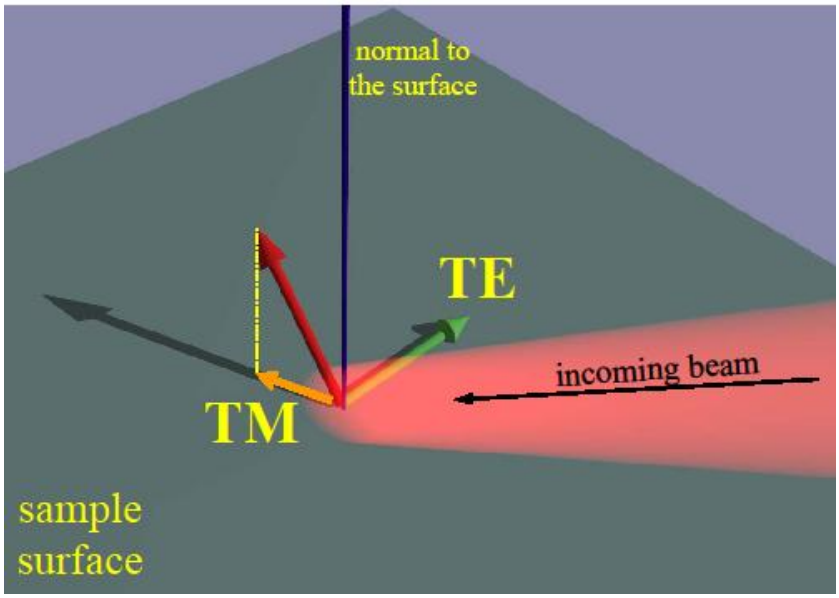

Fig. 4.1: Excitation of TE and TM polarization modes. The sample surface is parallel to the quantum well and cavity spacer, and the plane of incidence is that defined by the incoming beam and the normal to the surface. The green arrow indicates the direction of linear polarization perpendicular to the plane of incidence. In this case there is always a component of the electric field parallel to the propagation direction in the cavity (orange arrow).

The TE-TM splitting, due to the the long-range exchange interaction for exciton in QWs, is zero for polariton with $k = 0$, but it may be important for polaritons with higher momenta: it increases as a function of k, following a square root law at large k.(39) Moreover, due to in-plane asymmetries of the QWs or Bragg mirrors, a splitting may arise between the linearly polarized polaritons along the direction of the asymmetry, usually oriented along one crystallographic direction of the heterostructure.

Under circular excitation σ^+, the degree of circularly polarization can be analogously defined as:

$$\wp_{circ} = \frac{I^{\sigma^+} - I^{\sigma^-}}{I^{\sigma^+} + I^{\sigma^-}}, \qquad 4$$

where now I^{σ^+} (I^{σ^-}) indicates the intensity of the emission with spin +1 (-1).

4.3 – Polariton dynamics: three excitation regimes

The spin relaxation in semiconductor microcavities is strongly connected with the energy relaxation of polaritons. In the configuration we are interested in here, which is under non resonant excitation and negative detunings, polariton dynamics depends on the density of polaritons in the system, or, which is the same, on the excitation intensity.

The polariton dynamics in semiconductor microcavities at negative detunings has been studied varying the non-resonant excitation power by Ł. Kłopotowski et al.,(26) and, in the time-resolved emission spectra, three regimes have been observed.

The emission from the $k = 0$ states of the LPB, as the excitation power is initially increased, shows a quadratic intensity dependence. As the excitation power is further increased, a first threshold is reached. Above this value, the LPB emission presents a dramatic increase until a second threshold is reached. Above the second threshold, the emission intensity increase linearly with the excitation power and saturates.

In the quadratic regime, the decay of the LPB emission is slow: the decay time is of the order of 200 ps. Above the first threshold, a substantial acceleration is observed: the decay times become as short as 20 ps, and this fast emission dynamics is observed also above the second threshold, in the saturation regime.

After a non-resonant excitation pulse, photocreated electron–hole pairs loose most of their momentum via scattering with LO phonons. For negative detunings, the LPB has a large photonic character. Therefore, approaching $k = 0$, the curvature of the dispersion becomes very large and the density of states (proportional to the polariton mass) very small. Consequently, phonon scattering, as an energy relaxation mechanism, which would lead to a linear dependence of emission intensity on the excitation intensity, becomes inefficient, and a reservoir of polaritons is formed. The energy relaxation from the reservoir to $k = 0$ states occurs via spontaneous polariton–

polariton scattering, resulting in a quadratic dependence of the emission on the excitation power (spontaneous regime). This relaxation bottleneck effect disappears as the number of polaritons is further increased.

Above a certain density, polariton–polariton scattering becomes stimulated by the occupation of the final $k = 0$ state. This effect results in a significant acceleration of the relaxation processes (40) and, consequently, in an exponential increase of the emission intensity with increasing excitation density.(41) This range of excitation intensities corresponds to the stimulated regime. A further increase of the polariton population results in bleaching of the exciton transition due to exchange interaction and phase space filling (42); the bosonic description ceases to be valid, and a transition to weak coupling regime takes place. Indeed, above the second threshold, in the saturation regime, the transition energy becomes equal to the energy of the bare cavity mode.

4.4 – Polaritons spin dynamics under nonresonant excitation: exciton-cavity detuning dependence

For excitons in bare QWs under σ^+ pulsed excitation, the circular polarization degree reaches its maximum value just after the pulse excites the sample and then decays exponentially to zero. On the other hand, in microcavities, under non resonant pulsed excitation, the circular polarization degree $\wp_{circ}$ presents a maximum $\wp_{circ}^{max}$ at a finite time.

Just after the pulse, due to coherence losses in the relaxation mechanisms of polaritons, the emission from k = 0 state posses only a small polarization degree $\wp_{circ}$: $\wp_{circ}^{max}$ is reached, typically, after 60 – 100 ps, and its value increases with excitation density. The fact that a finite time is needed to reach $\wp_{circ}^{max}$ implies that there must be a new scattering mechanism that favours polaritons with +1 spin, and thus competes with spin relaxation and tends to prevent equalization of both spin populations. At very low powers, the relaxation of large in-plane wavevector excitons is governed by the emission of acoustic phonons and by spontaneous polariton-polariton scattering, which have no spin dependence. At higher powers, the new mechanism has been interpreted as stimulated polariton–polariton scattering, which is stimulated by the polariton final-state population and is strongly spin sensitive. The increase of $\wp_{circ}^{max}$ with excitation density effectively provides evidence that there is an enhancement of the scattering to the +1 spin state. The stimulation does not occur for the σ^--polarized

LPB emission, which also shows a time evolution with rise and decay times much longer than those observed in the stimulated regime for the σ^+ emission.

In this stimulated regime, once the maximum degree of polarization is reached, its dynamics is strongly dependent on the exciton-cavity detuning.(7) In Fig. 4.2, the polarization degree of a GaAs based microcavity ($\delta \approx 4.5$ meV), in the spontaneous and stimulated regimes, versus time is shown: a negative dip (−60%) is present at ∼150 ps, which is absent for larger detunings.(37) A similar phenomenon has been reported for QWs (43, 44) and is attributed to an anisotropic spin-splitting of localized excitons, induced by the long-range electron–hole exchange interaction, while in the case of planar microcavities, the splitting is most likely due to birefringence effects.

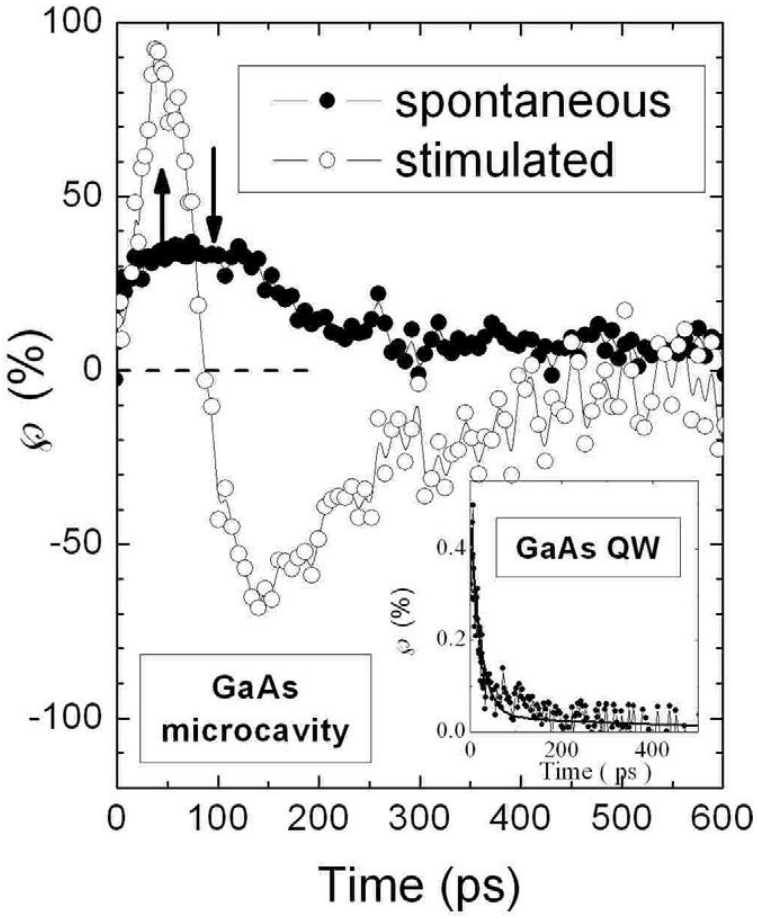

Fig. 4.2: Time evolution of the cavity-mode polarization of a GaAs based microcavity, with $Al_{0.25}Ga_{0.75}As$ resonators and $AlAs/Al_{0.35}Ga_{0.65}As$ DBRs for an excitation density of 7 W/cm^{-2} (solid points) and 40 W/cm^{-2} (open points). The arrows point to the maxima of the polarization. The inset shows a typical time evolution of the polarization in a GaAs quantum well for comparison.

Once the minimum negative value of $\wp_{circ}$ is reached, the polarization dynamics becomes slower: the remaining +1 spin population is too small to give rise to stimulation. Under these conditions, only the usual spin–flip mechanisms govern the polarization, which decreases steadily. It should be mentioned that, in the same Ref (37), excitation with σ^-polarized light was performed, yielding identical results to those of the σ^+ excitation: the sign reversal of the polarization is also observed for the

σ^- excitation and it is also the majority spin population (−1 in this case) the only one that undergoes stimulation.

Similar effects have been also observed in II–VI microcavities. In particular, Martín et al. (7) observed that after a non-resonant, σ^+-polarized excitation, the polarization dynamics of the polariton emission was strongly dependent on the detuning between the cavity and the bare exciton energies. Moreover, they observed pronounced oscillations of the polarization of the emission from the $k = 0$ states. An explanation of the observed polarization oscillations, proposed by Kavokin and coworkers,(45) is based on the pseudospin model and takes into account the splitting between the TE and TM modes of the cavity. They argued that linear polarization states, not circular ones, are the eigenstates of the system, and therefore due to their splitting, oscillations in the circular polarization are observed. However, TE-TM splitting is present only for $k \neq 0$, because at $k = 0$ the definition of TE and TM states loses its meaning. On the other hand, Martín et al. attributed the polarization to a splitting of circularly polarized $k = 0$ polaritons, suggesting that linear polarized states are the proper eigenstates at $k = 0$. We will see in the next section that the optical anisotropies of the structure may play an important role in determining the polarization properties of the emission in microcavities.

The time evolution of the circular polarization, as studied in Ref (7), is depicted in Fig. 4.3 for different detunings between the exciton and cavity modes. The open points correspond to the low excitation regime, which shows a dynamics of the polarization independent of the detuning and very similar to that found for bare excitons in QWs. The traces with the full symbols were taken at an excitation density at which the system is in the stimulated emission regime. At positive detunings, a positive degree of circular polarization is observed: $\wp_{circ}$ increases up to its maximum value, which can be as high as 90%, in 20 ps. The rise of the polarization (0 < t < 20 ps) has been interpreted as follows: the initial σ^+-polarized pulse creates a larger +1 spin population. A fast scattering process will bring all the photocreated excitons to the cavity mode before any spin relaxation can occur, which will result in a larger +1 spin population of $k \sim 0$ states at $t = 0$. This initial +1 spin population acted as a seed for the stimulated scattering process and therefore a large number of +1 spins were transferred to $k \sim 0$ states. The radiative recombination of this population resulted in a bigger σ^+-polarized emission, i.e. a very large positive polarization. After reaching the maximum difference in the spin populations $(t \sim 20\ \mathrm{ps})$, the +1 spin population decreases very quickly due to the fast emission dynamics, taking the polarization to zero $(20 < t < 40\ \mathrm{ps})$.

At $\delta \approx 0$, $\wp_{circ}$ showed a very short time interval of negative values, followed by a maximum, and eventually $\wp_{circ}$ decreased steadily to zero.

At negative detunings, $\wp_{circ}$ becomed basically negative, reaching values as large as −75% for δ ∼ −12 meV. In the case of $\delta < 0$, the experimental results may indicate that the initial σ^+-polarized pulse created a larger +1 spin population, which is reflected at $k \sim 0$ by the positive polarization at $t = 0$. The relaxation of the non-resonantly created polaritons towards $k \sim 0$, governed by the stimulated scattering, is probably more efficient for the −1 spin states than for +1 spin states, thus leading to an accumulation of −1 spin polaritons and resulting in a larger σ^--polarized emission and, therefore, a very large negative polarization. This negative polarization cannot be attributed to a resonant excitation of light-hole excitons, because the excitation energy was always kept at least 30 meV above the light–hole exciton resonance. Furthermore, such a resonant excitation would lead to a negative initial polarization degree, in contrast with the experimental findings.

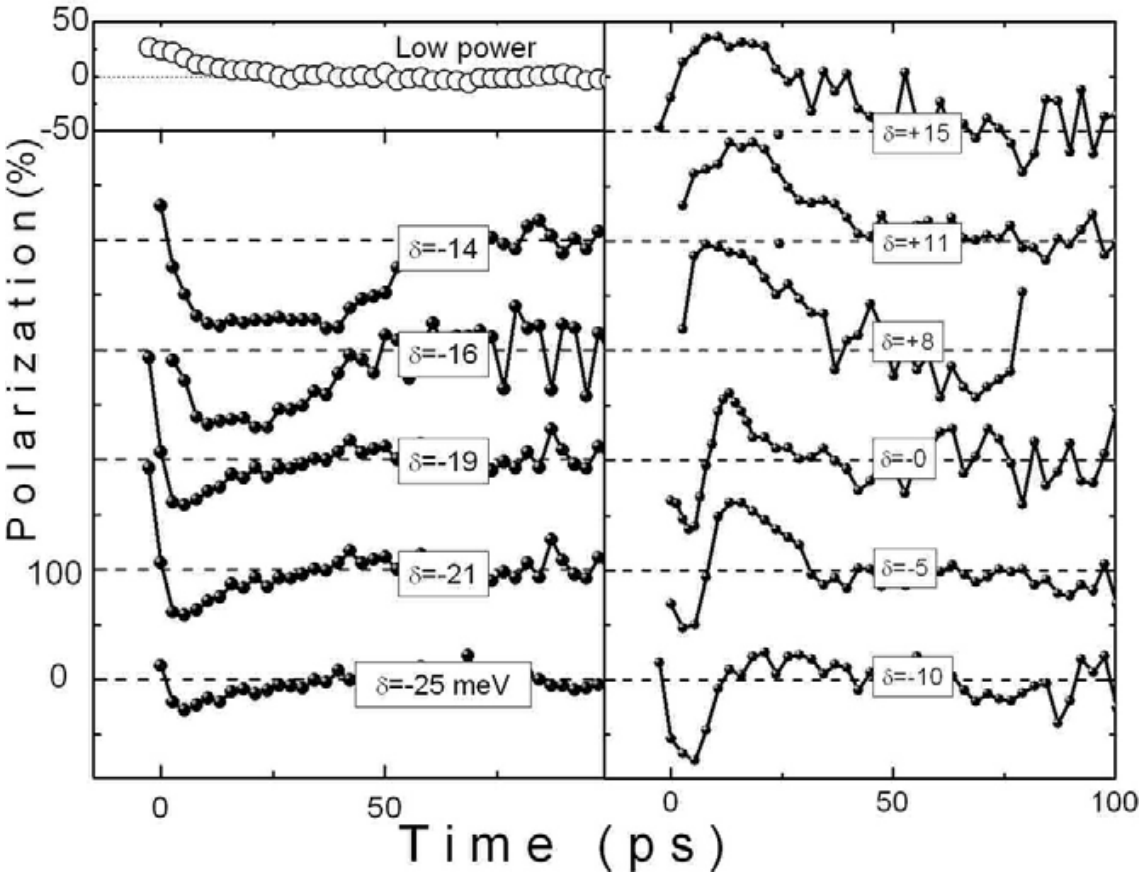

Fig. 4.3: Time evolution of the polarization for a λ/2 $Cd_{0.40}Mg_{0.60}Te$ microcavity at different detunings, from δ = −25 to +15 meV, for an excitation power density of 60 W cm−2 (solid points). A representative evolution at low power, 2 W cm−2, is depicted with open symbols. Each curve is offset by 100%, except the curves for low power and those corresponding to δ = −25 meV and δ = −10 meV.

It was proposed that the different scattering efficiencies might be related to an energy splitting, Δ, observed between the two circularly polarized components of the PL at very short times. This splitting, which is mirroring the different energies of the +1 and the −1 spin levels, has been found to show an increase with excitation power, saturating above the second threshold.(7)

In the case of δ > 0, the splitting was observed only for the UPB. At negative (positive) detunings, the energy of the −1 (+1) spin states at $k \sim 0$ was smaller than that of the +1 (−1) spin states. The energy splitting between the two spin states at $k \sim 0$ is likely to account for the reversal of the polarization degree of the PL with changing the exciton–cavity detuning. This splitting would be compatible with a decrease in the light–matter interaction strength for the majority polaritons (+1), which are initially created by the σ^+-polarized excitation, as compared to that of the minority (−1) polaritons. Actually, for negative (positive) detuning, the +1 spin states would lie above (below) the −1, accordingly with the reported results. However, experimental evidences showed that, with increasing excitation density, the initial blue shift of 0.5 meV is identical for both ±1 states, without any splitting, and is followed by a red shift of the −1 polaritons, while the +1 remain at the same energy.(46)

Therefore, the coupling strength of the +1 polaritons does not decrease, invalidating the previous argument. The fact that the splitting increased with excitation power density may indicate that it could originate from exciton–exciton interactions. An existing theory for bare excitons would qualitatively explain the splitting and the ±1 level ordering, as a result of exchange and vertex corrections to the self-energies,(19) but only for $\delta < 0$.

A quantum theory of momentum and spin relaxation of polaritons in microcavities, that takes into account self-consistently stimulated scattering and spin-relaxation processes, attributes the observed beats between right- and left-circularly polarized PL to a giant longitudinal–transverse splitting of the polaritons at the bottleneck that mixes their spin states and shows that the effect is strongly sensitive to the bosonic stimulation of polariton scattering.(45) The polarization oscillates with a period proportional to the inverse of the TE–TM splitting and the beats are sensitive to the pumping power due to the interplay between stimulated scattering and spin rotation. However, the theory does not reproduce the fact that the oscillations also take place at $k = 0$ and $\delta = 0$, where the TE–TM splitting should be zero.

In order to shed more light on the polarization properties at negative detunings, in the next section we will study the polarization of the PL emission under non resonant linear polarized excitation of a CdTe-based microcavity at negative detunings.

4.5 - Polarization dynamics varying the excitation power at negative detunings: pinning of the linear polarization degree

The sample under study is a $Cd_{0.4}Mg_{0.6}Te$ λ-microcavity with embedded CdTe quantum wells, with a Rabi splitting of 10 meV (for a detailed description of the sample, the reader can refer to section 3.1.1). The measurements are performed at a point of the sample characterized by an exciton-cavity detuning of $\delta \sim -11$ meV and at 5 K (Fig. 4.4). The optical excitation is done using 2-ps long pulses tuned to the first reflectivity minimum above the mirror's stop band and arrives to the sample almost at normal incidence (2,5°).

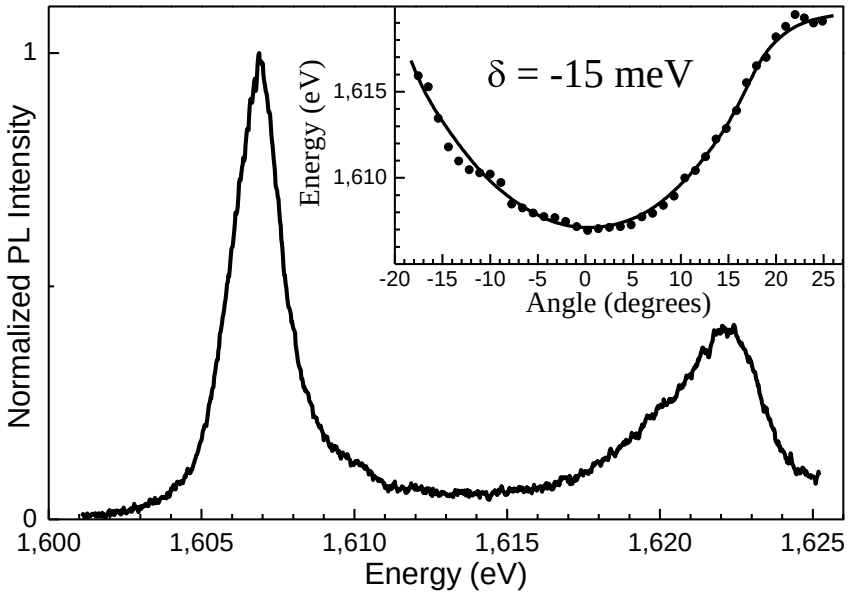

Fig. 4.4: Time-integrated PL spectrum for an excitation power of 0.5 mW at k = 0. Inset: Lower polariton branch dispersion relation, obtained varying the detection angle.

The photoluminescence is spectrally- and time-resolved by means of the streak camera coupled to a spectrograph, as described in sections 3.2 and 3.3. After linearly polarized excitation, either vertical (TE) or horizontal (TM), the PL is analyzed into its two linearly polarized components by means of a linear polarizer. A λ/4- plate is placed after the linear polarizer to avoid the polarization sensitivity of the gratings in the spectrometer. The degree of linear polarization is defined as in section 4.2. We will concentrate here on the dynamics of LPB population at $k = 0$, i.e. at zero degrees (angular resolution ±1º).

In our experiment, for excitation powers $P < 10$ mW, the system is in the spontaneous emission regime, and excitons and photons are strongly coupled.

Fig. 4.5(a) displays the time evolution of the LPB emission after TM polarized excitation. For the large negative detuning considered here, phonon scattering is strongly inhibited, and a reservoir of polaritons is formed just before the bottleneck region.

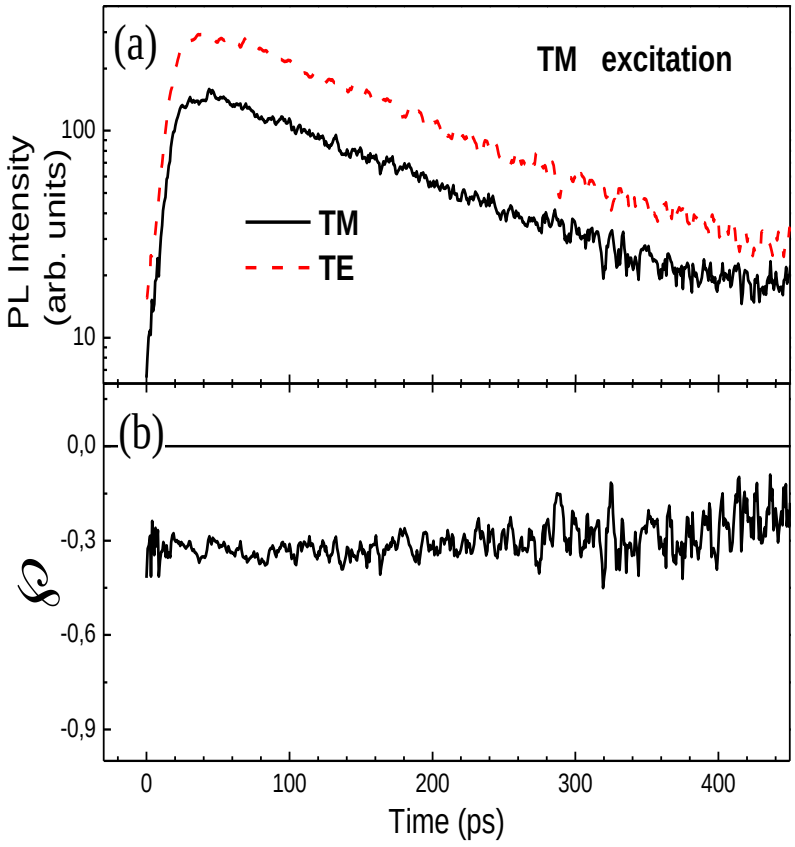

Fig. 4.5: Time evolution of the LPB emission at k = 0 for an excitation power of 0.5 mW after TM polarized excitation. Solid/dashed lines depict the TM/TE polarized PL component. (b) Time evolution of the degree of linear polarization $\wp_{lin}$ (see text). Same conditions as above.

Due to this bottleneck, the relaxation is considerably slowed down, with decay times of about 150 ps. In this regime there is no efficient mechanism available for polaritons to quickly surpass the bottleneck as polariton-phonon interaction is drastically reduced beyond the bottleneck. The integrated emission from the LPB displays a super-linear dependence on excitation, which indicates that relaxation is governed by spontaneous polariton-polariton scattering.(31) However, it is still possible to observe remarkable spin effects at $k = 0$. In Fig. 4.5(a) a large difference between the intensities of two linearly polarized PLs can be clearly observed, with the TE polarized emission (orthogonal to the excitation) being larger than the TM one. This difference is present all through the duration of the emission, leading to a negative linear polarization degree (depicted in Fig. 4.5(b)): a constant value $\wp_{lin} \sim -0.3$ is found, with a decay time of ~ 1 ns, much longer than the radiative lifetime.

Raising a bit further the excitation power $(10\ \mathrm{mW} < P < 20\ \mathrm{mW})$ changes drastically the recombination dynamics and the integrated emission from the LPB displays a strong super-linear dependence on power. Even though the polariton branches appear slightly shifted, excitons and photons are still strongly coupled.

Fig. 4.6(a) displays the time evolution of the two linearly polarized components of the non-linear emission from the $k = 0$ states of the LPB. The decay time has shortened to about 40 ps. This acceleration of the recombination dynamics is directly related with the activation of polariton-polariton stimulated scattering, which helps polaritons to efficiently overcome the relaxation bottleneck.

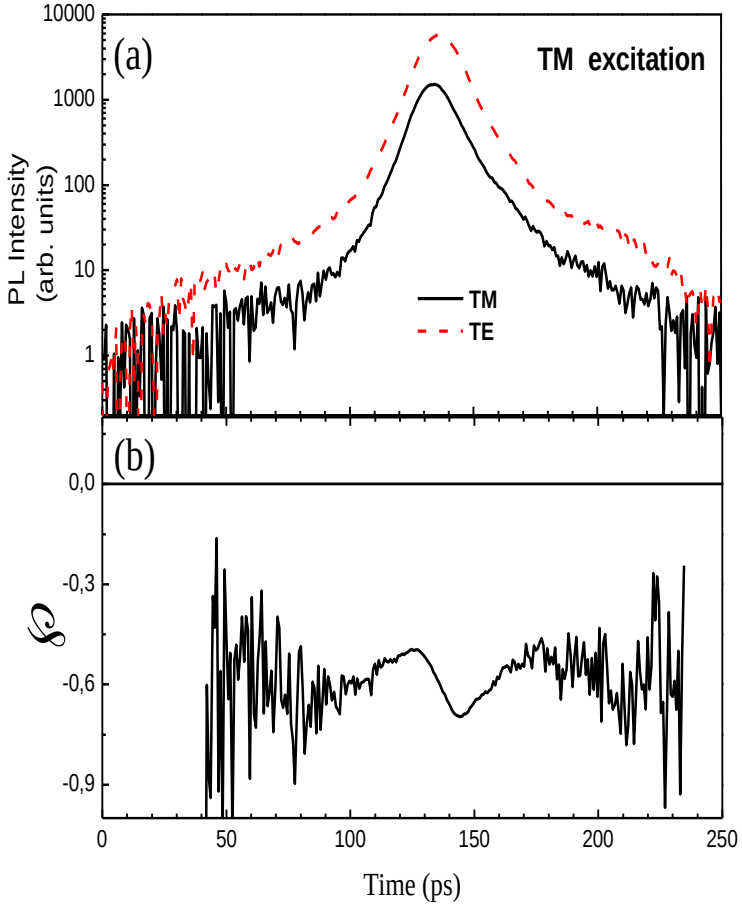

Fig. 4.6: Time evolution of the LPB emission at k = 0 for an excitation power of 10 mW, after TM polarized excitation. Solid/dashed lines depict the TM/TE polarized PL component. (b) Time evolution of the degree of linear polarization $\wp_{lin}$. Same conditions as in (a).

We observe that the intensity of the TE polarized PL is still much larger than the TM polarized one all along the duration of the emission. This difference between the intensities of the two linearly polarized components of the PL is enhanced with increasing the excitation power. The linear polarization degree, $\wp_{lin}$, in the stimulated regime is larger (Fig. 4.6(b), $\wp_{lin} = -0.5$) than in the spontaneous-emission regime (

Fig. 4.5(b), $\wp_{lin} = -0.3$), while the decay time of $\wp_{lin}$ still remains of the order of ~ 1 ns. On the other hand, marked oscillations of $\wp_{lin}$ can be seen after reaching the maximum linear polarization degree ($\wp_{lin} = -0.7$) for $t \neq 0$. These oscillations suggest that the spin eigenstates of the polaritons are not purely TE/TM states but elliptically polarized ones. The spin effects described above (freezing and oscillations of $\wp_{lin}$) have been described theoretically using the pseudospin model (see section 4.1), which considers the interplay between two different mechanisms: (i) a suppression of the spin relaxation (through exchange interaction, as described in Ref. (5)) for linearly polarized polaritons and (ii) an anisotropy of polariton-polariton stimulated scattering. The model also accounts for the 90º rotation of the polarization plane. In this model, however, the microcavities have been considered as optically isotropic objects having a perfect cylindrical symmetry. Anyway, recent works suggested that some built-in anisotropy may affect the polarization relaxation of polaritons.

To gain deeper insight into this polarization-plane rotation of 90°, we rotated by 90° the polarization of the excitation, from horizontal (TM) to vertical (TE), and repeated the experiments. Under these conditions, we find decay times which are comparable to those of Fig. 4.5(a) and Fig. 4.6(a) and a comparable excitation power threshold for the transition to the stimulated-emission regime. However, there is a significant difference between the two sets of data: the TE polarized emission is always stronger than the TM polarized one, regardless of the excitation polarization, and therefore in this case no rotation of the polarization plane occurs.

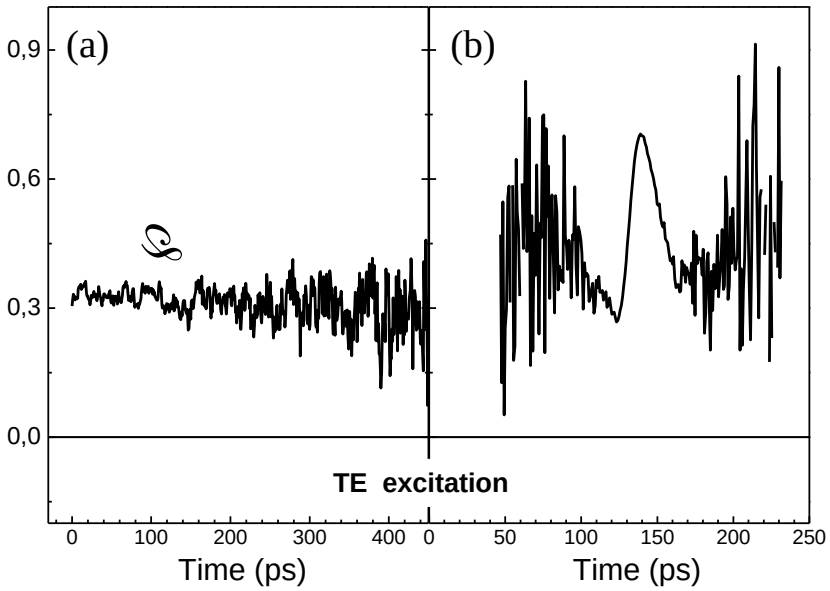

Fig. 4.7: Time evolution of the degree of linear polarization of the emission ($\wp_{lin}$) from the LPB at k = 0 for an excitation power of (a) 1 mW and (b) 15 mW after TE polarized excitation.

Under TE polarized excitation the linear polarization degree is positive and constant as long as there is any measurable signal (see Fig. 4.7(a)). The values of $\wp_{lin}$ are of the same order of magnitude for either excitation polarization ($\wp_{lin} \approx 0.3$ in the spontaneous regime and $\wp_{lin} \approx 0.5$ in the stimulated regime) and even the oscillations of the linear polarization degree at high excitation power are reproduced after vertically polarized excitation (Fig. 4.7(b)).

Further increase of the excitation power, beyond 20 mW, weakens the coupling of excitons and photons, the integrated emission intensity from $k = 0$ LPB states displays a linear dependence with power (saturation regime) and the non-linear effects observed in this regime are mainly due to the photonic part of polaritons. However, as for the spontaneous and stimulated regimes, the TE polarized emission is systematically larger than the TM polarized one, even though the experimental values of $\wp_{lin}$ are smaller than those obtained in the stimulated regime.

These experimental results show that the polarization of the emission is pinned to one of the crystallographic axes of the structure. This pinning has been confirmed by supplementary experiments performed with the sample rotated by 90°, returning to the same spot and using similar excitation conditions. In this case, we have found also that the preferential orientation for the polarization of the emission is rotated by 90° thus confirming the pinning along the same crystal axis as before. We interpret these striking effects, i.e. the long decay time of PL and the pinning of the linear polarization of the PL, as a consequence of a splitting of the polariton ground state, which is hinted in our time-resolved measurements, as shown in Fig. 4.8.

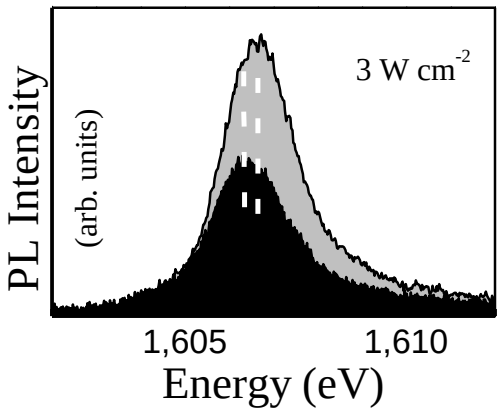

Fig. 4.8: Energy spectra of the two linearly polarized components (TM/TE in black/light-grey shades) of the time-integrated PL in the spontaneous regime $(3\ \mathrm{W/cm^2})$. The dashed white lines are guides to the eye.

This splitting can arise from either a splitting of the exciton resonance into a linearly polarized radiative doublet or a splitting of the photon eigenmodes of the cavity polarized TE and TM. It is worth mentioning that the longitudinal–transverse

splitting of exciton–polaritons, which is responsible for polariton spin relaxation in the excited states,(24) is always zero at $k = 0$.

Before discussing the possible origins of the splitting of the two linearly polarized polariton states at $k = 0$, let us see how it may affect the polarization properties of the light emission of the system. To get a simple idea of the scale of the effect, let us consider a polariton gas in thermal equilibrium. Of course, this is never the case for exciton–polaritons, for which the finite lifetime and the bottleneck effect are of crucial importance, but a simple thermodynamic treatment will allow us to understand qualitatively the observed phenomena. In the Boltzmann limit, the linear polarization degree of the emission from the ground state $\wp_{lin}(k = 0)$ can be estimated as(30)

$$\wp_{lin}(k = 0) = tanh\left(\frac{\Delta\varepsilon}{2k_B T}\right),$$

where $\Delta\varepsilon$ is the splitting between the $k = 0$ states with orthogonal linear polarizations. Taking $\Delta\varepsilon = 200$ μeV, and a temperature of 5 K, we obtain $\wp_{lin} = 0.46$, which is close to what we observe in our experiment.

The two linearly polarized components of the time-integrated PL show a small splitting between the two spectra, which cannot be measured with high accuracy because it is below the energy resolution of our streak camera and it is much smaller than the linewidth of the PL (see Fig. 4.8). Additional experiments performed under continuous-wave excitation confirm the existence of the energy splitting between the two linearly polarized components of the PL and show that the component lying at higher energies always has a larger intensity than that of the counter-polarized one, as shown in Fig. 4.9, indicating the non-thermal origin of the polarization.

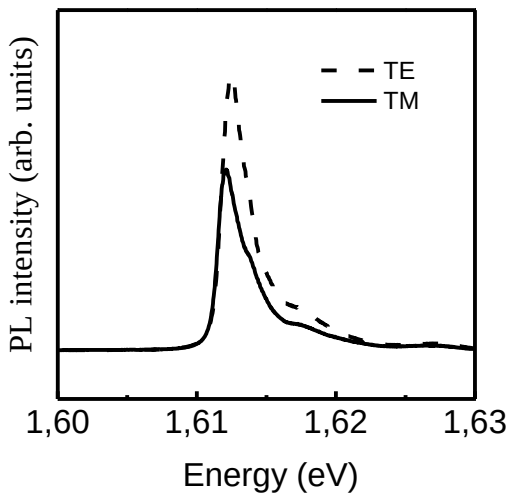

Fig. 4.9: Energy spectra, under cw excitation with TM polarized light, at 5 K, for TE (dashed lines) and TM (solid lines) detection.

The linear polarization $\wp_{lin}$ and the splitting $\Delta\varepsilon$ have similar temperature dependences, shown in Fig. 4.10. Both $\wp_{lin}$ and $\Delta\varepsilon$ monotonically decrease with T and both vanishes at $\mathrm{T} = 100\ \mathrm{K}$, thus confirming the direct relationship between the energy splitting and the observed linear polarization degree.

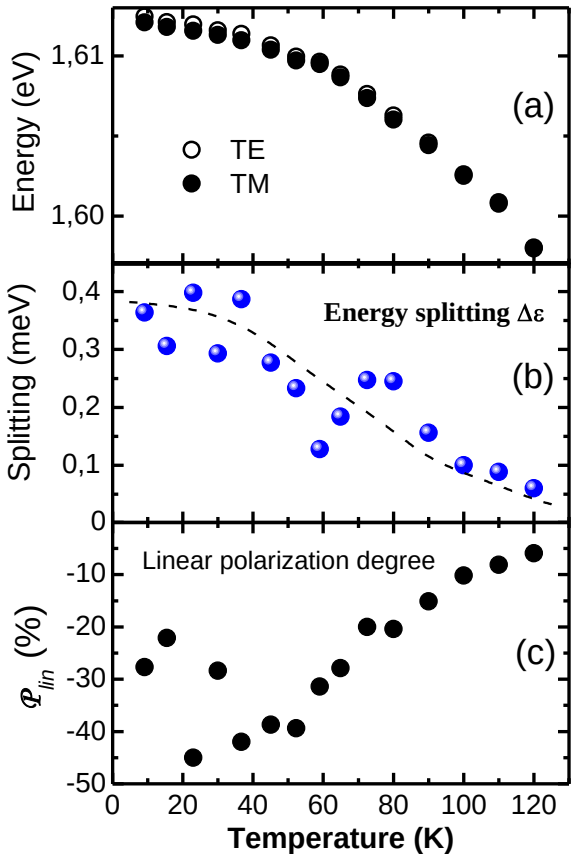

Fig. 4.10: (a) Energy of the PL at $k = 0$ for TE (dashed lines) and TM (solid lines) detection as a function of lattice temperature. (b) Splitting between the two orthogonal components of the emission as a function of temperature. (c) Linear polarization degree as a function of temperature. The data of (a), (b) and (c) are obtained under cw excitation with TM polarized light.

Above the stimulation threshold, due to the bosonic nature of exciton–polaritons, the degree of the linear polarization is significantly enhanced compared to what Eq. 4.3 yields. If the number of the particles in the ground state is N, in the limit $\mathrm{N} \gg 1$, the linear polarization degree reads

$$\wp_{lin}(k=0) = 1 - \frac{4}{N\left(e^{\Delta\varepsilon/kT} - 1\right)}.$$

Even for a very small splitting, the degree of polarization can be almost unity if the number of particles in the ground state is large enough. This is in agreement with our experimental observations showing a drastic increase of PL above the stimulation threshold when a large occupation of the ground state is obtained and the bosonic

effects play a major role, although the intensities of the emission are not determined by thermal occupation of the split levels.

The polariton eigenstate is a combination of an excitonic and a photonic eigenstate and the intermixing depends on the exciton–photon coupling constant and the detuning between bare exciton and photon modes. In principle, the splitting could arise from a splitting of the exciton state and different exciton–photon coupling constants in the two linear polarizations. The splitting of the exciton ground state is forbidden for symmetry reasons in an ideal symmetric QW, but becomes possible if the QW is asymmetric or if its interfaces have fluctuation islands oriented along the crystal axes.(47) The latter mechanism can hardly be the dominant one: we observe a drastic increase of PL above the stimulation threshold, which implies large occupation numbers that are incompatible with localized states. Let us now discuss the remaining possibility of the free exciton energy splitting, linked with an asymmetry along the growth axis of the QWs embedded in the cavity.(48) Under these circumstances, the exciton state becomes preferentially localized at one of interfaces which has a lower symmetry than the bulk crystal. This may happen due to built-in electric fields or simply due to the different scales of interface roughness at two interfaces. Such localization would break the symmetry of the exciton state in a QW and split the exciton states into x and y polarized states.

The value of splitting between x and y polarized states has been evaluated in Ref. (49), and can achieve $50-80\ \mu\mathrm{eV}$ for realistic QWs. Besides, the low symmetry of the structure induces a variation of the exciton oscillator strength in x and y linear polarizations. This results in a difference of the Rabi splittings for different linear polarizations. Anyway, at large negative detuning, the polariton splitting is strongly reduced with respect to the pure exciton splitting. In our case the polariton splitting will not be more than $10-20\ \mu\mathrm{eV}$. This is not enough for describing the linear polarization degree of emission that we observe in the spontaneous regime.

After ruling out the previously discussed source for the splitting, related with the excitonic part of polaritons, one is left with the effect of the photon eigenstates. Since the data presented here have been obtained under a large negative detuning ($\delta = -15\ \mathrm{meV}$), the polariton ground state is about 75% photon-like and therefore any effects associated with the photonic part of the polariton can be enhanced. Let us consider a small splitting between the bare photon modes of our microcavity in horizontal and vertical polarizations. This would mean that the Bragg mirrors or the cavity itself are slightly birefringent. The frequency ω_c of the uncoupled cavity mode is inversely proportional to the refractive index of the cavity material n_c. In an ideal λ-microcavity, $\omega_c = {}^{2\pi c}/_{n_c L_c}$, where L_c is the cavity width. Thus, a small change of n_c leads to a variation of the cavity frequency given by (30)

$$\omega_c \approx -\frac{\Delta n_c}{n_c}\omega_c.$$

To obtain a polariton splitting of $200\ \mu\mathrm{eV}$, the refractive index of the cavity should vary by about 0.02% between horizontal and vertical polarizations. Such a small variation can be a result of a weak uniaxial strain in the plane of the cavity. Anyway, further investigations are needed to achieve a quantitative explanation of the phenomena, which may arise from the interplay of different effects. In Ref. (50), for example, Brunetti et. al. have studied the linear dichroism in a GaAs microcavity and found that the exciton–polariton ground states were split into a linearly polarized doublet. These results were explained in the framework of the model where the splitting results from both the polarization dependent Rabi coupling and the splitting of the bare cavity mode.

It is worth to notice that the crystallographic direction play an important role even under resonant pumping: in Ref (51) the spatial properties and coherence of the high density phase of polaritons in a microcavity optical parametric oscillator (see chapter 5) have been studied, finding marked lateral variations in the transmission spectra. A partial alignment of these spatial features along the major crystallographic axes in the disordered photonic potential was seen. In that case, the samples are grown without any deliberate wedge, confirming that the anisotropy may arise in the mirrors.

Evidence for [110] oriented disorder has previously been reported also by Gurioli et al.,(52) Houdré et al.(53) and Langbein et al.(54) in resonant Rayleigh scattering and secondary emission measurements, and suggested to arise in Refs. (52) and (54) from the onset of lattice relaxation in the Bragg mirrors. Very clear [110] fluctuations in reflectivity have also been observed in high quality GaAs-based microcavities,(55) suggesting the universality of in-plane fluctuations in the photonic potential.

Finally we note that spatial patterning has also been observed for the high density coherent phase created under non-resonant excitation (56). Polarization properties of the emission seem to be strongly related with spatial anisotropy of the system, hindering the polarization direction to be randomly selected by a spontaneous symmetry breaking mechanism. Elucidation of the differing but related physics in the resonant and non-resonant case will be an interesting challenge in the next few years.

In conclusion, these experiments demonstrate that the conservation of the spin coherence is compatible with fast relaxation processes, and indicates that in future polariton lasers the linear polarization of emission could be stabilized and linked to one of the crystal axes due to the described pinning effect.

4.6 – Summary

In this Chapter we have presented experimental results on the time-resolved PL in CdTe microcavities, at negative detunings, under non-resonant linear polarized excitation. At low excitation density the system remains in the strong coupling regime and the polariton emission at $k = 0$ is determined by the exciton formation and polariton relaxation from the bottleneck states. The linear polarization degree of the emission is frozen (lifetime longer than 2 ns) at a constant value of $\wp_{lin} = 0.3$.

At higher excitation densities, stimulated scattering from the reservoir states towards the ground state accelerates the polariton dynamics and increases the polarization degree ($\wp_{lin} = 0.5$). The conservation of the spin orientation during the fast relaxation due to stimulated polariton scattering is explained in terms of an energy splitting presents at $k = 0$ between the TE- and TM-polarized polariton states. This splitting is most likely produced by a weak uniaxial strain in the plane of the cavity, which results in a pinning of the linear polarization degree along one of the crystallographic axis of the structure and does not depend on the polarization of the exciting beam.

Bibliography:

[1] R. J. Elliot. *Theory of the Effect of Spin-Orbit Coupling on Magnetic Resonance in Some Semiconductors*. Phys. Rev. **96,** 266 (1954).

[2] Y. Yafet (1963) in *Solid State Physics*, eds. Seitz, F. & Turnbull, D. (Academic Press, New York).

[3] G. E. Pikus, and G. L. Bir. *Exchange interaction in excitons in semiconductors*. Soviet Physics JETP **33,** 108 (1971).

[4] M. I. D'yakonov, and V. I. Perel'. *Spin relaxation of conduction electrons in noncentrosymmetric semiconductors*. Sov. Phys.-Solid State **13,** 3023 (1972).

[5] M. Z. Maialle, E. A. d. A. e. Silva, and L. J. Sham. *Exciton spin dynamics in quantum wells*. Phys. Rev. B **47,** 15776 (1993).

[6] G. Panzarini, L. C. Andreani, A. Armitage, D. Baxter, M. S. Skolnick, V. N. Astratov, J. S. Roberts, A. V. Kavokin, M. R. Vladimirova, and M. A. Kaliteevski. *Exciton-light coupling in single and coupled semiconductor microcavities: Polariton dispersion and polarization splitting*. Phys. Rev. B **59,** 5082 (1999).

[7] M. D. Martin, G. Aichmayr, L. Viña, and R. André. *Polarization Control of the Nonlinear Emission of Semiconductor Microcavities*. Phys. Rev. Lett. **89,** 077402 (2002).

[8] P. G. Lagoudakis, P. G. Savvidis, J. J. Baumberg, D. M. Whittaker, P. R. Eastham, M. S. Skolnick, and J. S. Robert. *Stimulated spin dynamics of polaritons in semiconductor microcavities*. Physical Review B **65,** 161310 (2002).

[9] M. I. D'yakonov, and V. I. Perel' (1984) in *Optical Orientation*, eds. Maier, F. & B.P. Zakharchenya (Elsevier Science Publishers, Amsterdam), pp. 11.

[10] G. E. Pikus, and A. N. Titkov (1984) in *Optical Orientation*, eds. Maier, F. & Zakharchenya, B. P. (Elsevier Science Publishers, Amsterdam), pp. 73.

[11] J. Rudolph, D. Hägele, H. M. Gibbs, G. Khitrova, and M. Oestreich. *Laser threshold reduction in a spintronic device*. Appl. Phys. Lett. **82,** 4516 (2003).

[12] S. Hallstein, J. D. Berger, M. Hilpert, H. C. Schneider, W. W. Rühle, F. Jahnke, S. W. Koch, H. M. Gibbs, G. Khitrova, and M. Oestreich. *Manifestation of coherent spin precession in stimulated semiconductor emission dynamics*. Phys. Rev. B **56,** R7076 (1997).

[13] P. G. Savvidis, J. J. Baumberg, R. M. Stevenson, M. S. Skolnick, D. M. Whittaker, and J. S. Roberts. *Angle-resonant stimulated polariton amplifier*. Phys. Rev. Lett. **84,** 1547 (2000).

[14] R. M. Stevenson, V. N. Astratov, M. S. Skolnick, D. M. Whittaker, M. Emam-Ismail, A. I. Tartakovskii, P. G. Savvidis, J. J. Baumberg, and J. S. Roberts. *Continuous Wave Observation of Massive Polariton Redistribution by Stimulated scattering in Semiconductor Microcavities*. Phys. Rev. Lett. **85,** 3680 (2000).

[15] A. I. Tartakovskii, D. N. Krizhanovskii, and V. D. Kulakovskii. *Polariton-polariton scattering in semiconductor microcavities: Distinctive features and similarities to the three-dimensional case*. Phys. Rev. B **62,** 13298 (2000).

[16] P. G. Savvidis, J. J. Baumberg, R. M. Stevenson, M. S. Skolnick, D. M. Whittaker, and J. S. Roberts. *Asymmetric angular emission in semiconductor microcavities*. Phys. Rev. B **62,** R13278 (2000).

[17] A. Kavokin, P. G. Lagoudakis, G. Malpuech, and J. J. Baumberg. *Polarization rotation in parametric scattering of polaritons in semiconductor microcavities*. Phys. Rev. B **67,** 195321 (2003).

[18] L. Viña, L. Muñoz, E. Perez, J. Fernández-Rossier, C. Tejedor, and K. Ploog. *Spin splitting in a polarized quasi-two-dimensional exciton gas*. Phys. Rev. B **54,** R8317 (1996).

[19] J. Fernández-Rossier, C. Tejedor, L. Muñoz, and L. Viña. *Polarized interacting exciton gas in quantum wells and bulk semiconductors*. Phys. Rev. B **54,** 11582 (1996).

[20] S. Savasta, O. Di Stefano, and R. Girlanda. *Spectroscopy of four-particle correlations in semiconductor microcavities*. Phys. Rev. B **64,** 073306 (2001).

[21] A. V. Kavokin, M. R. Vladimirova, M. A. Kaliteevski, O. Lyngnes, J. D. Berger, H. M. Gibbs, and G. Khitrova. *Resonant Faraday rotation in a semiconductor microcavity*. Phys. Rev. B **56,** 1087 (1997).

[22] D. N. Krizhanovskii, D. Sanvitto, I. A. Shelykh, M. M. Glazov, G. Malpuech, D. D. Solnyshkov, A. Kavokin, S. Ceccarelli, and M. S. Skolnick. *Rotation of the plane of polarization of light in a semiconductor microcavity*. Phys. Rev. B **73,** 073303 (2006).

[23] K. V. Kavokin, P. Renucci, T. Amand, X. Marie, P. Senellart, J. Bloch, and B. Sermage. *Linear polarisation inversion: A signature of Coulomb scattering of cavity polaritons with opposite spins*. Phys. stat. sol. (c) **0002**(2004).

[24] K. V. Kavokin, I. A. Shelykh, A. V. Kavokin, G. Malpuech, and P. Bigenwald. *Quantum Theory of Spin Dynamics of Exciton-Polaritons in Microcavities*. Phys. Rev. Lett. **92,** 017401 (2004).

[25] I. A. Shelykh, G. Malpuech, K. V. Kavokin, A. V. Kavokin, and P. Bigenwald. *Spin dynamics of interacting exciton polaritons in microcavity*. Phys. Rev. B **70,** 115301 (2004).

[26] L. Klopotowski, A. Amo, M. D. Martin, L. Viña, and R. André. *Polarization dynamics of microcavity polaritons: Three excitation regimes*. phys. stat. sol. (a) **202,** 357 (2005).

[27] A. Imamoglu, R. J. Ram, S. Pau, and Y. Yamamoto. *Nonequilibrium condensate and lasers without inversion: Exciton-polariton lasers*. Phys. Rev. A **53,** 4250 (1996).

[28] J. Kasprzak, R. Andre, D. Le Si, I. A. Shelykh, A. V. Kavokin, G. R. Yuri, K. V. Kavokin, and G. Malpuech. *Build up and pinning of linear polarization in the Bose condensates of exciton polaritons*. Physical Review B (Condensed Matter and Materials Physics) **75,** 045326 (2007).

[29] R. Balili, V. Hartwell, D. Snoke, L. Pfeiffer, and K. West. *Bose-Einstein Condensation of Microcavity Polaritons in a Trap*. Science Magazine **316,** 1007 (2007).

[30] L. Klopotowski, M. D. Martin, A. Amo, L. Viña, I. A. Shelykh, M. M. Glazov, G. Malpuech, A. Kavokin, and R. André. *Optical anisotropy and pinning of the linear polarization of light in semiconductor microcavities*. Solid State Communications **139,** 511 (2006).

[31] P. Senellart, J. Bloch, B. Sernage, and J. Y. Marzin (2000) in *Phys. Rev. B*, Vol. 62, pp. R16263.

[32] A. Alexandrou, G. Bianchi, E. Péronne, B. Hallé, F. Boeuf, R. André, R. Romestain, and L. S. Dang. *Stimulated scattering and its dynamics in semiconductor microcavities at 80 K under nonresonant excitation conditions*. Phys. Rev. B **64,** 233318 (2001).

[33] M. Saba, C. Ciuti, J. Bloch, V. Thierry-Mieg, R. Andre, L. S. Dang, S. Kundermann, A. Mura, G. Bongiovanni, J. L. Staehli, and B. Deveaud. *High-temperature ultrafast polariton parametric amplification in semiconductor microcavities*. Nature **414,** 731 (2001).

[34] J. Kasprzak, M. Richard, S. Kundermann, A. Baas, P. Jeambrun, J. M. J. Keeling, F. M. Marchetti, M. H. Szymanska, R. André, J. L. Staehli, V. Savona, P. B. Littlewood, B. Deveaud, and L. S. Dang. *Bose_Einstein condensation of exciton polaritons*. Nature **443,** 409 (2006).

[35] A. I. Tartakovskii, V. D. Kulakovskii, D. N. Krizhanovskii, M. S. Skolnick, V. N. Astratov, A. Armitage, and J. S. Roberts. *Nonlinearities in emission from the lower polariton branch of semiconductor microcavities*. Phys. Rev. B **60,** 11293 (1999).

[36] I. A. Shelykh, L. Vina, A. V. Kavokin, N. G. Galkin, G. Malpuech, and R. Andre. *Non-linear coupling of polariton and dark exciton states in semiconductor microcavities*. Solid State Communications **135,** 1 (2005).

[37] M. D. Martin, L. Viña, J. K. Son, and E. E. Mendez. *Spin dynamics of cavity polaritons*. Solid State Commun. **117,** 267 (2001).

[38] P. Renucci, T. Amand, X. Marie, P. Senellart, J. Bloch, B. Sermage, and K. V. Kavokin. *Microcavity polariton spin quantum beats without a magnetic field: A manifestation of Coulomb exchange in dense and polarized polariton systems*. Phys. Rev. B **72,** 075317 (2005).

[39] G. Panzarini, L. C. Andreani, A. Armitage, D. Baxter, M. S. Skolnick, V. N. Astratov, J. S. Roberts, A. V. Kavokin, M. R. Vladimirova, and M. A. Kaliteevski. *Cavity-polariton dispersions and polarization splitting in single and coupled semiconductor microcavities*. Phys. Solid State **41,** 1223 (1999).

[40] M. D. Martín, L.Viña, and E. E. Mendez. *Ultrafast light-polarization dynamics in semiconductor microcavities*. Solid State Commun. **119,** 259 (2001).

[41] L. S. Dang, D. Heger, R. André, F. Boeuf, and R. Romestain. *Stimulation of polariton photoluminescence in semiconductor microcavity*. Phys. Rev. Lett. **81,** 3920 (1998).

[42] S. Schmitt-Rink, D. S. Chemla, and D. A. B. Miller. *Theory of transient excitonic optical nonlinearities in semiconductor quantum-well structures*. Phys. Rev. B **32,** 6601 (1985).

[43] W. Langbein, R. Zimmermann, E. Runge, and J. M. Hvam. *Spin Relaxation without Coherence Loss: Fine-Structure Splitting of Localized Excitons*. physica status solidi (b) **221,** 349 (2000).

[44] R. Zimmermann, W. Langbein, E. Runge, and J. M. Hvam. *Localized excitons in quantum wells show spin relaxation without coherence loss*. Physica E: Low-dimensional Systems and Nanostructures **10,** 40 (2001).

[45] K. V. Kavokin, I. A. Shelykh, A. V. Kavokin, G. Malpuech, and P. Bigenwald. *Quantum theory of spin dynamics of exciton-`polaritons in microcavities*. Physical Review Letters **92,** 017401 (2004).

[46] G. Aichmayr, M. D. Martín, and R. André. *Dispersion mapping of spin-dependent polariton dynamics in CdTe microcavities*. Semiconductor Science and Technology **18,** S368 (2003).

[47] S. V. Gupalov, E. L. Ivchenko, and A. V. Kavokin. *Fine structure of localized exciton levels in quantum wells*. JETP **86,** 388 (1998).

[48] A. Kudelski, A. Golnik, J. A. Gaj, F. V. Kyrychenko, G. Karczewski, T. Wojtowicz, Y. G. Semenov, O. Krebs, and P. Voisin. *Interface profiles and in-plane anisotropy in common anion type-I$Cd_{1-x}Mg_xTe/CdTe/Cd_{1-x}Mn_xTe$ heterostructures studied by reflectivity*. Phys. Rev. B **64,** 045312 (2001).

[49] E. L. Ivchenko, A. Y. Kaminski, and U. Rössler. *Heavy-light hole mixing at zinc-blende (001) interfaces under normal incidence*. Phys. Rev. B **54,** 5852 (1996).

[50] A. Brunetti, M. Vladimirova, S. Cronenberger, D. Scalbert, M. Nawrocki, and J. Bloch. *Linear dichroism in a GaAs microcavity*. Superlattices and Microstructures **41,** 429 (2007).

[51] M. S. Skolnick, D. Sanvitto, D. N. Krizhanovskii, A. P. D. Love, D. M. Whittaker, and J. S. Roberts. *Spatial properties and coherence of the high density phase in the microcavity optical parametric oscillator*. physica status solidi (b) **243,** 3741 (2006).

[52] M. Gurioli, F. Bogani, D. S. Wiersma, P. Roussignol, G. Cassabois, G. Khitrova, and H. Gibbs. *Experimental study of disorder in a semiconductor microcavity*. Phys. Rev. B **64,** 165309 (2001).

[53] R. Houdré, C. Weisbuch, R. P. Stanley, U. Oesterle, and M. Ilegems. *Coherence effects in light scattering of two-dimensional photonic disordered systems: Elastic scattering of cavity polaritons*. Physical Review B **61,** R13333 LP (2000).

[54] W. Langbein. In: *Proceedings of the 26th International Conference on the Physics of Semiconductors*, Edinburgh (2002).

[55] D. Sanvitto, A. Daraei, A. Tahraoui, M. Hopkinson, P. W. Fry, D. M. Whittaker, and M. S. Skolnick. *Observation of ultrahigh quality factor in semiconductor microcavity*. Appl. Phys. Lett. **86,** 191109 (2005).

[56] M. Richard, J. Kasprzak, R. A. R. Romestain, L. S. Dang, G. Malpuech, and A. Kavokin. *Experimental evidence for nonequilibrium Bose condensation of exciton polaritons*. Phys. Rev. B **72,** 201301 (2005).

Chapter 5

High-density polariton systems under non-resonant excitation

5.1 – Introduction: strong-coupling and Bose-Einstein condensation

We have seen in Chapter 2 that light-matter interaction in semiconductor microcavities is usually described in the framework of the weak- and strong-coupling regimes.

If the cavity-mirrors reflectivity is large enough and the exciton linewidth sufficiently small, exciton and photon are strongly coupled and a coherent energy transfer between them occurs with the so-called Rabi frequency Ω_R. In the SC regime, at detuning $\delta = 0$, the degeneracy of the exciton and photon levels breaks into the lower (LPB) and upper (UPB) polariton branches, which are separated by a Rabi splitting (Eq 2.20):

$$Rabi\ Splitting = 2\sqrt{\hbar^2\Omega_{\mathrm{R}}^2 - \frac{\hbar^2}{4}(\gamma_c - \gamma_x)^2}$$

where $\hbar\Omega_R$ is the light-matter coupling term of Eq 2.14, proportional to the exciton oscillator strength, f_{exc}^{osc}, while γ_c and γ_x are the cavity linewidth and the non-radiative exciton linewidth, respectively. The dispersion relations of the polaritons are strongly modified with respect to those of the bare modes and present a deep minimum at the bottom of the LPB. The effective mass at these points is therefore very small, resulting in a small density of states near the ground state. This allows polaritons to form a Bose condensate at relatively high temperature, and, in principle, a polariton

laser that does not require population inversion is possible. On the contrary, in the WC regime the light-matter interaction is well described by a perturbative approach: the energies of the coupled modes are very similar to those of the bare modes and the gap between UPB and LPB vanishes. In the WC regime, polaritons properties are indeed very similar to those of photons in a vertical-cavity-surface-emitting-laser (VCSEL).

As mentioned, one of the most interesting properties of polaritons in the strong coupling regime is their capability to form a Bose-Einstein condensate (BEC). When exciton and photon are strongly coupled, the LPB presents a deep minimum at $k_{||} = 0$, as shown in fig 4.1 for the case of a GaAs microcavity at $\delta = 0$. At this point, the polariton masses are of the order of $m = 10^{-6} m_0$, with m_0 the free electron mass.

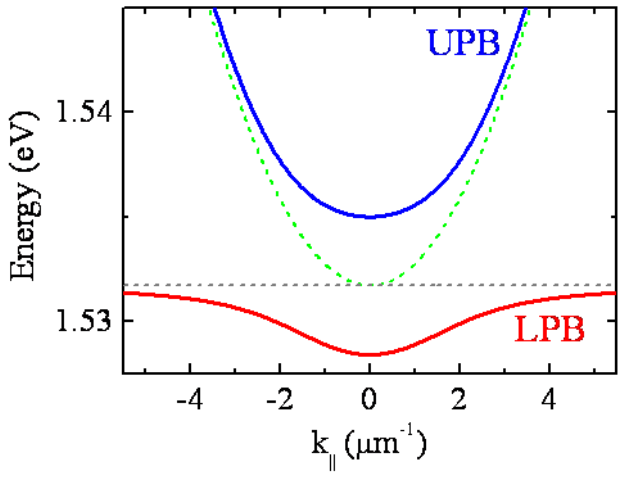

Fig. 5.1: Upper (UPB) and lower (LPB) polariton branch of a GaAs microcavity at δ=0. The bare exciton and photon dispersions are depicted in the figure with dashed lines.

The density of states g_{2D} of a two dimensional system, like exciton-polaritons in a microcavity, is given by

$$g_{2D}(E) = \frac{m}{\pi\hbar^2}\Theta(E)$$

where m is the effective polariton mass and $\Theta(E)$ is the Heaviside step function (we have set the zero value of energy at the bottom of the LPB). This implies that inside the polariton trap (at the bottom of the LPB, for $\delta \leq 0$), the polariton density of states is very small as compared to other systems which feature BEC, like atoms (atomic mass is of the order of 10^9 times larger than polariton mass). This property has very important consequences, because stimulation effects, which cause the condensation of bosons in a single quantum state, require a minimum occupancy factor that depends on temperature and on the density of states. The heavy mass of the atomic bosons employed in BEC studies implies working at sub-μK temperatures.

The small polariton effective mass allows the transition to a Bose-condensed phase to take place at much higher temperatures, from $10\ \mathrm{K}$ to $300\ \mathrm{K}$.

On the other side, excitons can be considered as composite bosons if their density is sufficiently small to disregard the interaction between the fermionic parts of different excitons. Actually, when the density of exciton is increased, not only the inter-exciton distance but also the carrier screening is dramatically altered. Indeed, at high density, the Coulomb interaction between the electron-hole pair of an exciton is screened by the charged particles which compose the neighbor excitons. As a consequence, the exciton eigenfunctions change, resulting in a decrease of the exciton oscillator strength and consequently of the exciton-photon coupling (see Eq. 2.14 and 2.15). This establishes an important limit to the density of polaritons in order to keep the system in the strong coupling regime. Polariton BEC is possible only if the critical density required to start the stimulated scattering process (occupancy factor equal to 1) is smaller than the density at which the transition from the strong- to the weak-coupling regime takes place.

Under resonant pumping of the LPB, such stimulate polariton scattering to the ground state ($k_{\|} = 0$) has been observed in the strong coupling regime, because the resonant excitation permits direct population of the polariton region with low density of states (small k in the LPB), and allows state occupancies greater than one to be achieved at total injected densities two or three orders of magnitude below the densities at which exciton screening, and the loss of strong coupling, occurs. Anyway, in this case it is not possible for polaritons to reach a thermalized distribution, and the large population created by the resonant exciting beam in a state different from the ground state is always present as a driving external field, so polariton BEC in the resonant case can only be obtained in an out-of-equilibrium environment. A deeper discussion on the resonant excitation configuration and polariton BEC properties will be found in Chapter 5. Here, we will consider the non resonant excitation scheme, similar to the conditions under which a real semiconductor device under electrical injection may be expected to operate. In non-resonant experiments, the main aim is to observe spontaneous coherent processes emerging from incoherent injection of polaritons: polariton degeneracy at the ground state, final state stimulation and ultimately polariton coherence and BEC.

5.2 – Non-resonant experiments

Under non resonant conditions, with excitation energies above the stop band of the Bragg mirrors of the microcavity, free electron-hole pairs are created in the QW. In less than 1 picosecond,(1) electrons and holes achieve thermalized distributions in

the QWs. Simultaneously, polaritons formation takes place, populating the UPB and LPB. As depicted in Fig. 5.2, polaritons rapidly relax by LO phonon emission until they reach the bottleneck region. Relaxation from the bottleneck region to the bottom of the polariton trap is a slow process at low excitation densities, as it requires the simultaneous relaxation of a significant amount of energy and momentum. At the bottleneck region, LO-phonon assisted scattering process cannot take place because of energy and momentum conservation restrictions, and only polariton-polariton scattering and acoustic phonon interaction can contribute to the polariton relaxation. Competition between slow acoustic phonon relaxation (times of ns) and fast escape from the cavity by photon leakage through the Bragg mirrors (orders of ps) leads to the formation of the relaxation bottleneck. As a consequence, at low excitation powers and $\delta \leq 0$, a large exciton population (exciton reservoir) builds up in the exciton reservoir region, while the states near $k = 0$ are strongly depleted. The presence of the bottleneck inhibits very strongly the achievement of high states occupancies at the bottom of the LPB.

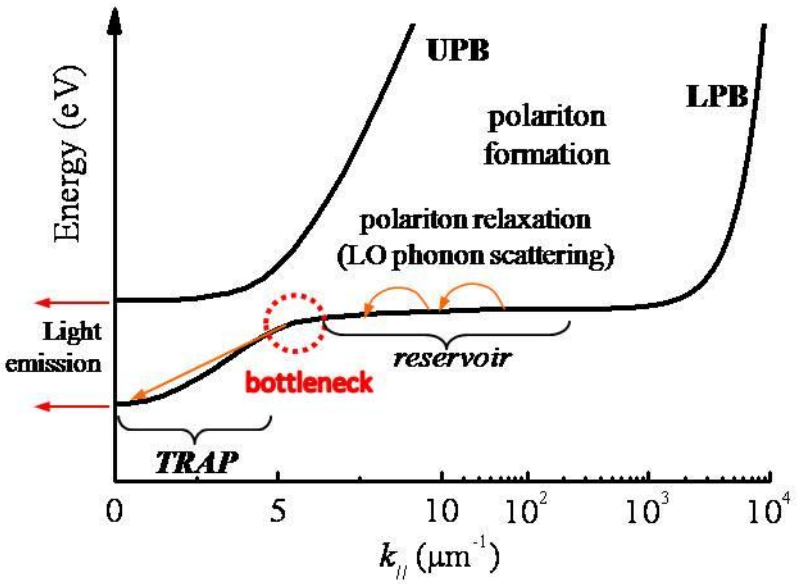

Fig. 5.2: In the strong coupling regime, non-resonant excitation create polariton at high energies which relax towards the reservoir, where they accumulate due to the slow relaxation rate of polaritons at the inflection point of the LPB (bottleneck region).

However, with increasing excitation densities, polariton-polariton scattering can provide an efficient channel to transfer polaritons from the reservoir towards $k = 0$. We will see in the next chapter that polariton-polariton scattering is responsible for the population of the ground state even in the case of resonant configuration experiments, demonstrating the general validity of the presented scheme. The difference lies in the fact that, under nonresonant pumping, a high density of

polaritons accumulates in the bottleneck region, and the relaxation towards the bottom of the LPB is strongly slowed down. Due to the photonic content of the LPB states with low momenta, which is close to 50% at $\delta = 0$, the polariton lifetime is of the order of 1-10 ps in standard GaAs and CdTe based microcavities. The much longer relaxation time of polaritons from the reservoir, hinders occupation factors at k=0 above unity to be achieved. Faster relaxation times from the reservoir are required to trigger the stimulated scattering. The usual strategy has been to increase the excitation density until the occupation of the ground state is high enough, as long as the strong coupling regime is not destroyed by the high carrier density. Actually, the first observation of nonlinear emission from the LPB at $k = 0$ in a GaAs based microcavity, under nonresonant excitation,(2) was interpreted as due to the stimulated scattering of polaritons in SC regime, while further experiments showed that the threshold for nonlinear emission occurred in that case after the crossover to the weak-coupling regime.(3) Nonlinear emission in the weak-coupling regime is analogous to the photon lasing in a VCSEL. Once the SC is lost, the bare exciton and photon dispersion relations are recovered, and the energy states of the system, shown in Fig. 5.3, are given by those of the first electron and heavy-hole subbands, decoupled to the photon cavity modes.

As depicted in the figure, non resonant excitation results in a four level system: population inversion between levels 3 and 2 is easily achieved due to the efficient electron and hole relaxation towards, respectively, the bottom and the top of their bands. In particular, when $\delta = 0$, the Bragg mirrors act as a very efficient resonator, with the photonic mode very close to the bandgap energy, and photonic lasing switches on with a very low power threshold.(2, 4, 5)

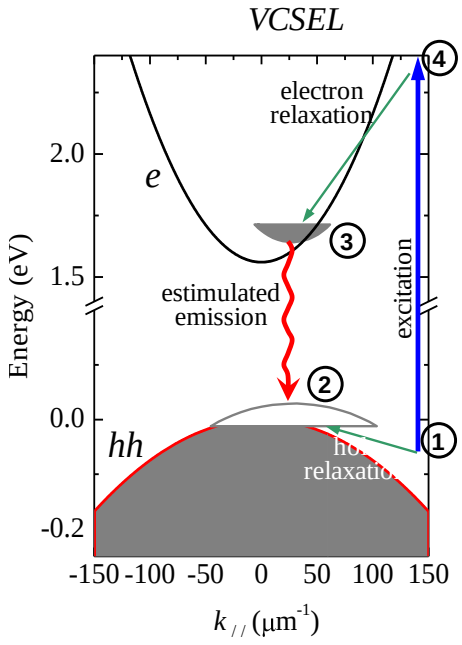

Fig. 5.3: Schematic structure of the 4-level lasing system in a microcavity in the weak coupling regime above the threshold for photon lasing (VCSEL regime).

This photon laser is conceptually different from a polariton laser (*plaser*):(6) optical emission in a *plaser* would come from the leakage out of the microcavity of a BEC of polaritons at the bottom of the LPB. Due to the bosonic nature of polaritons, the polariton-polariton scattering from the reservoir to the bottom of the momentum trap ($k = 0$) is stimulated by final state occupation greater than unity.

The condensed polaritons are in a well defined quantum state, and, when they leak out of the cavity, they present very similar characteristics to those of a conventional photon laser (monochromaticity, coherence, directionality). Unlike in a photon laser, however, a *plaser* would not require population inversion, and could operate without an excitation power threshold.(6)

Bosonic stimulation in microcavity under non resonant pumping was first observed in CdTe samples, (7) containing of 16 QWs with a Rabi splitting of 23 meV. Two distinct stimulation thresholds were found increasing the intensity of cw non-resonant pumping. Above the first threshold, nonlinear emission at energies close to the bottom of the LPB was clearly seen. The second threshold, at higher pump intensities, was connected with the electron-hole lasing mechanism in the weak-coupling regime (see Fig. 5.4).

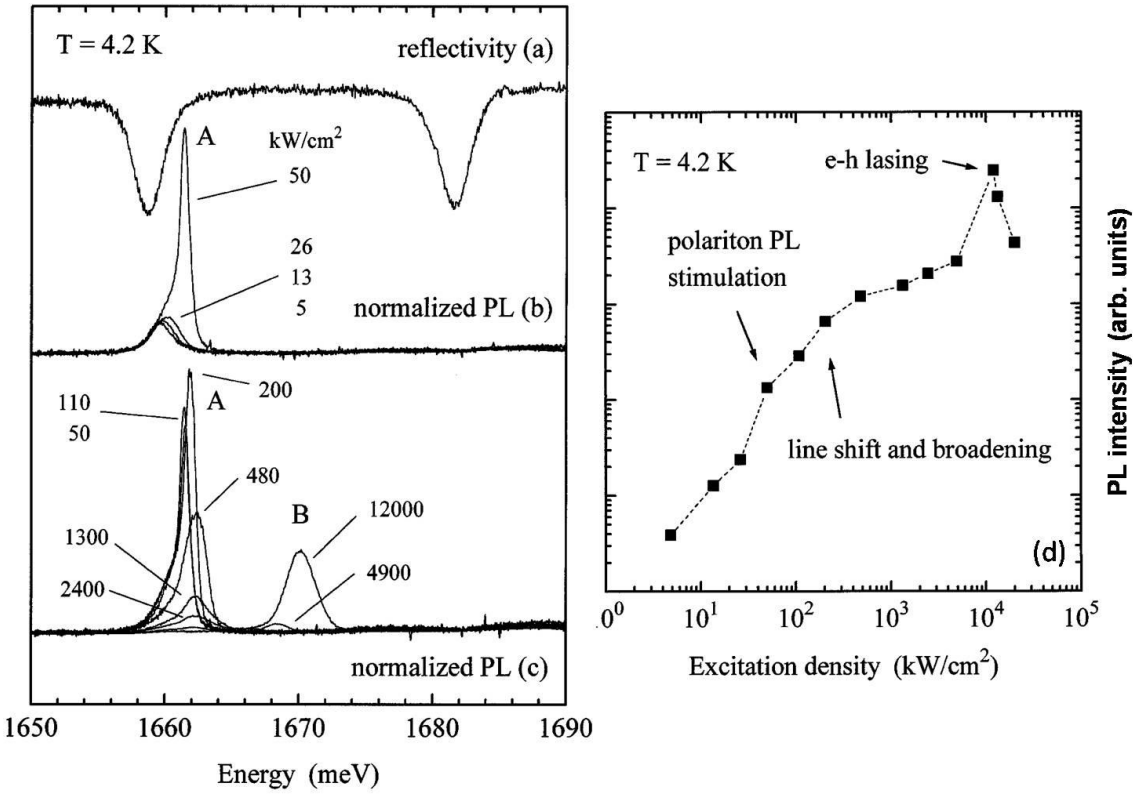

Fig. 5.4: Optical measurements at 4.2 K and for zero detuning. (a) Reflectivity spectrum. (b) PL spectra for a range of excitation densities. The excitation is at 1.8 eV. All spectra are normalized to the corresponding excitation densities. The A line is stimulated PL associated with the lower polariton state in the strong exciton-photon coupling regime. (c) Same as in (b). The B line corresponds to the stimulated emission of electron-hole plasma in the weak coupling regime. (d) Integrated PL intensity as a function of excitation density. Solid squares are experimental data. The dotted line is only a guide for the eyes. Onsets of excitation density effects as observed in (b) and (c) are indicated. These data are obtained by Le Si Dang and coworkers and reported in Ref. (8).

Further investigations (9, 10) demonstrated that the first nonlinear threshold occurs in the strong coupling regime and was due to stimulated scattering to the ground state. Concerning GaAs based samples under non resonant pumping, nonlinear emission in the strong coupling regime was claimed in a single QW GaAs microcavity with a Rabi splitting of $3.5\ \mathrm{meV}$.(11, 12) However, it was shown later that this nonlinearity presented an emission varying as the square of the excitation power, and the threshold occurred for occupation factors much smaller than one, and therefore this nonlinearity was associated with an increase of polariton-polariton scattering, rather than with final state stimulation.(12) In GaAs microcavities, in order to bypass the bottleneck and to achieve occupation factors greater than one at the bottom of the LPB under non resonant pumping, and therefore trigger the final state stimulation, it was necessary to perform pump and probe experiments.(12, 13) but in this way a spontaneous phase transition is not possible.

Indeed, in GaAs systems, the electron-hole binding energy is small ($\leq$ 10 meV) as compared to that in CdTe samples (~ 20 meV), and therefore the exciton is ionized, and polariton destroyed, at lower carrier densities.

In the literature, the BEC terminology is used in relation with polariton fluids, even if polaritons dwell in a quasi-2 dimensional plane and, strictly speaking, a true BEC can form only at temperature exactly $T = 0$ or in the presence of a trap.(14) Anyway, in the presence of interactions, superfluidity and long-range order can exist below a critical temperature (BKT transition). In Fig. 4.5 are reported the polariton phase diagrams for different materials as a function of particle density and temperature.(15)

The dashed vertical and horizontal lines mark the crossover from the strongly coupled polariton phase to the onset of LED and VCSEL operation. The solid line shows the temperature and density dependence of the BKT transition, which is the two dimensional analogous of the conventional BEC transition: the lower region corresponds to an incoherent polariton phase (polariton diode), while above this line a BEC of polaritons is found.

When the excitation density is increased, the system looses the strong coupling due to screening and exciton ionization. Actually, when non resonant excitation is above the QW bandgap, the critical carrier density for the transition from the strong- to the weak-coupling regime is even smaller than that indicated in Fig. 5.5, because in this situation polaritons coexist with free carriers which contribute to the screening. In such conditions, the strong coupling is lost at densities lower than those required for condensation and the system is driven into the VCSEL regime, where photon laser takes places in the weak coupling regime. Several attempts to overcome the relaxation bottleneck has been investigated (increase of the lattice temperature, (16) enhancing of the electron-polariton scattering (17)), but, even if the bottleneck effect can be

strongly reduced, the occupation of $k = 0$ state was always too low to trigger the stimulated scattering.

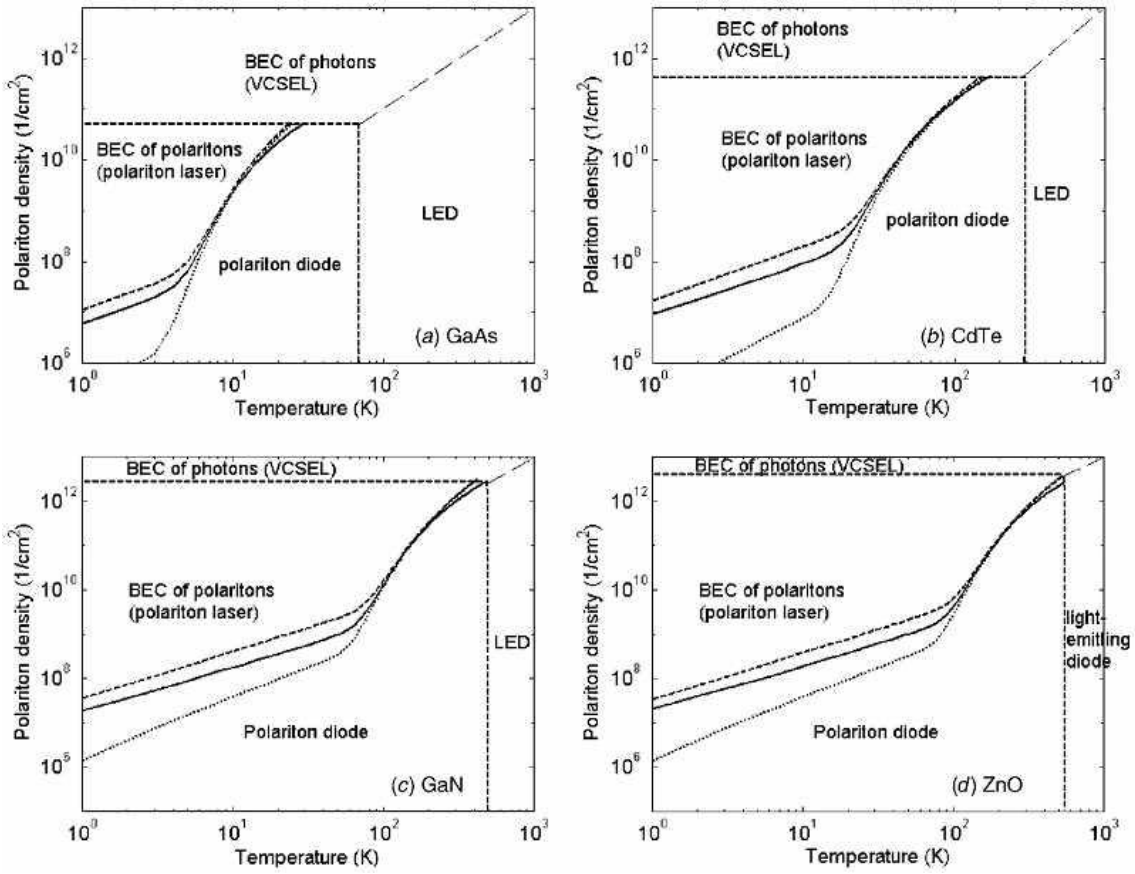

Fig. 5.5: Phase diagrams for microcavities based on (a) GaAs, (b) CdTe, (c) GaN and (d) ZnO (from Ref. (15)). The vertical and horizontal lines show the limits of the strong coupling regime imposed by the exciton thermal broadening and screening, respectively. The solid lines show the critical density for the quasi-condensation (BKT phase transition) versus temperature. The dotted and dashed lines show the critical density in finite size systems (lateral dimension of 100 µm and 1 m, respectively). Taken from Ref. (Malpuech, Semic Science Tech. 18, S395, 2003)

Only recently, BEC of polaritons has been demonstrated in GaAs systems through excitation of the LPB with a very large angle, that is, with very large in-plane momentum: in this configuration only polaritons are created in the systems, avoiding the screening effects of the free carrier bath.(18)

In systems with a larger exciton binding energy, under non resonant excitations, the transition to the weak coupling occurs at much higher densities, (see Fig. 5.5) and the condensed phase can be reached in the strong coupling regime,(19) even at room temperature in the case of GaN based microcavities.(20)

5.3 – Transition from the strong to the weak coupling regime

When the carrier density is increased, by raising the optical excitation power, the exciton oscillator strength, f_{exc}^{osc}, is renormalized due to the formation of an electron-hole (e-h) plasma. As a result, the coupling parameter is reduced (see Eq. 2.4 and 2.15) and a continuous transition from the strong- to the weak-coupling regime occurs: for increasing excitation intensities, the reduction in the exciton-photon coupling manifests itself in a decreased Rabi splitting, i.e. a blue shift of the LPB emission energy and a red shift of the UPB emission energy.(4, 21-23) When the WC regime is reached, photon stimulated emission takes place.

In this chapter, we will study the transition from the strong to the weak coupling regime. The employed sample is a 3/2 λ GaAs microcavity with two stacks of three $In_{0.06}Ga_{0.94}As$ QWs, with a Rabi splitting of $6\ meV$ at 5 K. Electron-hole pairs are non-resonantly excited by 2 ps-long circularly-polarized (σ^+) pulses of a $Ti{:}\,Al_2O_3$ laser, with energy $E = 1.63\ eV$ and repetition rate of $80\ Mhz$. Polaritons with large wavevector $k_{\|}$ are formed and relax towards the bottom of the LPB. Photoluminescence (PL) from states with $k_{\|} \sim 0$ is selected by a diaphragm and analyzed into its co- (σ^+) and cross- (σ^-) polarized components by a combination of a $\lambda/4$ plate and a linear polarizer. The PL is energy- and time- resolved by a spectrograph coupled with a streak camera (resolution of $0.2\ meV$ and $10\ ps$, respectively). All the experiments are carried out at $\delta = 0$ and $T = 5\ K$.

In Fig. 5.6, streak camera images of the microcavity emission after pulsed non-resonant excitation above the first minimum of the stop band are shown for different intensities of the pump pulses: the emission from the $k{\sim}0$ states is time- (vertical direction) and energy-resolved (horizontal direction). At low intensities, the microcavity is in the strong coupling regime, with emission energies of the LPB (E_{LPB} in the figure) and UPB (E_{UPB}, indicated in the figure but not visible in this color scale due to the much weaker intensity of the UPB emission) shifted with respect to the degenerate exciton and photon resonance (E_{CM}) and separated by the Rabi splitting. Increasing the excitation density, the emission energy shows a blue shift at short times, corresponding to a high density phase of polaritons, and at longer times the low-density value of the LPB energy is recovered. The transition of the emission energy towards the cavity mode resonance is therefore related with the density of polaritons at different times. In this intermediate regime, an increase of the photoluminescence linewidth and an acceleration of the dynamics are clearly visible. Increasing further the excitation power (above the power threshold $P_{th} = 1\ mW$) induces a collapse of the system into the weak coupling regime.

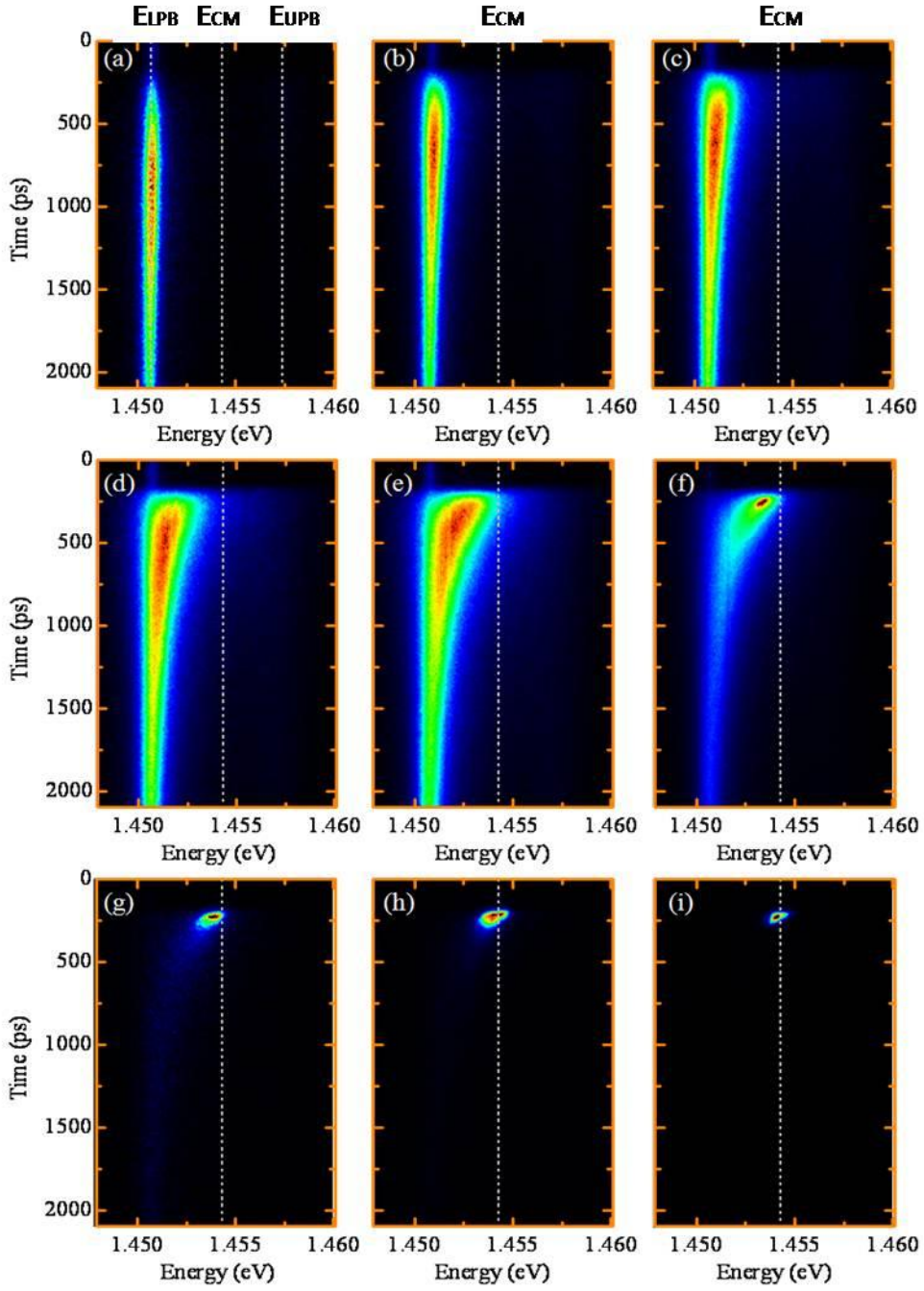

Fig. 5.6: Microcavity luminescence at k = 0 at 5 K after pulsed non-resonant excitation above the first minimum of the stop band at different excitation powers P (normalized to the threshold power P_{th} for the transition to the weak coupling regime): (a) P/P_{th}=0.03 (b) P/P_{th}=0.2, (c) 0.3, (d) 0.5, (e) 0.66, (f) 0.83, (g) 1, (h) 1.15, (i) 1.5. The dotted lines in (a) depict the energies of the $k = 0$ states of the LPB, cavity mode (E_{CM}) and UPB.

Above P_{th}, the emission energy shifts at the cavity mode resonance, with a superlinear dependence of the photoluminescence intensity on the excitation power and a very fast dynamics, which concentrates in the first 50 ps, due to the stimulated character of the recombination in the weak-coupling regime. It is interesting to note that at short times, when the peak of the emission energy is shifted, a weaker emission

is still visible (in panel (d), (e) and (f)) at the not-shifted LPB energy: in other words, for excitation powers in the range of the transition from the strong- to the weak-coupling regime, a strong coupled emission coexists with a decoupled component.

This phenomenon can be observed in experiments at very different detunings. Fig. 5.7 shows the emission energy as a function of the incident power for different detunings of the bare exciton and cavity mode.

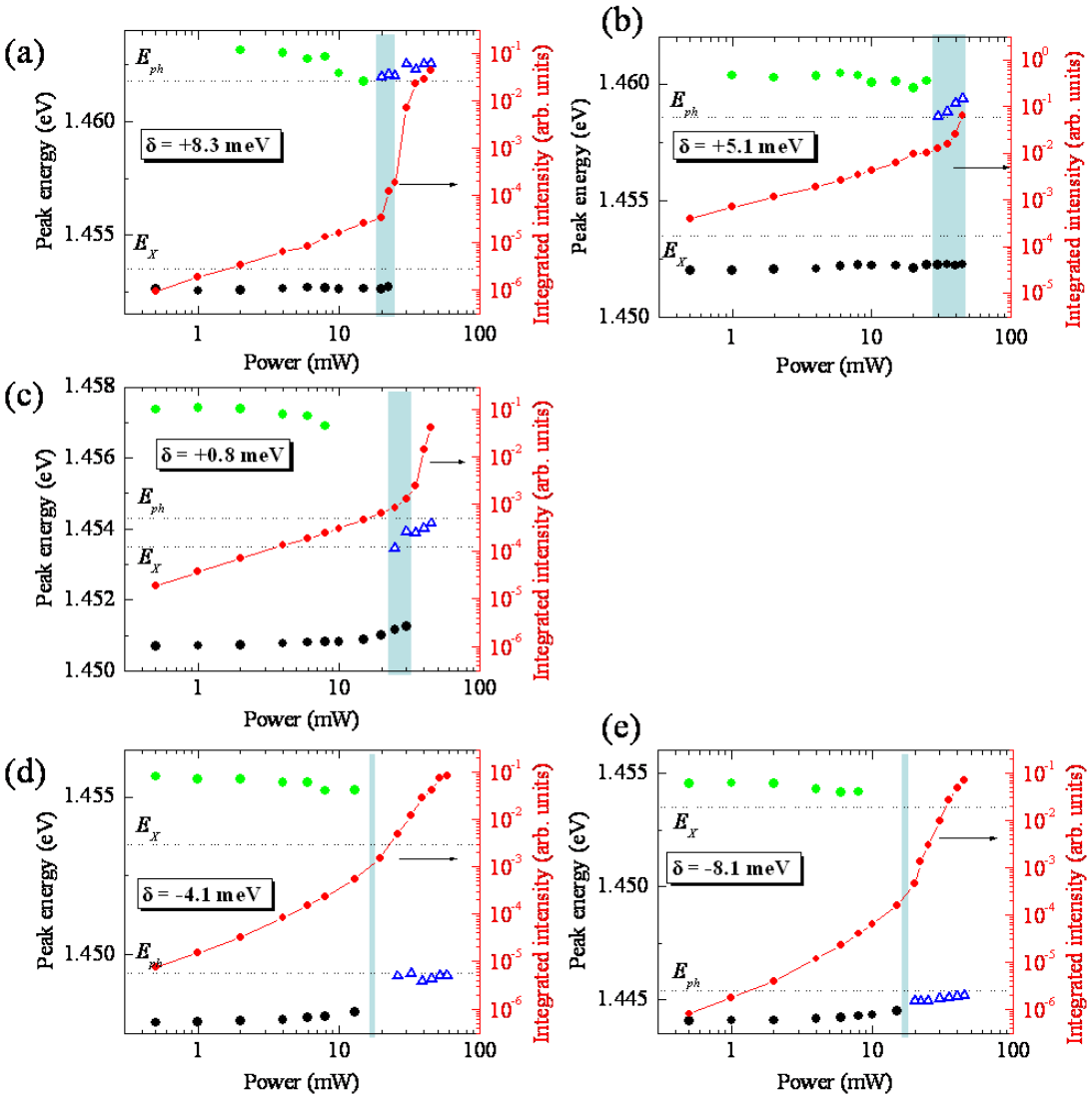

Fig. 5.7: On the left scale is depicted the energy of the k = 0 emission of the UPB (green dots), LPB (black dots) and cavity modes (blue open triangles) as a function of the non-resonant pulse power for several values of the detuning: (a) δ = 8.3 meV, (b) δ = 5.1 meV, (c) δ = 0.8 meV, (d) δ = -4.1 meV, (e) δ = -8.1 meV. On the right scale is reported the total integrated emission (red dots). The blue area shows the transition from the strong to the weak coupling regimes. The dotted lines indicate the energy of the bare cavity (E_{ph})and exciton (E_x) modes.

At every detuning, at low excitation power, the system is in the strong coupling regime and the emission intensity shows a linear dependence on the excitation power. The light blue areas indicate the range of powers for the transition regions, where the appearance of emission at the cavity mode energy coexists with a weaker emission at the energies of the strongly-coupled polariton dispersions; the cavity mode emission intensity presents a superlinear dependence on the excitation power, characteristic of lasing systems at the threshold power.(24) For this reason, the coexistence can be observed in a small range of powers, since the photon lasing mode intensity increases superlinearly and hides the emission of the coupled mode, whose intensity increases only linearly with the excitation power. The $\delta \sim 0$ configuration presents the most favorable condition for the observation of the coexistence, as the strongly and weakly coupled modes present in this case the maximum separation in energy between them.

One could think that the Gaussian profile of the laser beam could explain this coexistence: the weakly coupled emission coming from the center of the spot, where the critical density for the transition is reached firstly, while at the borders of the spot polaritons would be still in the strong coupling regime. However, we shall see in section 5.3.2, where the spatial properties of the emission are presented, that it is not the case.

In the next section, we are going to discuss the importance of the polarization properties of polaritons in the transition from the strong to the weak coupling regime, and in particular we will study the coexistence of strongly and weakly coupled polaritons with opposite spins.

5.3.1 - Transition from the strong- to the weak-coupling regime in semiconductor microcavities: polarization dependence

Two processes are responsible for the change of f_{ex}^{osc} at high carrier density: the blocking mechanism due to the Pauli exclusion principle (phase space filling) and the modification of the electron-hole interaction in the presence of other electron-hole pairs.(25) Both, the exchange effect, another consequence of the exclusion principle, and the long-range Coulomb interaction contribute to the latter process. These effects have been profusely studied and it is well known how they affect the exciton properties and in particular the exciton oscillator strength f_{exc}^{osc}.(26) However, only few works deal with polarized interacting exciton in QWs.(27, 28) In order to understand and control the emission properties of a polariton laser, it is important to study the role of the spin in the polariton interactions.(29, 30) In this section, we will see that the transition from the strong coupling to the weak coupling regime takes

place at different powers for polaritons with opposite spin orientation and that it is governed by the occupation factor of each spin population.

Fig. 5.8(a) and (b) illustrate the streak camera images of the LPB emission with polarization σ^+ and σ^-, respectively, for an excitation power $P_{ex} = 0.8\,mW$. In Fig. 5.8(a), the σ^+-LPB emission energy is blue shifted at short times (as indicated by the arrow), when a high carrier density is present. At longer time, as the carrier density decreases, the shift of the σ^+-LPB emission energy vanishes. The σ^--LPB emission (Fig. 5.8(b)) presents the same behavior as that described for the σ^+ case, but the energy shift at short time is smaller, as evidenced by the arrow, which marks the short-time energies of the σ^+ emission. It should be stated that the false-color intensity scales of Fig. 5.8(a) and Fig. 5.8(b) are different. Actually the σ^+ signal is much stronger than the σ^- one, yielding a time-integrated polarization degree $\wp_{circ} = 0.5$, where $\wp_{circ}$ is defined as in Eq. 3.2. In Fig. 5.9 is plotted the time evolution of the emission intensity for both polarizations and the corresponding polarization degree $\wp_{circ}$.

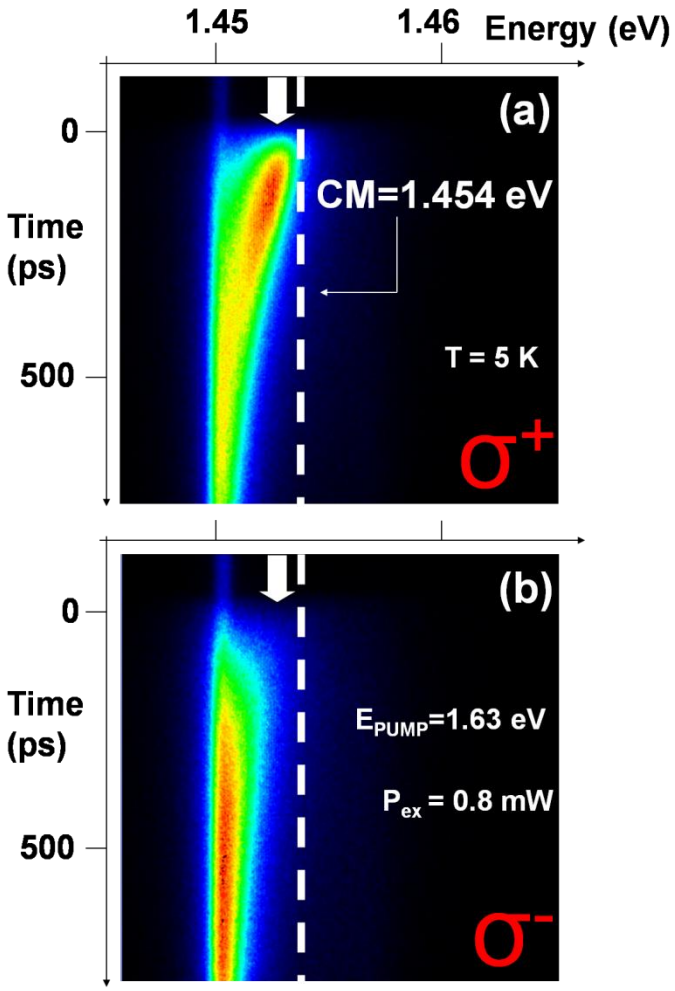

Fig. 5.8: LPB emission with polarization σ^+ (a) and σ^- (b) for an excitation power P_{ex}=0.8 mW. The dashed lines represent the energy on the cavity mode, CM = 1.454 eV. The white arrows indicate the energy of the blue shifted σ^+ emission at short times.

The dependence on P_{ex} of the LPB peak energies at short time (31) is presented in Fig. 5.10(a) for the two polarizations. Under low excitation power, the system is in the strong coupling regime and the LPB, for both polarizations, lies at an energy $\sim 3.5\ meV$ below the bare cavity mode (CM). Increasing P_{ex}, both polarized branches of the lower polariton dispersion experiment a blue shift: the Rabi splitting, given by twice the energy separation between the cavity mode and the LPB, is effectively reduced due to the afore-mentioned decrease of f_{ex}^{osc}. Strikingly, at a given P_{ex}, the energy shift of the σ^+ polaritons is larger than that of the σ^- polaritons and an energy splitting between them is obtained.

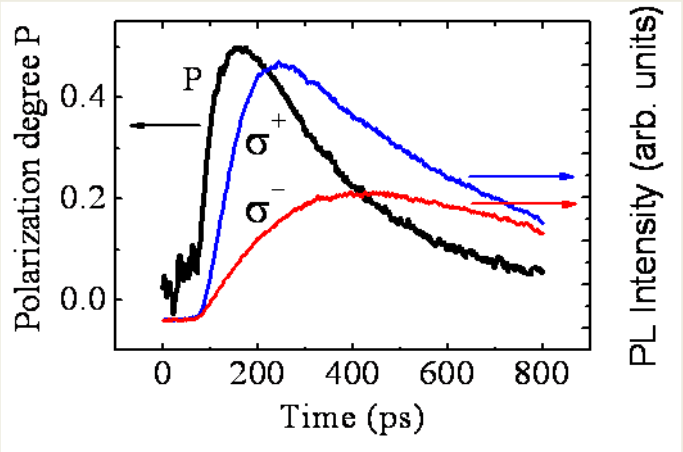

Fig. 5.9: Emission intensity of both polarizations plotted as a function of time (right scale). The corresponding polarization degree $\wp_{circ}$ is shown on the left scale (black curve).

Eventually, for $P > 1$ mW, σ^+ polaritons (spin up, +1) reach the energy of the cavity mode and are in the weak coupling regime, while σ^- polaritons (spin down, -1) are still in the strong coupling regime, as can be inferred by their energy positions (see Fig. 5.10(a)). A transition from the strong coupling regime to the weak coupling regime has taken place only for the co-polarized polaritons.

Fig. 5.10(b) shows the dependence on P_{ex} of the time-integrated PL intensity for both polarizations and the corresponding polarization degree. At low P_{ex}, the PL intensity is similar for both polarizations, yielding $\wp_{circ} \approx 0$. At powers higher than ~ 0.6 mW, when the transition from the strong coupling to the weak coupling regime starts, the intensity of σ^+ polaritons grows superlinearly with P_{ex} and the polarization degree increases rapidly reaching $\wp_{circ} \approx 0.95$ at $1.2\ mW$. At this power, the σ^+ emission corresponds to laser action from the bare cavity mode in the weak coupling regime.(23, 32)

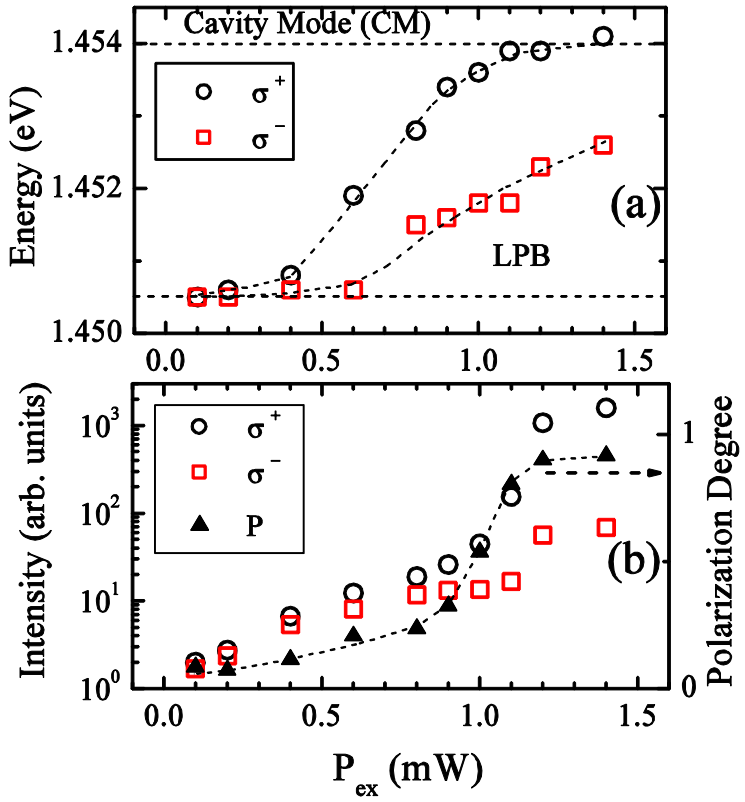

Fig. 5.10: (a) Emission energy for both polarizations as a function of the excitation power. The dashed lines represent the energies of the LPB and cavity mode at k = 0. (b) Time-integrated PL intensity for both polarizations and the corresponding polarization degree.

To have a deeper understanding of the energy shifts for both polarizations, we analyze their dependence on the occupation factors of each of the polariton populations with a given spin. Indeed, with a direct measurement of the absolute PL intensity , it is possible to obtain the occupation factors $\eta_{occ}^{\sigma^+}$ and $\eta_{occ}^{\sigma^-}$ of polariton states with $k_{\|}\sim 0$. We relate the number of polaritons $N(k_{\|}\sim 0)$ to the PL intensity I_{PL} (in Watt) by:

$$N(k_{\|}\sim 0) = \frac{I_{PL} \times \tau}{\propto \times E}, \qquad 5$$

where $\tau = 2\,ps$ is the cavity photon escape time, α is the polariton photon weight at $k_{\|}\sim 0$ and E is its energy. Selecting $k_{\|}\sim 0$ states by a pin-hole, a finite number, N_k, of k-states contribute to the PL: the occupation factor is given by $\eta_{occ} = \frac{N(k_{\|}\sim 0)}{N_k}$.(33, 34) Fig. 5.11(a) shows the occupation factors for both spin populations, $\eta_{occ}^{\sigma^+}$ and $\eta_{occ}^{\sigma^-}$, versus the excitation power P_{ex}.

This analysis makes now clear that the difference in the energy shifts for both polarizations is directly linked to their respective occupation factors: the energy

splitting between σ^+ and σ^- emissions appears at $P_{ex} \geq 0.6\,mW$ (Fig. 5.10(a)), the same power for which a noticeable difference in the occupation factors is obtained (Fig. 5.11(a)). Since in the weak coupling regime the emission behaves as that from photons in a VCSEL, we restrict our analysis for σ^+ polarization to polariton occupation factors corresponding to values of P_{ex} at which the polaritons are still in the strong coupling regime ($P_{ex} < 1.1\,mW$).

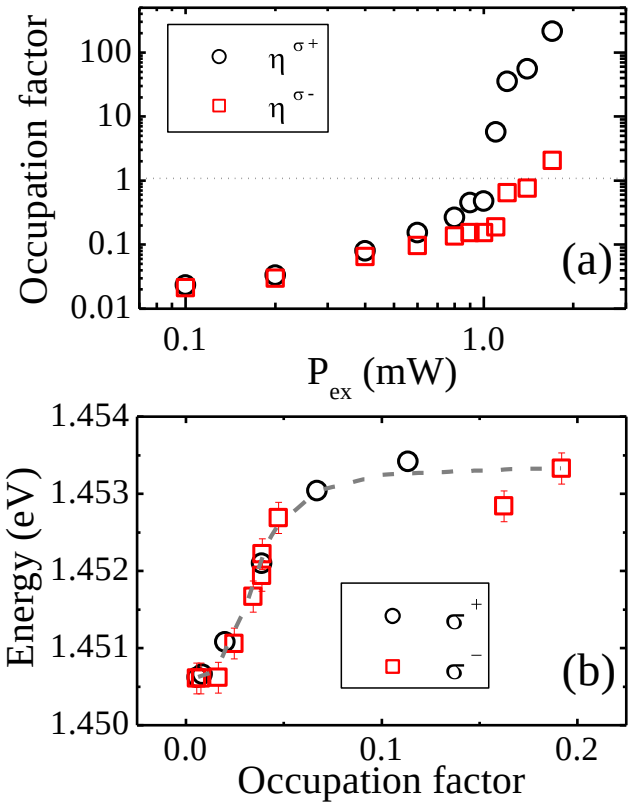

Fig. 5.11: (a) Occupation factors for both σ^+ and σ^- populations versus the excitation power. (b) LPB-peak energies of both polarizations versus the respective occupation factors.

Plotting now the σ^+ and σ^- LPB-peak energies versus the respective occupation factors, as in Fig. 5.11(b), the same behavior is observed for both polarizations, with the two curves superimposed. The emission energies of the polarized polaritons, and consequently their coupling regime, are determined by the occupation factor of the polaritons with a given spin. It is quite remarkable that the combined effect of the total carrier density and of the spin orientation of the polaritons on the screening of the exciton (i.e. on the collapse of the Rabi splitting) yields an identical dependence on the occupation factors.

In fact, it has been noted that phase space filling plays a dominant role in determining the exciton properties in the presence of high carrier densities: the wavefunction of a bound electron-hole pair can be represented as a linear combination of the eigenfunctions of all free-electron states; if the states with small $k_{\|}^{e,h}$ are occupied by free carriers and subject to the Pauli exclusion principle, the allowed electron/hole states that contribute to the exciton wavefunction are those with large momentum $k_{\|}^{e,h}$ and the shape of the exciton wavefunction is strongly modified. Bigenwald *et al.* (35) have shown that in this case the binding energy and the oscillator strength of the exciton depend on the distribution rather than on the total density of electrons and holes.

One could argue that the different distributions of carriers with opposite spin, together with the fact that e-h interactions include exchange, which depends strongly on spin, may explain why the f_{exc}^{osc} of majority σ^+ spin excitons becomes smaller than that of minority σ^- spin excitons at a given carrier density (i.e., excitation power) and that the transition from the strong coupling to the weak coupling regime for polaritons with a given spin orientation is mainly determined by its own occupation factor. It should be mentioned that the splitting between polarized exciton(27) can be ruled out as the origin of the results presented in Fig. 5.10(a): in fact, the splitting is absent for the LPB at large positive detunings, where LPB is mostly excitonic, and it is also absent in an identical sample without cavity mirrors.

In order to exclude possible spatial inhomogeneities present in these samples, (19, 36, 37) which could lead to spatially separated regions containing different populations of σ^+ and σ^- polaritons, we have performed confocal scanning of the polariton emission with a resolution of $10\ \mu m$ (see next section). In a region of $50\ \mu\mathrm{m}$ close to the laser spot center we have observed coexistence of both the weakly coupled σ^+ emission together with the strongly coupled σ^- polaritons.

5.3.2 Spatial distribution of strong- and weak-coupled exciton polaritons in semiconductor microcavities

We have already seen that in a microcavity, increasing the polariton density, the coupling is reduced due to phase space filling effects and the screening of the Coulomb interaction between the fermions (electrons and holes) that compose the excitons. Consequently, the LPB energy shifts towards the cavity mode energy: the strong coupling is lost and polaritons convert in the bare exciton and photon modes (weak-coupling regime). Eventually, for very high powers, the excitons also ionize and a plasma of oppositely charged particles in the presence of the electromagnetic radiation in the cavity is obtained. Only if a sufficiently high density of polaritons, without losing the strong coupling regime, is achieved (occupation factors larger than 1), a polariton condensate can be created. Otherwise, with the increase of the excitation intensity the system undergoes a transition from the strong- to the weak-coupling regime. In the previous section has been demonstrated that under non resonant circularly polarized excitation the transition from the strong coupling to the weak coupling regime of the co-polarized polaritons occurs at an excitation power lower than that of the cross-polarized polaritons. This is attributed to the different carriers distributions for each spin orientation and to phase space filling effects, which obtain a transition that depends only on the polariton population of a given spin. The strength of the coupling was determined from the LPB emission energies for the two spin population as a function of the excitation power.

In this section the spatial distribution of this transition is studied by a confocal scanning of the LPB emission across the laser excited area, with a resolution of 10 µm.

The image of the sample is magnified 2.5 times and a pin-hole with a diameter of 25 µm is used in the plane of the image to select only a small part of the excited area. In this way we can compare PL coming from different point of the excited spot with a final resolution of 10 µm.

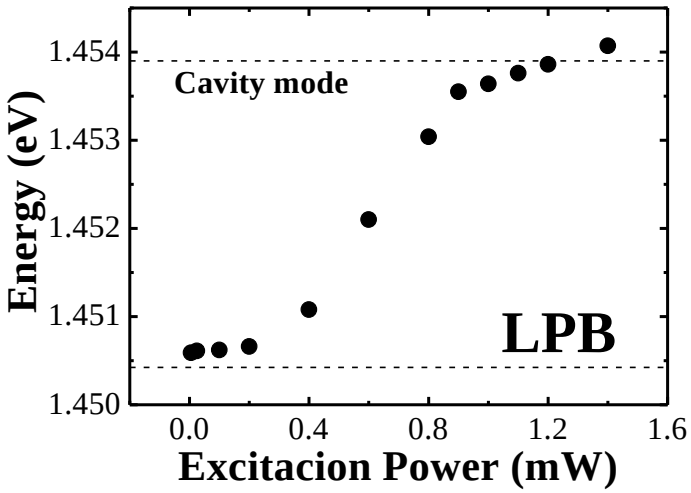

Fig. 5.12: Emission energy of the LPB at resonance and $k = 0$ as a function of the excitation power.

At low P the system is in the strong coupling regime and the LPB emits at 1.4505 eV; with increasing P, the LPB emission blue shifts as depicted in Fig. 5.12. At P > 1 mW the system is in the weak-coupling regime and the PL is due to bare cavity photons. The PL intensity increases linearly with the excitation power for P < 0.6mW and superlinearly at higher P, due to the increasing importance of the stimulated polariton-polariton scattering,(38) until a saturation is obtained in the weak-coupling regime.

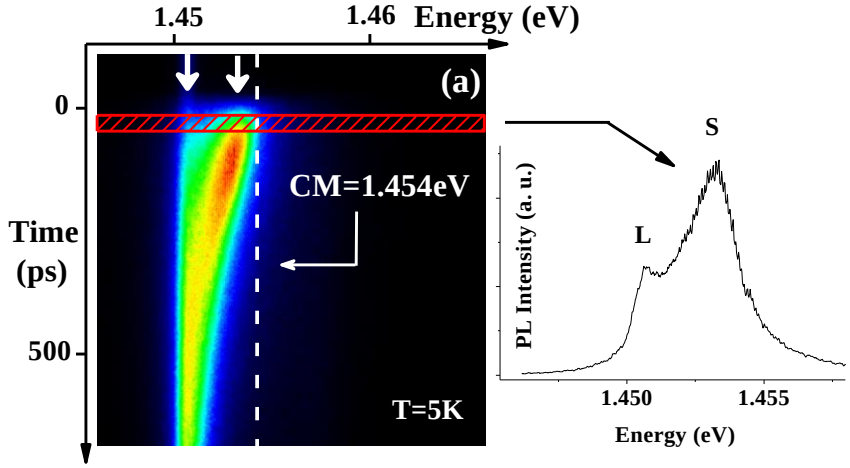

Fig. 5.13: Streak camera image of PL emission with P = 0.8 mW. The cavity mode (CM) is indicated by the dashed line; the white arrows indicate the two coexisting emission S and L. The inset depicts the energy spectrum at 70 ps.

In Fig. 5.13 is shown the streak camera image of the LPB emission at k = 0 for P_{ex} = 0.8 mW. The LPB is shifted towards the cavity mode (CM) at short time, when the high density of carriers reduces the strong coupling and the PL intensity is superlinear with P_{ex}. At longer times, when the polariton density becomes smaller, the LPB emits at 1.4505 eV and recovers its linear emission regime.

The inset of Fig. 5.13 shows the energy spectrum of the PL at short time (70 ps): the blue-shifted LPB emission (S) coexists at short time with a non-shifted LPB emission (L) peaked at 1.4505 eV. The S peak is due to PL coming from a region with a high density of polaritons, (the emission energy corresponds to a renormalized Ω and the PL intensity is superlinear with P), while the L peak is due to a region with a low density of polaritons in the linear emission regime. These regions are coexisting in the excitation spot.

The coexistence of linear- and non linear-regime emissions has been attributed in the literature to different intensities in the excitation as a consequence of the Gaussian profile of the laser spot(32). According to this explanation, the S emission would originate at the center of the spot, where a high density of polaritons is present, and the L emission at the border of the spot.

To check whether the coexistence of the linear-and non linear-regime emissions at short times is due to the Gaussian profile of the laser beam (diameter = 200 μm), we have scanned the emission spot with a resolution of 10 μm to discriminate the PL coming from different positions of the excited area.

Fig. 5.14 shows the spectra obtained with the pin-hole placed at the center, 50 μm and 100 μm apart from the center of the laser spot, respectively. If the coexistence were originated from a high polariton density at the center and a lower density at the border of the spot, it would be expected an S-emission from the center and a L-emission from the border, where the intensity doesn't reach the non-linear threshold. However, we detect both components all over the excitation spot with a resolution of 10 μm.

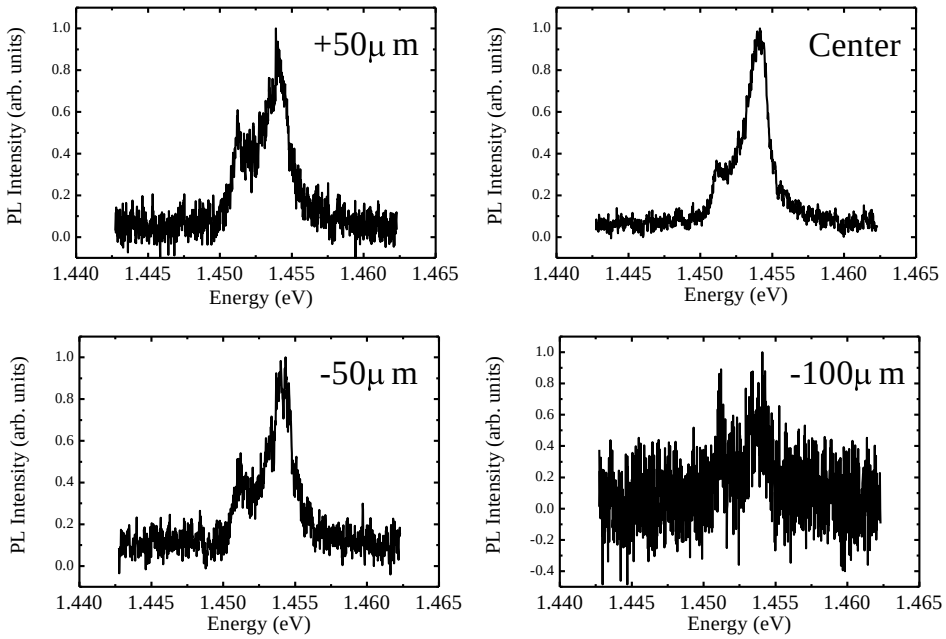

Fig. 5.14: PL spectra after 70 ps observed with the pin-hole placed at the center (b), 50 μm (a and c) and 100 μm (d) apart from the center.

Moreover, the separation in energy between the peaks remains constant over the whole emission area, ruling out the spatial variation of intensity of the excitation spot as the origin of the coexistence of the S- and the L-emission, which should yield a decreasing splitting moving from the center towards the edges of the spot. We interpret our observations in terms of an existence of islands with different polariton densities that are located all over the excitation area. Point defects in the cavity can produce a spatially non-uniform potential, allowing polaritons to populate preferentially some positions inside the excited area.(36) Similar regions have been identified as polariton condensates in recent experiments.(19)

In order to get more insight on the island distribution we investigate the intensity distribution of the emission across the excitation spot. Fig. 5.15 shows the intensities of the S- and L-emissions as a function of the position inside the spot. The ratio between the S- and L-peak intensities is well described by a Gaussian centered at the middle of the excitation spot, as compiled in Fig. 5.16.

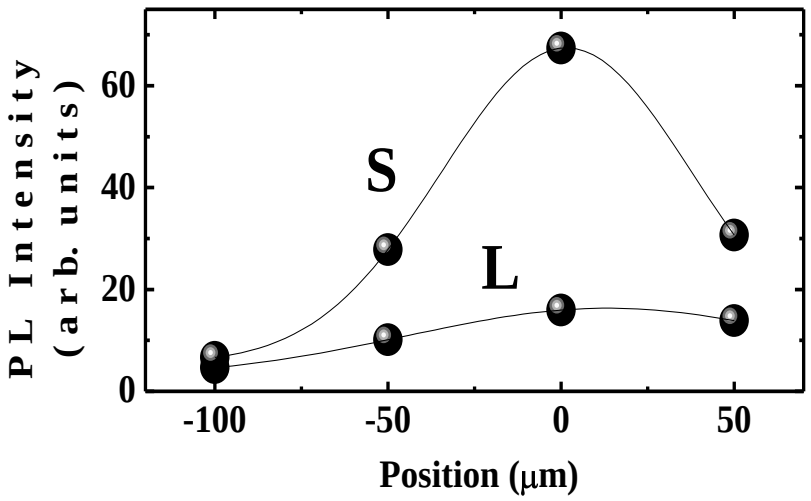

Fig. 5.15: PL intensity of the S- and L-emission versus the position.

It has to be noted that if the S-emission were originated at the center and L emission at the borders of the spot, one should expect that the ratio would be superlinear on the excitation intensity, due to stimulated scattering process occurring where a large excitation is present, and therefore not yielding a Gaussian profile. Actually, S-signals originate from separate islands smaller than our spatial resolution, coexisting with low-density regions in the linear emission regime, and the number of islands giving rise to the S-emission follows a Gaussian distribution along the spot.

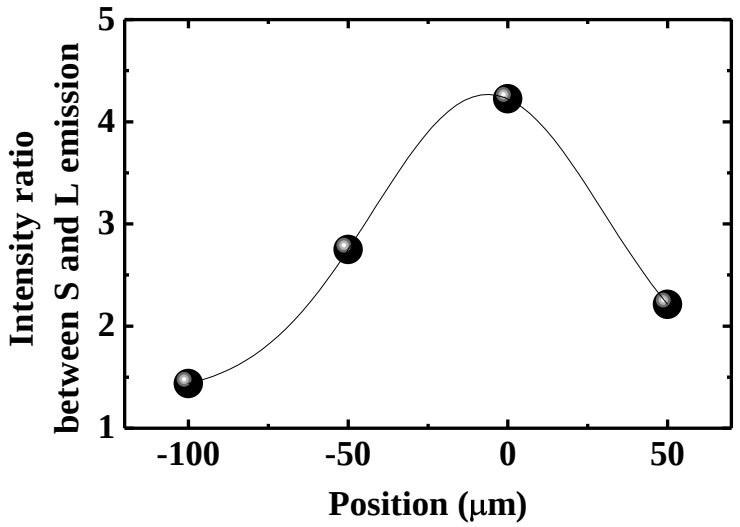

Fig. 5.16: Intensity ratio between S- and L-peak versus the position, fitted by a Gaussian centered at the middle of the spot.

In summary, S-emission, corresponding to high densities of polaritons, originates in islands non-uniformly distributed all over the sample, and the Gaussian profile of the laser beam only determines the probability to reach the critical density of polaritons in such islands. Furthermore, strong- and weak-coupled polaritons coexist in the area illuminated by the excitation laser within regions smaller than 10 μm.

5.4 – Summary

In this Chapter we have presented experimental results on the time-resolved PL in GaAs microcavities, at $\delta = 0$, under non-resonant circular polarized excitation. With increasing the excitation intensity, the exciton-exciton interactions lead to a renormalization of the polariton energies and eventually to a transition to the weak-coupling regime. The polarization analysis of the emission showed that the transition occurs for different intensities of the excitation beam. The emission energies of the polarized polaritons, and consequently their coupling regime, are determined by the occupation factor of the polaritons with a given spin. This is attributed to the different carriers distributions for each spin orientation and to phase space filling effects.

The spatial distribution of the strong- to weak-coupling transition is studied by a confocal scanning of the LPB emission across the laser-excited area. It has been found that high density phases of polaritons originate in islands non-uniformly distributed, and that strong- and weak-coupled polaritons coexist within regions smaller than 10 μm.

Bibliography:

1. Rota, L., Lugli, P., Elsaesser, T. & Shah, J. (1993) *Phys. Rev. B* **47,** 4226.

2. Pau, S., Cao, H., Jacobson, J. M., Björk, G., Yamamoto, Y. & Imamoglu, A. (1996) *Phys. Rev. A* **54,** 1789-1792.

3. Cao, H., Pau, S., Jacobson, J. M., Björk, G., Yamamoto, Y. & Imamoglu, A. (1997) *Phys. Rev. A* **55,** 4632-4635.

4. Butté, R., Delalleau, G., Tartakovskii, A. I., Skolnick, M. S., Astratov, V. N., Baumberg, J. J., Malpuech, G., Di Carlo, A., Kavokin, A. V. & Roberts, J. S. (2002) *Phys. Rev. B* **65,** 205310 - 205319.

5. Lagoudakis, P. G., Martín, M. D., Baumberg, J. J., Malpuech, G. & Kavokin, A. (2004) *Journal of Appl. Phys.* **95,** 2487-9.

6. Imamoglu, A., Ram, R. J., Pau, S. & Yamamoto, Y. (1996) *Phys. Rev. A* **53,** 4250.

7. Dang, L. S., Heger, D., Andre, R., Boeuf, F. & Romestain, R. (1998) *Phys. Rev. Lett.* **81,** 3920-3923.

8. Dang, L. S., Heger, D., André, R., Boeuf, F. & Romestain, R. (1998) *Phys. Rev. Lett.* **81,** 3920-3923.

9. Boeuf, F., André, R., Romestain, R., Dang, L. S., Péronne, E., Lampin, J. F., Hulin, D. & Alexandrou, A. (2000) *Phys. Rev. B* **62,** R2279-R2282.

10. Alexandrou, A., Bianchi, G., Péronne, E., B. Hallé, F. Boeuf, André, R., Romestain, R. & Dang, L. S. (2001) *Phys. Rev. B* **64,** 233318.

11. Senellart, P. & Bloch, J. (1999) *Phys. Rev. Lett.* **82,** 1233-1236.

12. Senellart, P., Bloch, J., Sernage, B. & Marzin, J. Y. (2000) *Phys. Rev. B* **62,** R16263-6.

13. Huang, R., Tassone, F. & Yamamoto, Y. (2000) *Phys. Rev. B* **61,** R7854.

14. Balili, R., Hartwell, V., Snoke, D., Pfeiffer, L. & West, K. (2007) *Science* **316,** 1007.

15. Malpuech, G., Rubo, Y. G., Laussy, F. P., Bigenwald, P. & Kavokin, A. V. (2003) *Semicond. Sci. Technol.* **18,** S395.

16. Tartakovskii, A. I., Emam-Ismail, M., Stevenson, R. M., Skolnick, M. S., Astratov, V. N., Whittaker, D. M., Baumberg, J. J. & Roberts, J. S. (2000) *Physical Review B* **62,** R2283.

17. Bajoni, D., Perrin, M., Senellart, P., Lemaitre, A., Sermage, B. & Bloch, J. (2006) *Phys. Rev. B* **73,** 205344-8.

18. Lai, C. W., Kim, N. Y., Utsunomiya, S., Roumpos, G., Deng, H., Fraser, M. D., Byrnes, C., Recher, P., Kumada, N., Fujisawa, T. & Yamamoto, Y. (2007) *Nature* **450,** 529.

19. Kasprzak, J., Richard, M., Kundermann, S., Baas, A., Jeambrun, P., Keeling, J. M. J., Marchetti, F. M., Szymanska, M. H., André, R., Staehli, J. L., Savona, V., Littlewood, P. B., Deveaud, B. & Dang, L. S. (2006) *Nature* **443,** 409-14.

20. Christopoulos, S., Baldassarri_Hoger_von_Hogersthal, G., A.J.D.Grundy, Lagoudakis, P. G., Kavokin, A. V., Baumberg, J. J., Christmann, G., Butte, R., Feltin, E., Carlin, J. F. & Grandjean, N. (2007) *Phys. Rev.Lett.* **98,** 126405.

21. Houdré, R., Gibernon, J. L., Pellandini, P., Stanley, R. P., Oesterle, U., Weisbuch, C., Shelykh, I. A., O'Gorman, J., Roycroft, B. & Ilegems, M. (1995) *Phys. Rev. B* **52,** 7810-7813.

22. Bloch, J., Sermage, B., Jacquot, C., Senellart, P. & Thierry-Mieg, V. (2002) *Physica E* **13,** 390-393.

23. Kira, M., Jahnke, F. & Koch, S. W. (1997) *Phys. Rev. Lett.* **79,** 5170-73.

24. Doan, T. D., Cao, H. T., Tran Thoai, D. B. & Haug, H. (2005) *Phys. Rev. B* **72,** 085301.

25. Schmitt-Rink, S., Chemla, D. S. & Miller, D. A. B. (1985) *Phys. Rev. B* **32,** 6601-6609.

26. Haug, H. & Schmitt-Rink, S. (1984) *Prog. Quant. Electr.* **9,** 3-100.

27. Viña, L., Muñoz, L., Pérez, E., Fernández-Rossier, J., Tejedor, C. & Ploog, K. (1996) in *Phys. Rev. B*, Vol. 54, pp. 8317.

28. Ben-Tabou de-Leon, S. & Laikhtman, B. (2001) *Phys. Rev. B* **63,** 125306.

29. Tartakovskii, A. I., Kulakovskii, V. D. & Krizhanovskii, D. N. (1999) *Phys. Rev. B* **60,** R11293-R11296.

30. Quochi, F., Staehli, J. L., Oesterle, U., Deveaud, B., Bongiovanni, G., Mura, A. & Saba, M. (1999) *24th Int. Conf. Phys. Semiconduct., Ed. D. Gershoni (World Scientific, Singapore), CDROM 0565.pdf, IV-G-2*.

31. *The peak energies are obtained from time-integration in a window [0, 150] ps*.

32. Deng, H., Weihs, W., Snoke, D., Bloch, J. & Yamamoto, Y. (2003) *Proc. Natl. Acad. Sci. U.S.A.* **100,** 15318-23.

33. Stevenson, R. M., Astratov, V. N., Skolnick, M. S., Whittaker, D. M., Emam-Ismail, M., Tartakovskii, A. I., Savvidis, P. G., Baumberg, J. J. & Roberts, J. S. (2000) *Phys. Rev. Lett.* **85,** 3680-3683.

34. Senellart, P., Bloch, J., Sermage, B. & Marzin, J. Y. (2000) *Phys. Rev. B* **62,** R16263-R16266.

35. Bigenwald, P., Kavokin, A., Gil, B. & Lefebvre, P. (2000) *Phys. Rev. B* **61,** 15621-24.

36. Sanvitto, D., Krizhanovskii, D. N., Whittaker, D. M., Ceccarelli, S., Skolnick, M. S. & Roberts, J. S. (2006) *Phys. Rev. B* **73,** 241308-4.

37. Krizhanovskii, D. N., Sanvitto, D., Love, A. P. D., Skolnick, M. S., Whittaker, D. M. & Roberts, J. S. (2006) *Phys. Rev. Lett.* **97,** 097402.

38. Klopotowski, L., Amo, A., Martin, M. D., Viña, L. & André, R. (2005) *phys. stat. sol. (a)* **202,** 357-361.

Chapter 6

High-density polariton system under resonant excitation

6.1 – OPO and OPA

The collective behavior of microcavity polaritons under resonant excitation of the lower polariton branch has been the subject of intense study in the last ten years. Experimentally, it has been demonstrated that very large optical nonlinearities can be obtained in resonantly pumped microcavities in the strong coupling regime.(1, 2) When polaritons are resonantly injected into the lower branch, it is possible to create a large population with a desired energy and momentum. An important property of planar microcavities is the correspondence between the in-plane momentum of each polariton mode and the direction of the external photon to which it couples.(3) Moreover, it means that angular-resolved PL experiments allow investigating the polariton distribution by analyzing the angular dependence of the emission outside the microcavity. Indeed, in the far field plane, each point with coordinates $(\vartheta_x, \vartheta_y)$ corresponds to a particular in-plane momentum $(k_x, k_y) = \frac{\omega}{c}(\sin\vartheta_x, \sin\vartheta_y)$, where ω is the emission frequency.

Polaritons with energy and in-plane momentum $(\varepsilon_{LP}(\boldsymbol{k_P}), \boldsymbol{k_P})$ are resonantly created in a particular state *P* of the LPB (where $\varepsilon_{LP}(\boldsymbol{k})$ is the lower polariton energy dispersion as a function of the in-plane momentum $\boldsymbol{k}$) by a laser beam with the corresponding energy and incidence angle. If the pump intensity is high enough, polaritons in this state strongly interact with each other: the repulsive interactions between the excitonic component of polaritons cause polaritons to scatter off each

other and there is a high probability for pair-scattering events to take place. In this pair scattering events, a couple of identical pump polaritons $(\boldsymbol{k_P}, \boldsymbol{k_P})$ are scattered towards the signal and idler states $(\boldsymbol{k_S}, \boldsymbol{k_I})$, as it is shown in Fig. 6.1.

The pair scattering events, also called parametric scattering, must satisfy the following energy and momentum conservation rules:

$$2\varepsilon_{LP}(\boldsymbol{k_P}) = \varepsilon_{LP}(\boldsymbol{k_S}) + \varepsilon_{LP}(\boldsymbol{k_I})$$

$$2\boldsymbol{k_P} = \boldsymbol{k_S} + \boldsymbol{k_I}$$

where P, S and I indicate the pump, signal and idler modes, respectively. The particular shape of the LPB (ogee) makes it possible for non degenerate pump, signal and idler modes all to be on resonance with polariton states of the LPB simultaneously, leading to strong nonlinear emissions from microcavities in the strong-coupling.

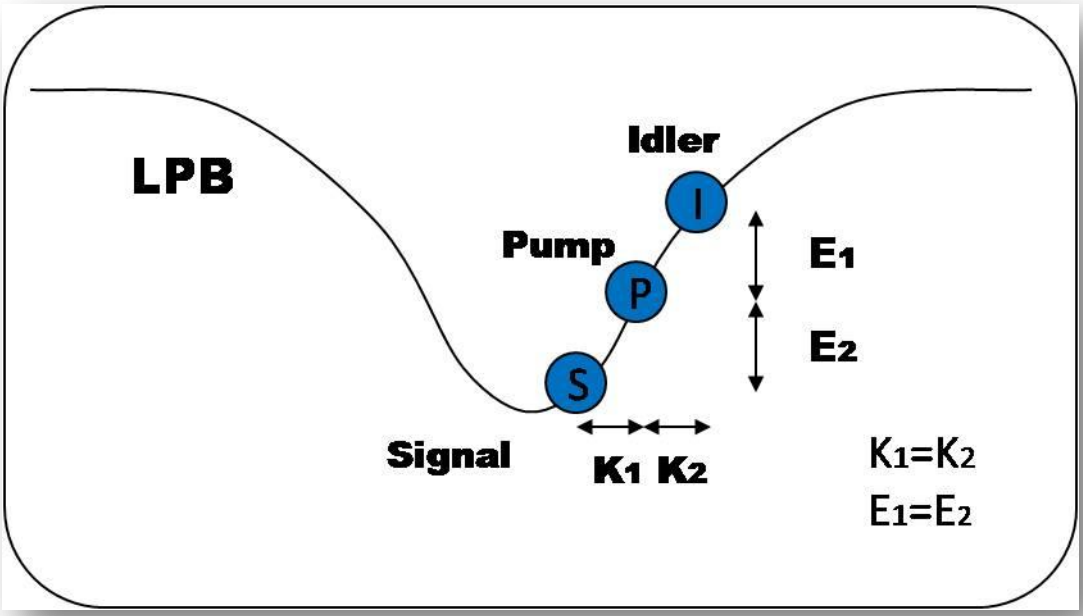

Fig. 6.1: Parametric scattering scheme. The simultaneous resonance of signal, idler and pump with the LPB and the conservation of energy and momentum in the pair scattering scheme are sketch in the figure. This configuration conforms a triple resonant polaritonic optical parametric oscillator.

Pump polaritons, injected at $\mathbf{k} = \mathbf{k_P}$, first create an incoherent polariton population at low and high $\boldsymbol{k}$ through spontaneous parametric scattering processes. These spontaneously created polaritons, due to their bosonic nature, stimulate further scattering out of the pump beam until a threshold is reached, when the gain due to stimulated scattering overcomes the losses. The stimulated parametric scattering at pump powers above the threshold can produce two different type of nonlinear process depending on the experimental conditions: optical parametric amplification (OPA),

when the scattering is stimulated by excitation of the signal mode with a probe beam, and optical parametric oscillation (OPO), where there is no probe and a coherent population in the signal mode appears spontaneously.

Parametric amplification in microcavities was first reported by Savvidis et al.(1), using angle-resolved pump-probe experiments. A pump beam resonantly excited the lower polariton branch at a specific angle ($\boldsymbol{k_P}$), and a probe pulse was made to impinge at normal incidence ($\boldsymbol{k} = 0$) on the sample. The probe reflectivity spectrum was measured by varying the pump angle and when an intense enough pump beam excited the sample at the "magic angle", the probe was strongly amplified (gain $\sim$ 100). The "magic angle" is located near the inflection point of the LPB, where the phase matching conditions 6.1 are simultaneously satisfied. The parametric scattering picture was confirmed by the direct observation of the idler beam at an emission angle corresponding to $2\boldsymbol{k_P}$. This experimentally demonstrated the existence of a very efficient all-optical amplifier through polaritons. The experimental results of ref (1) have been modeled by Ciuti et al.(4) using a quantum treatment of polariton-polariton interaction.

A parametric oscillator (OPO) has been observed by Stevenson et al.(5) and Baumberg et al. (6) in cw experiments with the pump ($\boldsymbol{k_P}$) incident at the inflection point of the LPB. Above a threshold pump intensity, strong signal, at $\boldsymbol{k} = 0$, and idler, at $2\boldsymbol{k_P}$, beams were observed, without any probe stimulation. A classical model accounting for OPA and OPO processes was developed in (7, 8). In the OPO case, the spontaneous emission acts as a spontaneous probe, and the signal emission occurs near the bottom of the LPB.

It is worth to mention that nonlinear emission from microcavities in the strong coupling regime was observed also under non-resonant pumping.(9, 10) In such a case, even being the phenomenology and spectral features similar to those obtained under resonant excitation, the incoherent dynamics and the contribution of the upper polariton branch have to be considered, complicating the theoretical description.

The bosonic nature of polaritons allows stimulated scattering to occur when the intensity of the driving field is increased above some threshold, both under non-resonant and resonant laser excitation. The occurrence of stimulated polariton-polariton scattering, together with the small polariton mass and the favorable shape of the lower polariton branch (with a deep trap at $\boldsymbol{k} = 0$), makes it possible the Bose-Einstein condensation of polaritons at small in-plane wave vectors.(11-17) Polariton states near $\boldsymbol{k} = 0$ are spontaneously populated, seeding the final state stimulation of parametric scattering of polaritons from the reservoir (non-resonant case) or from the pump mode (P) (resonant case). As a consequence of the spontaneous population of $\boldsymbol{k} \approx 0$ states, the lowest pump intensity threshold for the OPO process is always found for a signal at $\boldsymbol{k} = 0$. This is the main reason for the particular configuration with the

signal at $\boldsymbol{k} = 0$ to be privileged in the switching-on of the OPO. The fundamental difference between the resonant and non resonant pumping scheme resides in the incoherent dynamics of polariton relaxation in the latter configuration. The coherence of the emission above threshold in this case originates spontaneously, while in the resonant case the relationship with the driving field has to be taken into account. We will discuss this important point later on.

Polariton states with high momentum are subject to additional scattering processes with respect to those near $\boldsymbol{k} = 0$ due to the larger exciton fraction and the proximity of the exciton reservoir. As a consequence, the absolute intensity of the idler emission is typically $\sim 10\%$ of that of the signal. An interesting configuration for the parametric amplification process is the one of ref (18), where the probe beam (cw, one order of magnitude weaker than the pump) is used to populate a polariton state with high momentum $k_{probe} = k_I$ and stimulate the parametric scattering towards a signal state with small $k = k_S$, as shown in Fig. 6.2. In this way, if the phase matching conditions are satisfied, a strong amplification is obtained for a polariton state with $k_S \neq k_{probe}$. Using this two-beam configuration, a coherent polariton population can be generated at any desired k-vector, which is determined by the chosen wave-vectors of the pump and probe beams and the relations in Eq. 6.1.

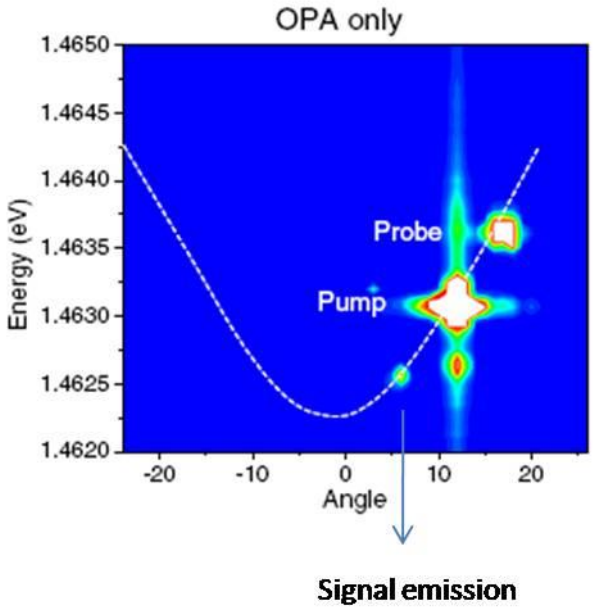

Fig. 6.2: Plot of the emission intensity versus energy and angle for the OPA configuration with the probe at high angles. The bright spots are the positions of the various incoming and emitted beams. The dashed line is a fit to the LPB dispersion. Taken from Ref. (18)

Nevertheless, increasing the pump power, the parametric scattering towards the bottom of the lower branch is stimulated by the polariton population at $k = 0$, formed through relaxation and localization of incoherent polariton scattered off the pump mode. Above the OPO threshold, the OPO switches on and a strong coherent

signal emission appears at $k = 0$ (coupled to an OPO idler), but the OPA signal and idler are still present. A more detailed description of the multiple parametric scattering process and the interplay between OPA and OPO can be found in Ref (18).

6.2 – Coherence

The half-matter, half-light nature of polaritons allows to treat them either in terms of classical Bose-Einstein condensates, where pure matter waves are involved (ultracold atoms), as well as in terms of classical optical parametric oscillators, where pure photons are involved and the passive medium, excited in the transparency region, only provides the nonlinearity of the system. The analogy with Bose-Einstein condensates (BEC) is adopted in non-resonant experiments, while the OPO terminology is often used in relation with the resonant configuration. Anyway, polariton condensates differ in several fundamental aspects from the well understood case of ultracold atoms,(19) and the microcavity OPO presents a much richer and complex physics than that of a classical OPO.(20) Indeed, differently from the case of atomic BEC, microcavities represent an open system, far from the thermodynamical equilibrium; and, differently from photons in a laser, polaritons interact strongly one with each other. In semiconductor microcavities, the boson-boson interaction and the non equilibrium condition are simultaneously present and the interplay of these effects needs new theoretical approaches. When a high density phase of polaritons is formed and a single mode is macroscopically populated, the polariton gas is, in fact, a quantum degenerate, interacting many-body system whose stationary state does not correspond to a thermal equilibrium state but is originated from a dynamical balance of pumping and losses: because of the finite lifetime of polaritons, the polariton condensate has to be continuously replenished from optical injected polaritons in an higher energy state through parametric scattering. Therefore, the coherence properties of this process cover a crucial importance in this discussion.

In this chapter the BEC terminology is used in the sense adopted in the literature about polariton fluids. Polaritons dwell in a quasi-2 dimensional plane and, strictly speaking, a true BEC can form only at temperature $\mathrm{T} = 0$ or in presence of a trap.(21) Anyway, in the presence of interaction, superfluidity and long-range order can exist below a critical temperature (BKT transition).

Recently, theoretical calculations specifically performed on two dimensional polariton systems show that, even without considering BKT effects, when phase fluctuations and internal structure of polaritons are considered, the critical density for

"condensation" follows a dependence on temperature similar to that of a BKT transition.(22)

6.2.1 - Non-resonant pumping

The main aim of non resonant experiments has been to observe spontaneous coherence emerging from incoherent injection of polaritons at energies well above the exciton resonance. As polaritons behaves as bosons, one can expect quantum degeneracy to occur at the bottom of the LPB, as well as final state stimulation and eventually polariton BEC formation. The first unambiguous observation of polariton bosonic stimulation was reported by (9, 23, 24) in CdTe microcavities. In III-V microcavities, the threshold for the final state stimulation is higher than that for the transition to the weak coupling regime, and the stimulated scattering to the ground state was demonstrated only in pump-probe experiment.(25, 26)

The stimulated scattering to the ground state and the nonlinear increase of its population was the first step towards the demonstration of quantum condensation, which owns two other properties: spontaneous coherence and thermalization. However, the short polariton lifetime in the cavity, typically of few picoseconds, and the presence of the bottleneck region, hindered the creation of a thermal population at the bottom of the LPB. Several attempts have been adopted to accelerate the thermalization,(14) but the direct measurement of the polariton population distribution still showed deviations from the proper Bose-Einstein statistics.

Only recently, evidence for polariton condensation has been reported in (13, 14) for CdTe-based and in (27) for GaN based microcavities, combining measurement of the polariton thermalization time with the coherence properties of the emission. Finally, polariton condensation effects have been observed even in GaAs based microcavities, applying a localized pressure to confine the particles in a macroscopic potential trap.(15) It is worth to mention that the angle-dependent emission pattern of a microcavity in the strong coupling regime is very similar to the Bose-Einstein distribution,(28) complicating the experimental proof of observation of a thermalized distribution of polariton for $k \neq 0$.

Despite the observation of polariton BEC, it is evident that new theoretical approaches are needed to properly describe the new physics that could arise in this out-of-equilibrium environment. Real quantum effects, as creation of vortices(29, 30) or superfluidity,(31) well known in the equilibrium case of atomic BEC, are still not

completely clear in the case of semiconductor microcavities, but show the potentiality of microcavity polaritons to study these effects in solid state structures.

6.2.2 - Resonant pumping

In resonant experiments on microcavities, strong evidences of quantum degeneracy and final state stimulation have been reported.(32, 33) In resonant OPA experiment, the stimulated regime is more correctly described as a parametric amplifier rather than a laser, because the population of the lowest mode is amplified by a phase coherent parametric process. Indeed, the polariton-polariton interaction that is at the origin of the observed amplification is a coherent one, which can be identified with polariton four-wave mixing.

In OPO experiments, it has been showed that the quantum degeneracy and the stimulated parametric scattering regime can be reached even without a probe.(2, 6) Stimulated scattering is self initiated when the pump intensity is strong enough so that the final state population (spontaneously created in the signal state, $\boldsymbol{k} \approx 0$) is close to one. Because of the parametric scattering, pumping of the ground state is very efficient, resulting in smaller power threshold for stimulated scattering with respect to the case of a high quality vertical cavity surfaces emitting laser (VCSEL).(6)

The coherence of pump, idler and signal beams in OPA was first studied by Messin and co-workers.(34) They studied the parametric polariton amplifier with an alternative experimental configuration: unlike in the previous references (nondegenerate pump, idler and signal beam), the phase matching conditions were ensured by pumping at normal incidence ($k_P = k_S = k_I = 0$) in a degenerate four-wave mixing configuration. In this geometry it was possible to investigate the dependence of the phase of the signal on the phase of the pump, demonstrating that parametric scattering is a coherent process.

The spectral narrowing of the OPO signal above the threshold, predicted by theory as a consequence of the coherence of the process,(3, 4, 7, 8) was observed in (2, 33, 35, 36). Direct evidence for the coherence nature of the signal was reported in (37), where first order temporal and spatial coherence was demonstrated and the emitted signal was shown to be in a single mode quantum state, rather than in a multi-mode state. The quantum nature of the pair scattering process has been evidenced by the observation of intensity correlations between the signal and idler states. (37-39) The pair correlation of the signal-idler emission has been demonstrated by showing

that polaritons in two distinct idler modes can interfere if and only if they share the same signal mode.(39) The number of particle in the signal and idler states should be identical if only parametric scattering were responsible for their occupation. However, the idler energy and momentum are close to those of the exciton reservoir, which strongly interacts with the idler leading to its very fast spreading in momentum. It is the fast dephasing of the idler what limits the coherence of the OPO.(40)

The macroscopic occupation of the ground state in resonant experiments differs in some way from condensation and spontaneous coherence arising from incoherent pumping. The resonant pump in the OPO configuration is an external coherent driving field which is coupled to the signal, and such driven systems require a specific treatment. While in OPA the phase of the signal is pinned to that of the probe beam, in OPO experiment there is a free phase between the pump and signal modes, which means that, without a probe, the actual phase of the signal is spontaneously chosen (see section 6.5).

It is worthwhile mentioning that in the OPO configuration, even if the signal state presents features associated with the condensed ground state of a BEC, the system as a whole doesn't follow a true Bose-Einstein distribution, as the pump mode is a macroscopically occupied state different from the ground state. Therefore, the properties of the signal state must be investigated in the theoretical framework of an out of equilibrium system.(41)

In (42), Wouters and Carusotto develop a generic theory describing a non-equilibrium condensate, which can be used independently of the specific pumping scheme. A general consequence of the nonequlibrium condition on the dynamic behavior of polaritons is the presence of a diffusive mode, instead of a propagating mode like sound, in the excitation spectrum on top of a polariton condensate. This qualitatively difference, the presence of a diffusive (Goldstone) mode, will be treated with more details in section 6.5.

6.3 – Hydrodynamics

The time-resolved spectroscopy experiments on resonantly pumped polaritons allow the investigation of the hydrodynamical properties of the injected "polariton fluid".(43) In (44), Carusotto and Ciuti proposed an experiment to study the hydrodynamical properties of the polariton fluid by looking at the resonant Rayleigh scattering. A strong pump beam creates a large coherent population of polaritons with a defined non zero momentum, so to generate a polariton fluid with non-zero flow velocity along the cavity plane. In the presence of disorder, static defect are known to produce resonant Rayleigh scattering (RRS) of the exciting laser field.(45, 46) At low power, the RRS produces a ring emission pattern in the momentum space at the energy of the pump, as polariton are elastically scattered to states with different momentum but same energy. However, since a large coherent population of polaritons modifies the polariton dispersion relation, at higher pump powers, both the shape and the intensity across the pattern of resonantly scattered polaritons change. In particular, the strict connection between the dispersion of the elementary excitations of a polariton quantum fluid and the intensity and shape of the RRS on defects has been addressed.(44). Superfluidity of polariton, e. g. the possibility of frictionless flow, which is a manifestation of macroscopic coherence, produces a quenching of the RRS intensity when the flow velocity imprinted by the pump is slower than the sound velocity in the polariton fluid. The observation of polariton superfluid effects would be a direct manifestation of the quantum nature of polaritons.

As we have already seen, convincing evidences for polariton Bose-Einstein condensation have been reported in non-resonant configurations. However, these observation do not differ significantly from what can be found in a pure photonic laser.(28) Nevertheless, while big theoretical efforts have been dedicated to this subject,(47, 48) only few experiments in the literature addressed the issue of polariton movement. In ref (49, 50), the observed states do not conformed a polariton fluids with macroscopic occupations, as they are populated by the incoherent scattering from other polariton states. Recently, Langbein and collaborators observed polariton flow in semiconductor microcavities,(51) but in this case the propagation of polariton was incoherent, with a very fast decay ($\sim$ 4 ps, of the order of the polariton lifetime in the cavity). A conceptually new experiments has been reported in (52), where polaritons are excited in the OPO configuration and the polariton fluid is observed in real and momentum space. To obtain a polariton fluid with a finite velocity, a probe pulse was made to impinge at resonance with the LPB at high angles. If the phase matching conditions are satisfied, a signal state, with $\boldsymbol{k_S} \neq 0$, would be macroscopically occupied. In this experiment, non-equilibrium long-living polariton coherent states with finite velocity are created and the effects of local defects on the

polariton fluids are probed. Ćerenkov waves were observed for polaritons coherently created $\sim 1\ meV$ above the bottom of their dispersion, while superfluid behavior was found for polaritons running at lower energies and momenta. In presence of small defects, the coherent polariton gas that remains in a superfluid regime passed through the obstacle without changing its velocity. When the physical size of the obstacle became comparable to that of the polariton jet, elastic scattering resulted in splitting the polariton fluid in two daughter states with different in-plane momentum vectors.

6.4 – Parametric scattering

The theoretical description of parametric scattering of polaritons can be restricted to the lower polariton branch only, assuming that dynamics takes place only there and the population of the upper polariton branch remains negligible. We will follow here a mean field description of the cavity polariton field dynamics, as in ref (53), developed in terms of a nonlinear wave equation (polaritonic Gross-Pitaevskii equation) with a third order nonlinearity for a single-component k-space polariton field $\psi_{LP}(k)$:

$$i\frac{d}{dt}\psi_{LP}(k) = \left[\varepsilon(k) - i\frac{\gamma(k)}{2}\right]\psi_{LP}(k) + F_p(k)e^{-iw_p t} + \sum_{q_1,q_2} g_{k,q_1,q_2}\psi^*_{LP}(q_1+q_2-k)\psi_{LP}(q_1)\psi_{LP}(q_2).$$

The field $\psi_{LP}(k)$ is normalized in such a way that its square modulus $|\psi_{LP}(k)|^2$ equals the number of polaritons with momentum k per unit area. $\varepsilon(k)$ is the dispersion relation of the lower polariton and $\gamma(k)$ is its loss rate. The exciting laser field, with driving amplitude $F_p(k)$, is a monochromatic and continuous-wave coherent field with frequency ω_P and momentum k_P, circularly polarized and with a plane-wave spatial profile.

The last term of the equation, the third-order nonlinear interaction, takes into account the exciton-exciton collisional interactions.(54, 55) The exciton-exciton coupling constant in a single quantum well can be approximated by a momentum-independent value $\bar{g}$, because the wave vectors involved are much smaller that the inverse exciton radius (If N_{QW} are present in the cavity, the effective excitonic coupling constant is $g = \frac{\bar{g}}{N_{QW}}$). Since the equation has been written in the polaritonic basis, the momentum-dependent excitonic fraction has to be taken into account through the

Hopfield coefficients $X(k)$ and $C(k)$, quantifying the exciton and photon components of the lower polariton branch:

$$g_{k,q_1,q_2} = gX^*(k)X^*(q_1+q_2-k)X(q_1)X(q_2). \quad 6$$

Equation 6.2 can be used to describe a generic OPO, as a planar cavity containing a slab of passive nonlinear $\chi^{(3)}$ material. In this case, no exciton-photon coupling exists and polaritons reduce to bare cavity photons. The nonlinear coupling constant would be obtained using the nonlinear susceptibility $\chi^{(3)}$ of the medium under consideration:

$$\hbar g \approx \chi^{(3)} \frac{(\hbar\omega_P)^2}{\epsilon_{lin}^2 d},$$

where ϵ_{lin} is the dielectric constant of the medium and d its thickness. Typical values of $\chi^{(3)}$ of nonlinear materials used in optical applications are of the order of 10^{-9} esu ((53)), which gives a nonlinear coupling constant $\hbar g \approx 5 \times 10^{-9} eV\mu m^2$. In semiconductor microcavities in the strong coupling regime, the theoretical prediction $\hbar g \approx 1.5 \times 10^{-5} eV\mu m^2$ ((53)), in reasonable agreement with available experimental data,(47, 56) corresponds to a coupling constant 3-4 order of magnitude larger than that of usual nonlinear materials. This explains the great interest covered by semiconductor microcavities for low-power nonlinear optical applications.

The exact solution of the set of equations of motion can be found in the form

$$\psi_{LP}(x,t) = Pe^{i(k_p x - \omega_p t)}, \quad 6$$

with the amplitude P fixed by the condition (7)

$$\left[\varepsilon_p - \omega_p - \frac{i}{2}\gamma_p + g\left|X(k_p)\right|^4 |P|^2\right] P + F_p = 0. \quad 6$$

where $\varepsilon_P = \varepsilon(k_P)$ is the pump-mode energy in the linear regime and $\gamma_P = \gamma(k_P)$ is the corresponding linewidth.

The optical nonlinearity of microcavities originates from the exciton-exciton interaction and is therefore of the $\chi^{(3)}$ type. It not only provides the parametric interaction necessary for the parametric oscillation, but is also responsible for significant mean-field frequency shift of the modes. The effect of the third-order nonlinearity is to renormalize the pump mode frequency by a mean-field shift proportional to the excitonic population of the mode, $n_{xp} = \left|X(k_p)\right|^2 |P|^2$. This effect, absent in $\chi^{(2)}$ classical OPO, has extremely important consequences. Depending on the sign of the detuning between the pump frequency ω_p and the polariton energy

$\varepsilon(k_P)$, OPO could be is in the optical limiter regime or in the bistability regime (see Fig. 6.3).

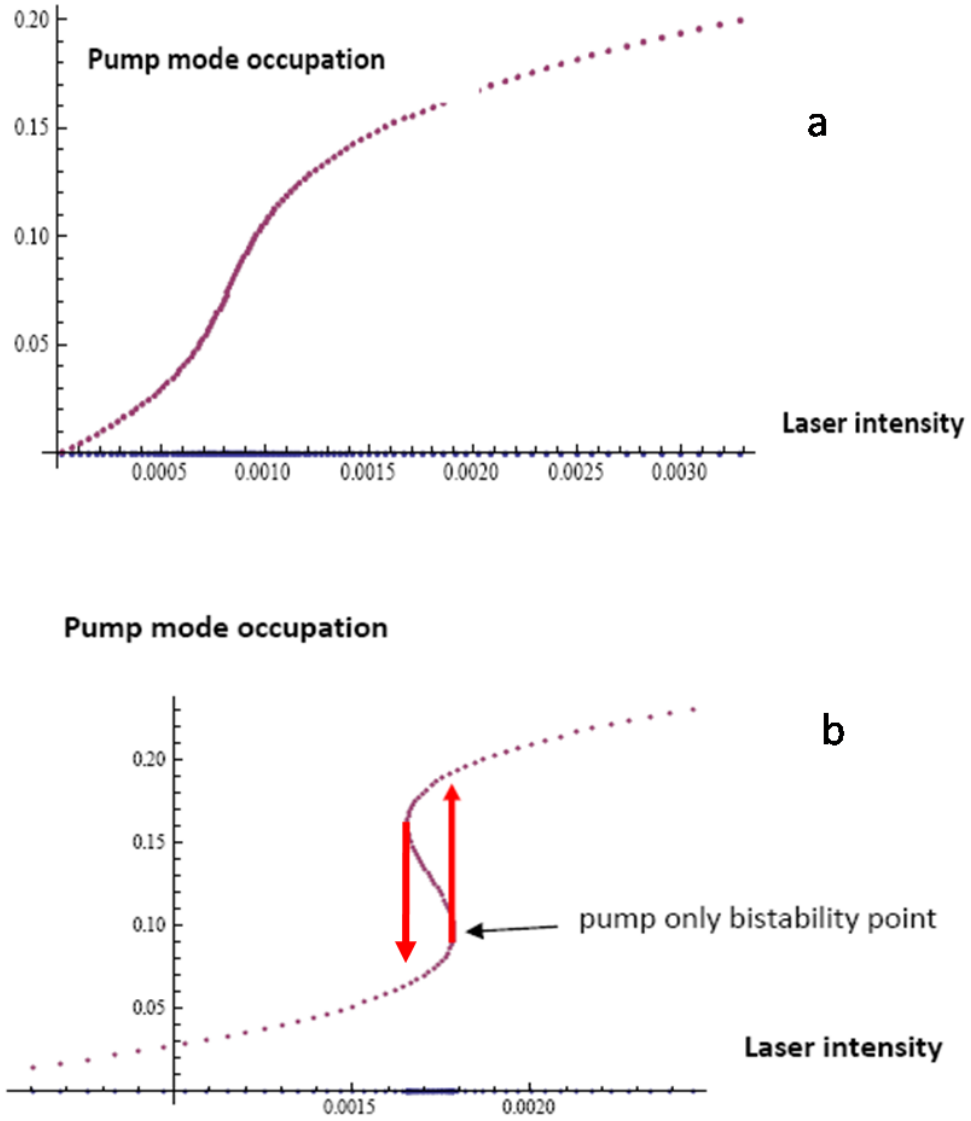

Fig. 6.3: Pump mode occupation versus laser intensity for an OPO in: (a) optical limiter regime; (b) bistability regime.

The solution of the cubic equation (Eq. 6.5), is well known:(8) when the detuning $\omega_p - \varepsilon_p < {\sqrt{3}}/{2}\,\gamma_p$, we are in the so-called optical limiter regime (Fig. 6.3(a)), in which the population of the pump mode monotonically increases as a function of the driving intensity I_p, while for blue-detuned frequency $\omega_p - \varepsilon_p > {\sqrt{3}}/{2}\,\gamma_p$, a positive feedback occurs (the effect of the renormalization is to shift the polariton

resonance towards the pump frequency) and an hysteric behavior can be observed as in Fig. 6.3(b).(53, 57) In this latter case, for increasing laser intensities, the pump mode population follows the lower branch until its endpoint is reached and then it jumps to the upper branch (upward red arrow). For decreasing intensities, the pump mode population follows the upper branch until its endpoint, and then jumps back to the lower branch (downward red arrow). As can be seen in Fig. 6.3(b), the upward and downward jump points do not coincide, and the hysteretic behavior of the system is evident.

6.5 - Dynamical stability of the pump-only state

The parametric oscillations switch on as soon as the incident intensity exceeds the threshold value for some pairs of signal-idler modes. Optical parametric oscillations, as well as the instability of the central branch of the hysteresis loop, are due to the solution of 6.5 becoming dynamical unstable. The stability of the pump only solution 6.5 is determined by considering the spectrum of small excitation with frequency ω and wave vector k:(8, 53)

$$\psi_{LP}(x,t) = e^{i(k_p x - \omega_p t)}\left[P + u(q)e^{-i(qx-\omega t)} + v^*(q)e^{i(qx-\omega^* t)}\right],$$

which describes signal and idler modes with wave vectors $k_s = k_p - q$, $\omega_s = \omega_p - \omega$ and $k_i = k_p + q$, $\omega_i = \omega_p + \omega$.

This ansatz allows for finite amplitudes in the pump, idler and signal modes, while all other modes are assumed to remain empty. This is a good approximation until the possible occupation of other modes via multiple scattering processes is small and would give only quantitatively small corrections.

Introducing Eq. 6.6 in Eq. 6.2 and expanding to the first order of the perturbation, it reduces to the following eigenvalue problem

$$L\,(k_s)w(k_s) = \omega(k_s)w(k_s),$$

where $w(k_s)$ is the two-component displacement vector $w(k_s) = [u(k_s), v(k_s)]^T$ and the 2×2 matrix $L\,(k_s)$ is given by:

$$L\,(k_s) = \begin{pmatrix} \epsilon_s - \omega_p + 2g|X_s|^2\left|X_p\right|^2|P|^2 - i\frac{\gamma_s}{2} & gX_s^*X_iX_p^2P^2 \\ -gX_sX_i^*X_i^{*2}P^{*2} & -\epsilon_s + \omega_p - 2g|X_i|^2\left|X_p\right|^2|P|^2 - i\frac{\gamma_i}{2} \end{pmatrix}.$$

The possible solutions are given by imposing that the determinant of the coefficient is zero, that would give two complex eigenvalues $\omega_{\pm}(k_s)$.

The condition for the dynamical stability is obtained when the imaginary parts of all eigenvalues of $L\ (k_s)$ are negative ($Im[\omega_{\pm}(k_s)] < 0$) for all wave vectors k_s,

$$Im[\omega_{\pm}(k_s)] = -\frac{\gamma_s + \gamma_i}{4} \pm Im\left\{\sqrt{\left[\left(\epsilon_{si} - \omega_p\right) + g(|X_s|^2 + |X_i|^2)n_{xp} - i\frac{\gamma_s - \gamma_i}{4}\right]^2 - g^2|X_s|^2|X_i|^2 n_{xp}^2}\right\},$$

where $\epsilon_{si} = \frac{[\epsilon_s + \epsilon_i]}{2}$. Two kinds of physically distinct instabilities can arise: a single mode instability, which involves the pump mode alone, and a parametric instability, with $k_s \neq k_p$. Parametric oscillation takes place at the threshold for this parametric instabilities, when a finite intensities appears in a pair of distinct signal/idler modes at $k_{s,i}$. A detailed discussion on the different type of instabilities can be found in (53). The conditions under which OPO switches on have been studied also by Whittaker, using an equivalent classical formalism, including the contribution of signal and idler populations to the energy renormalization.(8) The theory predicts that a simple bistable behavior occurs for small angles $(< 10°)$, while for angles greater than $10°$, the OPO switches on. The OPO threshold is found to vary smoothly with pump angle and energy, giving no special significance to the “magic angle” (on the contrary, in ultrafast amplification experiment, the gain is strongly peaked around the magic angle conditions).

Experimentally, the OPO signal emission has been always observed in a direction within few degrees of the surface normal. If the signal angle were simply determined by the requirement that the mismatch of the signal and idler energies from the polariton dispersion is minimized, a wider range of angles would be obtained, depending on the pump energy and angle. Actually, it happens for pump intensities very close to the threshold, while at higher powers the renormalization contributions from the signal and idler switch off the high angle OPO and pull the small angle states into resonance.

The occupation values of the pump and signal modes in the stationary state are plotted in Fig. 6.4, as calculated in Ref. (53), versus the pump intensity for a pump frequency $\omega_p < \epsilon(k_p)$, which corresponds to the optical limiter case. For pump intensities within a certain range, the pump only solution becomes dynamically unstable and the onset of parametric oscillation results in a finite population of the signal mode. Outside this range, the pump only solution remains dynamically stable and the amplitudes of the signal and idler modes are zero.

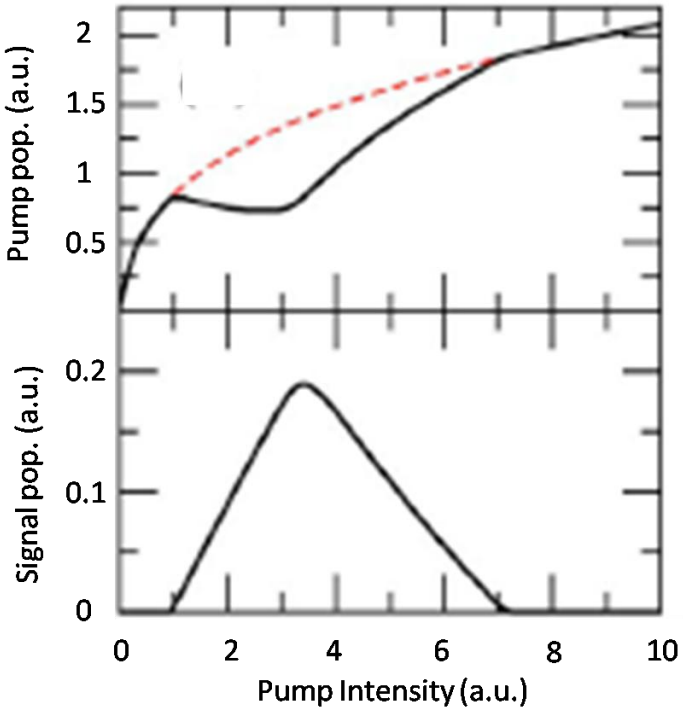

Fig. 6.4: Pump (upper solid curve) and signal (lower panel curve), exciton density as a function of the pump power. The dashed line is the pump intensity in the pump-only solution (from Ref. (53)).

While the amplitude P of the pump mode is completely determined, both in modulus and phase, by the incident laser beam, a free parameter remains in the choice of the signal and idler phases, due to the invariance of the equation of motion and the interaction Hamiltonian under a simultaneous phase rotation of the signal and idler in opposite direction:

$$S \to Se^{i\Delta\emptyset} \qquad I \to Ie^{-i\Delta\emptyset}. \tag{6}$$

It means that the sum of the idler and signal phases is fixed by the pump phase, $\phi_{pump} = \phi_{signal} + \phi_{idler}$, but still the system presents a phase-rotation symmetry (U(1)).

In the parametrically oscillating states, S and I have finite values, so that this U(1) phase-rotation symmetry is spontaneously broken during the OPO formation. In the absence of external perturbation, at each realization of the experiment, a specific value of the phase of S, and consequently of I, is randomly selected. As a consequence of the phase-rotation symmetry, no restoring force applies to a simultaneous and opposite rotation of the signal and idler phases, which slowly diffuse in time under the effect of fluctuations.(41)

6.6 - Response to a weak perturbation and the Goldstone mode

When spatial twists of the signal/idler phases are created by an extra probe laser F_r at frequency $\omega_r = \omega_s + \Delta\omega$ and wave vector $k_r = k_s + \Delta k$ close to the frequency and the wave vector of the signal, $|\Delta k| \ll |k_s - k_p|$, the spontaneously broken symmetry manifests itself as a strong response of the system. If the applied perturbation is weak, the response of the system can be calculated by linearising the mean-field equation of motion (6.2) around the solution (6.6), which can be made by modifying the eigenfunction of the signal S, the idler I and the pump P modes as:

$$S \to S + u_s e^{i(\Delta k x - \Delta\omega t)} + v_s^* e^{-i(\Delta k x - \Delta\omega t)}$$

$$P \to P + u_p e^{i(\Delta k x - \Delta\omega t)} + v_p^* e^{-i(\Delta k x - \Delta\omega t)}$$

$$I \to I + u_i e^{i(\Delta k x - \Delta\omega t)} + v_i^* e^{-i(\Delta k x - \Delta\omega t)}.$$

The deviations from the steady state can be grouped in a 6 component vector $\mathcal{U} = (u_s, u_p, u_i, v_s, v_p, v_i)^T$, that, under the weak probe F_r, obeys the equation

$$\Delta\omega\mathcal{U} - \mathcal{L}(\Delta k)\mathcal{U} = \mathcal{F}_r$$

where the force vector reads $\mathcal{F}_r = (F_r, 0, \dots, 0)^T$. The detailed calculation can be found in Ref. (41), here we will just point out the physical meaning of the equation 6.14 and its eigenvalues. The square modulus of the first element u_s of the system response $\mathcal{U}$ corresponds to the number of polaritons created in the k_r mode. The real and imaginary part of the Bogoliubov matrix $\mathcal{L}(\Delta k)$ give respectively the frequency and linewidth of the elementary excitations around the parametrically oscillating stationary state and fix the shape of the luminescence peaks under the considered excitation configuration. Plotting the eigenvalues of 6.14 as a function of Δk, as in Fig. 6.5, the Bogoliubov dispersion of the excitations around the signal is obtained.

In particular, in the real part of the dispersion is present a soft Goldstone branch (marked as (G) in Fig. 6.5) of eigenvalues $\omega_G(\Delta k)$ which tends to exactly zero for $\Delta k \to 0$. The presence of this branch is a direct consequence of the spontaneous breaking of the symmetry of the idler/signal phase and corresponds to a spatially varying twist of the signal/idler phases for finite values of Δk. The existence of a Goldstone mode is a general feature of both non-equilibrium and equilibrium systems when a spontaneous symmetry breaking occurs.

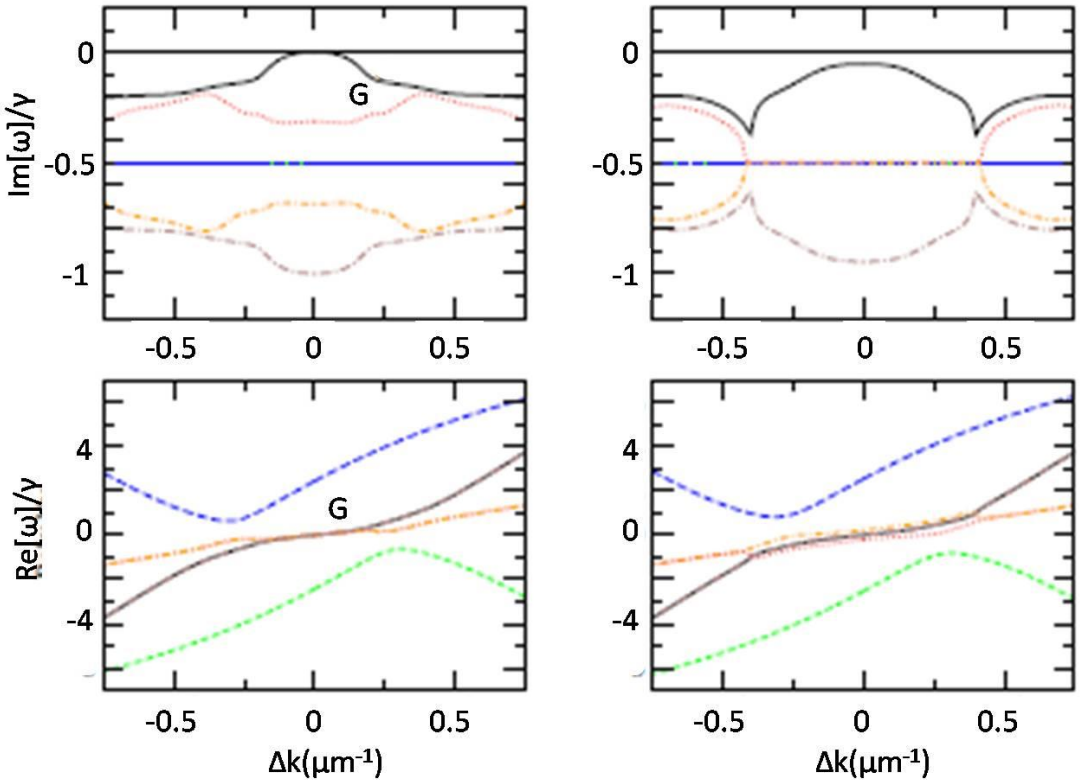

Fig. 6.5: Imaginary (upper panels) and real (lower panels) part of the dispersion relation of the excitations around the stationary state for the pump intensity corresponding to the dashed line in Fig. 6.4. The left-hand panels refer to the case in which the signal-idler phase rotation symmetry is spontaneously broken and a Goldstone mode (G) is present (solid line). The right-hand panels refer to the case in which a probe laser beam is applied at the signal state, so that the phase rotation symmetry is explicitly broken and a gap opens in the dispersion relation. Taken from Ref. (41).

Nevertheless, in a Bose system at equilibrium, the Goldstone mode dispersion shows a singularity at $k = 0$ ($Re[\omega(k)] \simeq c_s|k|$ around $k = 0$) and corresponds to a weakly damped sound waves which in the long wavelength limit propagate at the speed of sound, c_s. In non-equilibrium systems, like in the present case of a planar OPO, the real part of the Goldstone mode goes as $Re[\omega(\Delta k)] \propto \Delta k$, while the imaginary part goes as $Im[\omega(\Delta k)] \approx -\propto (\Delta k)^2$ for small Δk with $\propto > 0$. It results in a narrowing of the linewidth of the Goldstone peak as $\Delta k \to 0$. Since the lifetime is inversely proportional to the linewidth, the lifetime of the Goldstone mode increases with $\Delta k \to 0$ as $\sim \frac{1}{(\Delta k)^2}$.

The physical meaning of such features is that the Goldstone mode of a planar OPO, consisting in a spatially varying twist of the signal/idler phase, does not propagate as a sound wave, but has a diffusive and overdamped character: once a localized perturbation is created, this will relax back to the equilibrium state while being dragged by the pump polariton flow. This diffusive Goldstone mode has been

addressed recently as a general feature of non-equilibrium systems, independently of the coherent (as in the OPO configuration) or incoherent (as in polariton Bose-Einstein condensation) nature of the pumping source.

The preceding model and conclusions are valid within the linear response approximation, which means for low enough values of the probe laser intensities. In particular, numerical simulations have shown that linear response theory holds as long as the polariton density in the probe mode is smaller than those of the signal and idler modes, avoiding the parametric emission to take place in the probe mode.

As it happens to the magnetization of a ferromagnetic material, which can be oriented by the application of an external magnetic field, in microcavity OPOs the symmetry can be explicitly broken by pinning the signal/idler phase with an extra-laser beam which stimulates the parametric emission. When the extra-laser beam is applied at the frequency and wave vector of the signal emission, stimulated processes push the parametric emission to preferentially occur with a phase pinned to the incident extra-laser one. Three different situations are possible in this case, depending on the energy ω_r and momentum k_r of the extra-laser beam and on its intensity I_r:

1) When $\omega_r = \omega_s$ and $k_r = k_s$ (extra laser exactly on resonance with the signal parametric emission), the linear response theory cannot be applied and the extra laser beam has to be included from the beginning as an additional driving term in the equation of motion. In this case, in addition to pinning the phase of the signal, the effect of the extra beam is to increase the signal intensity. The linear response theory can then be used to calculate the Bogoliubov dispersion of the new solution. The imaginary part $Im[\omega_G(\Delta k)]$ presents now a finite gap (see right panels of Fig. 6.5) at $\Delta k = 0$ and therefore:

   - no Goldstone mode exists any longer

   - the damping rate of Bogoliubov excitations is finite for any value of Δk, because $Im[\omega(\Delta k)] \neq 0$ for any Δk.

   Differently from the equilibrium case, where the presence of the external field which explicitly breaks the symmetry, opens a gap in the real part of the dispersion law, in non-equilibrium systems the gap appears in the imaginary part of the dispersion. This results in a finite damping rate of Bogoliubov excitation even for $\Delta k = 0$, which means, in a probe transmission experiment, a dramatic broadening of the Goldstone peak (and consequently a decrease of the lifetime) with respect to the case of spontaneously broken symmetry.

When the extra laser and the OPO signal emission are slightly detuned, $\omega_r = \omega_s + \delta\omega_s$, two regimes must be distinguished depending on the extra-laser intensity I_r:

2) For small I_r, the only effect of the extra beam is to induce a small perturbation on the top of the parametric oscillation state at the natural frequency ω_s, and can be described within the linear response theory discussed before.

3) For I_r large enough to force parametric oscillation to occur at the extra-laser frequency $\omega_s + \delta\omega_s$, the linear-response theory cannot be applied. The stationary state recovers the form 6.6 but with the signal/idler frequency replaced by $\omega_{s,i} \rightarrow \omega_{s,i} \pm \delta\omega_s$. This corresponds to the situation of forced stimulated process imposed by the extra laser beam described above (1)).

The transition from probing the Goldstone mode (case (2)) to forcing the parametric oscillation at a slightly different frequency (case (3)) depends on the intensity of the extra laser beam. The phenomenology does not change if a wave vector mismatch, in addition to the frequency mismatch considered here, between the extra beam and the signal emission is included as well.(41)

In the previous discussion, the effect of the disorder has not been included: this is a valid approximation for high quality samples; nevertheless, it has been shown that the interplay of spatial inhomogeneities with the nonlinear dynamics has important effects on the coherence properties of the optical parametric oscillator. In Ref. (58), spatially and spectrally resolved real space images of the polariton signal are obtained in order to study important features of the high density phases, such as coherence and polarization properties, unperturbed by spatial averaging. The blueshift of the lower branch (which occurs when the OPO crosses the threshold into the high density regime) due to polariton-polariton quasi-particle interactions, and in-plane potential fluctuations in the microcavity, result in different localized regions in the signal distribution. The signal emission is found to consist of independent modes emitting at slightly different energies. The coherence times of the different modes as a function of the state occupancy reveals a very different behavior to that in a laser, where the photons emitted in the stimulated scattering process are non-interacting.

6.7 – Long-lived polariton states in semiconductor microcavities across the parametric threshold

While the BEC formation in systems close to thermodynamical equilibrium has been observed and described in the literature,(59, 60) recent experimental works show the necessity of extend the many-body theory of quantum fluids to system whose stationary states arises from the interplay of an external driving field with dissipation effects.(17) Even though many concepts directly extend to this non-equilibrium case, e.g. phase transition and order parameter, a deeper investigation is required for several other properties which appear to be severely modified, e.g. superfluidity.(31) Several groups have reported the observation of spontaneous coherence in spatially extended systems of polaritons far from thermodynamical equilibrium with mechanisms that can be interpreted as non-equilibrium analogs of Bose-Einstein condensation (BEC).(17) In spite of the different pumping schemes (resonant for the OPO case, non-resonant for the so-called polariton BEC case ((13, 15, 61)), a U(1) symmetry is spontaneously broken in all cases and coherence is not simply inherited from the pump beam.

Along with the changing nature of the polariton fluid, the life time of elementary excitations is dramatically modified for increasing pump intensity. Indeed, the imaginary part of the Goldstone branch actually represents the inverse of the lifetime of the elementary excitation around the signal emission.

An alternative configuration is presented here in order to study the response of the OPO to a pulsed perturbation. A weak pulsed beam, applied at the idler position, is used to probe in real time the dynamics of the system around the pump-only stationary state. The signal emission is time- and energy-resolved to allow the measurement of the elementary excitations behavior at the OPO transition.

The steady state of the system is probed by injecting extra polaritons by means of a weak pulsed beam, and the decay time of the response is measured as a function of the pump intensity. A dramatic slowing down of the dynamics is observed as the threshold is approached from below: close to the threshold, the decay time can become orders of magnitude longer than the typical life time of polaritons, and it remains very long even well above the threshold. Good agreement between the experimental observations and the theoretical model based on the generalized polariton Gross-Pitaevskii equation is found. In particular, this observation suggests the possibility of investigating the polariton dynamics beyond the limits imposed by the intrinsic polariton life time.

The studied microcavity is composed by a *AlAs* $\lambda/2$ cavity with a top (bottom) Bragg mirror of 15 (25) $Al_{0.1}Ga_{0.9}As/AlAs$ pairs, grown on a *GaAs* substrate. A $20\ nm$

wide *GaAs* quantum well is embedded at the antinode position of the cavity mode. The sample is kept at a constant temperature of $10\ K$. The quantum well excitons are in strong coupling with the cavity mode, with a Rabi splitting of $4.4\ meV$. The cavity-mode is at resonance with the exciton energy, i.e. the detuning is $\delta = 0$ for the experiment performed here. A more detailed description of the sample can be found in section 3.1.2. A continuous-wave laser source $(Ti{:}\,Al_2O_3)$, named *Pump* hereafter, is used to excite the sample with an incident angle of $10°$. A *2* ps pulse (*Probe*), coming from a different laser source with a repetition rate of 82 MHz, is focused within the *Pump* spot and impinges on the sample with a tunable incident angle. Photoluminescence is collected and analyzed by a spectrograph coupled either to a streak- or a conventional CCD-camera. The emission in the far field is visualized by focusing a lens on the Fourier plane $(k_x; k_y)$: a direction k_y of this plane is selected and energy-resolved by the spectrograph, allowing the direct experimental observation of any two-dimensional section $(k_x; Energy)$ of the polariton dispersion on the CCD camera (see section 3.3). Temporal-resolved PL images are obtained by the streak camera in both configurations $(Energy; Time)$ and $(k_x; Time)$, allowing a complete study of the dynamics at different energies and momenta.

The *Pump* impinges on the sample in resonance with the LPB, allowing the direct injection of polaritons at the pump state with wave vector and energy $(k_P; \varepsilon_{LP}(k_P))$. The polariton-polariton interaction couples the pump state to the signal and idler states $(k_{s,i}; \varepsilon_{LP}(k_{s,i}))$ and the onset of parametric oscillation, which is obtained for pump powers above the threshold $I_p^{th} = 12.5\ mW$, results in the macroscopical occupation of the signal state at $(k_S = 0; \varepsilon_{LP}(0))$. This corresponds to the particular scattering process $\{k_P; k_P\} \rightarrow \{0; 2k_P\}$, which has been demonstrated to be the selected one in pump-only configurations due to its lowest threshold value. One of the effect of the $\chi^{(3)}$ nonlinearities is to renormalize the polariton branch by a quantity proportional to the excitonic population. This implies that with increasing pumping intensities, one has to consider the renormalized polariton dispersion $\tilde{\varepsilon}_{LP}(k_P)$. For this reason, the *Pump* frequency $\omega_P = 1.5273\ eV$, with a linewidth of $0.1\ meV$, is set slightly above the energy $\varepsilon_{LP}(k_P)$ of the LPB under low pumping. In order to avoid complications arising from the optical bistability scenario, the detuning between the pump frequency and the lower polariton branch is kept in the range of the optical limiter, that is $(\omega_P - \varepsilon_{LP}(k_P) \sim \gamma(k_P)$, where $\gamma(k_P) \approx 0.4\ meV$ is the LPB linewidth at k_P.

Firstly, we have investigated the stationary-state polariton emission in the absence of the *Probe*. To clearly identify the threshold, we have studied the energy of the signal emission as a function of *Pump* power I_p (full triangles in Fig. 6.6). A smooth and almost linear blueshift of the signal energy is visible at low pump powers, while a sudden jump appears for I_p just above 12 mW, due to the onset of parametric oscillation. Such a discontinuous behavior around the threshold was predicted in Refs

(8, 53): below the threshold, the energy of the incoherent parametric luminescence is indeed fixed by the slightly blue-shifted LPB dispersion, while above threshold it is determined by a more complex OPO dynamics that also involves the idler energy. Far above threshold, the blue-shift saturates. The PL intensity of the signal emission, as a function of I_p, is plotted in Fig. 6.6 and confirm that the appearance of nonlinearities occurs for $I_p = 12.5\ mW$.

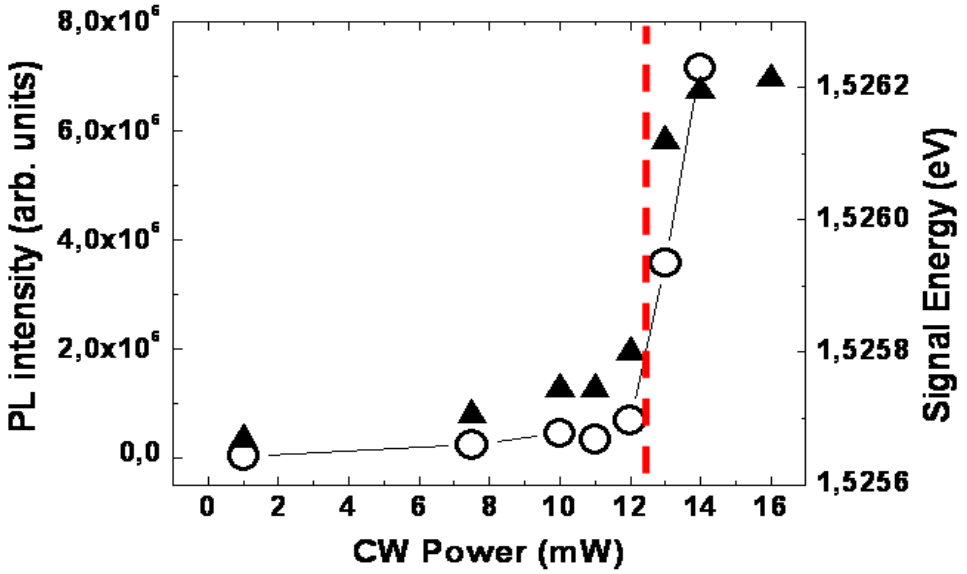

Fig. 6.6: Energy (full triangles) and PL intensity (open circles) of the signal versus pump power. The red dashed line indicates the pump intensity threshold.

Typical energy-momentum emission patterns are shown in Fig. 6.7 for two different values of I_p. Although the pump wavevector lies well outside the k-space region imaged in Fig. 6.7, a small polariton occupation of the LPB bottom still appears as a consequence of incoherent relaxation processes even at low pump powers (lower panel). As the polariton density is very low, the photoluminescence spectrum is concentrated on the linear-regime LPB branch. At higher pump intensities, polariton-polariton interactions are able to significantly modify the emission pattern and, in particular, are responsible for parametric processes, where two pump polaritons at k_p are transformed into a pair of signal and idler polaritons of wavevectors $k_{s,i}$, respectively.

The onset of parametric oscillation is clearly visible in the emission pattern for *Pump* intensities above the threshold $I_p^{th} = 12.5\ mW$ (upper panel of Fig. 6.7): the occupation of the signal at $k_s = 0$ becomes in this case very large and the linewidth of the emission in energy is substantially reduced as compared to the bare LPB linewidth (see Fig. 6.7). The spectral narrowing in energy is accompanied by a significant

broadening of the k-space emission. The full width half maximum (FWHM) of the emission below and above threshold is of $0.41\ \mathrm{meV}$ and $0.16\ \mathrm{meV}$ respectively, which is consistent with what is expected from the onset of the OPO regime. The flat shape of the coherent OPO emission in the $(k_x; E)$ plane is however more likely to be a consequence of the peculiar shape of finite-size non-equilibrium condensates, as discussed in Ref. (62), rather than an evidence of the diffusive nature of the Goldstone mode.(41)

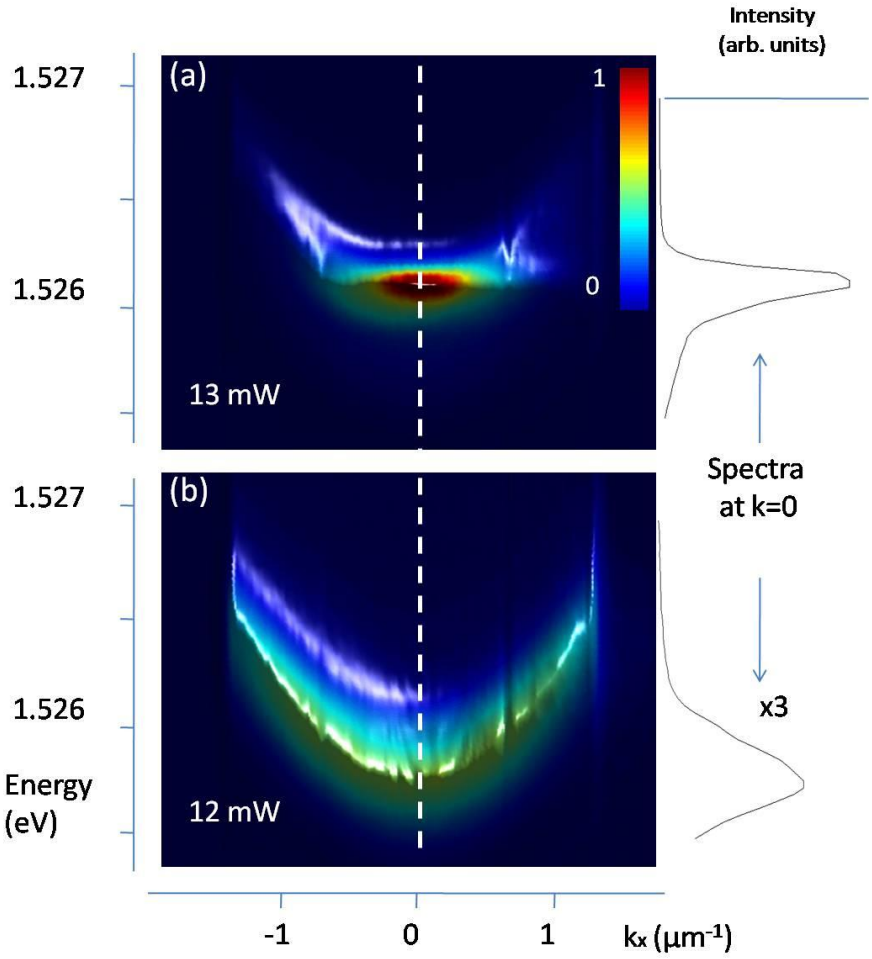

Fig. 6.7: Direct experimental observation on the CCD camera of a two-dimensional section $(k_x; E)$, with $k_y = 0$, of the lower polariton dispersion for pump powers I_p (a) just above (13 mW) and (b) below (12 mW) the OPO threshold $I_p^{th} = 12,5\ mW$. The energy spectra at $k_x = 0$ (dashed line in the figure) are depicted on the right, with a magnification of a factor 3 for the lower panel of the figure. The PL emission is normalized to 1 and plotted in a linear color scale.

The main goal our experiments is to study the response of the system in its stationary state to an additional weak $(\leq 0.2\ mW)$ *Probe* pulse that impinges on the sample at a large angle of $20°$, which is near the idler position. The evolution of the system in response to the *Probe* pulse is monitored by investigating the time- and

momentum-resolved signal emission and, in particular, its decay time. As an example, we have traced in Fig. 6.8 the time-evolution of the difference

$$\Delta I_s = PL(Pump + Probe) - PL(Pump)$$

between the signal emission intensity in the presence and in the absence of the *Probe*, respectively, for three different *Pump* intensity values.

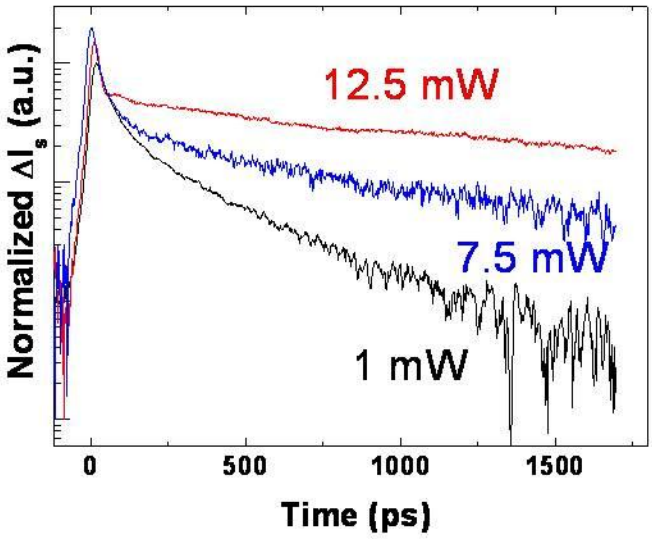

Fig. 6.8: Time evolution of the energy-integrated signal emission ΔI_s for three different values of I_p $(1\ mW, 7.5\ mW, 12\ mW)$.

Right after the arrival of the *Probe* pulse, parametric scattering of pump polaritons into the signal state is stimulated by the small population of the new idler polaritons injected by the *Probe*: in the plotted curves, this corresponds to a fast switch-on of the ΔI_s at the *Probe* arrival time. The fast decay on a 30 ps scale is then followed by a much slower exponential decay on a time scale in the 100 ps range, i.e. orders of magnitude longer than both the empty cavity decay time (2 ps) and the polariton-polariton scattering time,(63) but still significantly shorter than the *Probe* repetition time of approximately 12 ns).

As easily seen by comparing the three curves shown in Fig. 6.8, the response of the system strongly depends on the intensity I_p of the *Pump*. While the decay time of the fast transient decreases for increasing *Pump* powers and eventually goes below the streak-camera resolution of $\sim 30\ ps$, the long decay-time significantly increases with I_p. This latter dependence is summarized by the open circles in Fig. 6.9. The decay time shows a divergent behavior for pump powers approaching $I_p^{th} = 12{,}5\ mW$; for higher *Pump* powers, it exceeds the time window of our setup. To rule out non-linear effects and ensure we are in a linear-response regime with respect to the *Probe* intensity, we

have checked that the physics of interest is independent of the *Probe* pulse intensity: while some changes remain visible in the short-time dynamics, the long-time dynamics simply shows a global rescaling of the observed intensity.

The parametric nature of the enhanced life time is confirmed by the coincidence of the divergence with the signal emission energy jump, the frequency narrowing of the luminescence and the nonlinear increase of the signal emission at I_p^{th}.

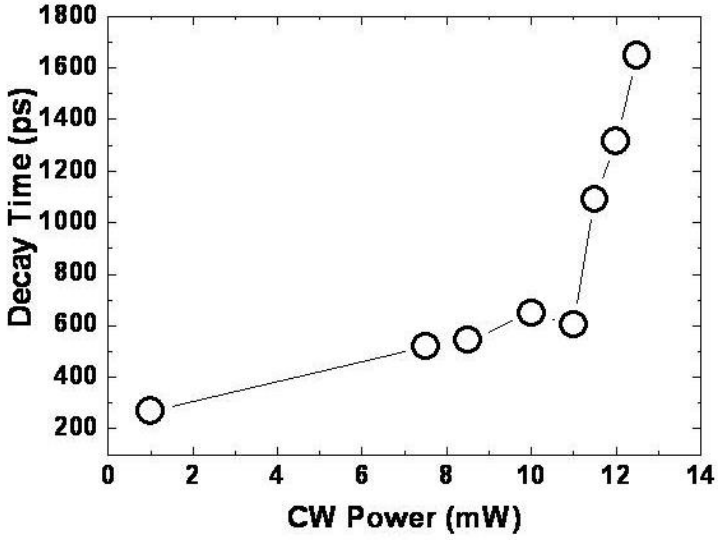

Fig. 6.9: Decay time of ΔI_s versus pump power I_p.

The role of the parametric processes is further evidenced by the momentum-resolved data shown in Fig. 6.10, in which the decay time of the signal emission is plotted as a function of the wavevector k_x. The considered wavevector range is centered on the value k_s where signal emission would appear if the *Pump* intensity was above threshold. While the decay time is a smooth function of k_x for I_p well below the parametric oscillation threshold (open circles), a marked peak is apparent in the vicinity of k_s $(k_x = 0)$ for *Pump* intensities around and above the threshold (full circles).

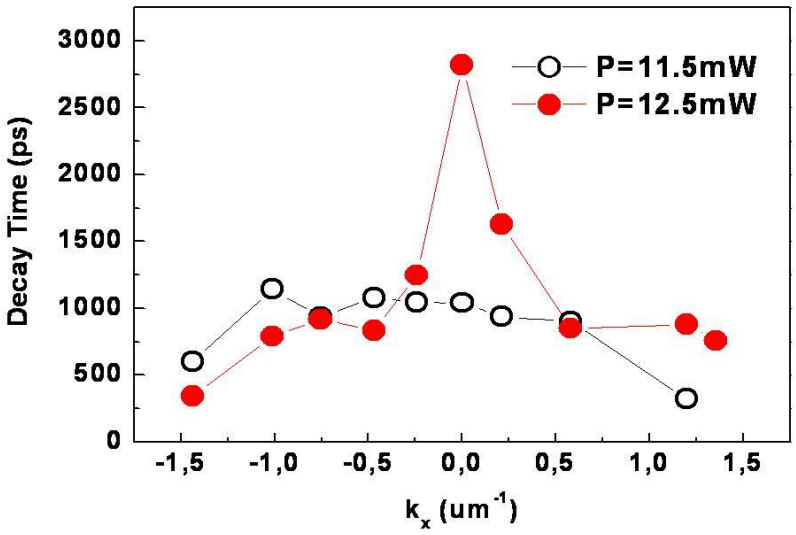

Fig. 6.10: k_x dependence of the signal decay time for two different pump powers, 11.5 mW (open circles) and 12.5 mW (full circles).

A convenient way to interpret the observed slowing down of the response to the probe is to use the coherent polariton model based on a pair of coupled Gross-Pitaevskii-like nonlinear wave equations for respectively the photon and exciton fields $\psi_{c,x}(\boldsymbol{r},t)$:(3, 64)

$$i\frac{\partial\psi_c}{\partial t} = \left(\omega_c(-i\nabla_{\mathrm{r}}) - i\frac{\gamma_c}{2}\right)\psi_c + \Omega_{\mathrm{R}}\psi_x + F(\boldsymbol{r},t)$$

$$i\frac{\partial\psi_x}{\partial t} = \left(\omega_x\psi_x - i\frac{\gamma_x}{2}\right)\psi_x + \Omega_{\mathrm{R}}\psi_c + g|\psi_x|^2\psi_x$$

We follow the dynamics of the system starting from the $\psi_{x,c}(\boldsymbol{r},t) = 0$ vacuum state. $\omega_c(k)$ is the photon dispersion, while the exciton dispersion is assumed to be flat at ω_x. $\gamma_{c,x}$ are the decay rates of the cavity-photon and the exciton, respectively. The exciton-exciton interactions are characterized by the nonlinear coupling coefficient g and Ω_{R} is the exciton-photon Rabi coupling. The driving $F(\boldsymbol{r},t)$ is proportional to the incident electromagnetic field and has to include both the *Pump* and the pulsed *Probe*: once the system has attained its stationary-state under the *Pump* only, an additional short *Probe* pulse is applied close to resonance with the idler. The following response of the system is monitored on the most relevant observables, in particular the polariton distribution in k-space. For the sake of simplicity, we have limited ourselves to the case of a plane-wave *Pump* with a well-defined wavevector k_p and periodic boundary conditions, while the finite spatial size of the *Probe* is fully taken into account.

As discussed in Ref. (53, 64), the approach to the OPO threshold from below is signaled by the decay rate of some mode tending to zero. As a function of k, the decay

time results then strongly peaked around the point where the decay rate is the smallest. These general claims are perfectly visible in the numerical result plotted in Fig. 6.11. For *Pump* intensities just below I_p^{th}, the evolution of the integrated signal emission ΔI_s after the arrival of the probe pulse is characterized by a short transient followed by a much slower exponential decay, with a time constant that dramatically increases as the threshold is approached (Fig. 6.11(a)). By comparing the overall decay time of the integrated ΔI_s (Fig. 6.11(b)) with the k-dependent decay time (Fig. 6.11(c)), it is immediate to see that the former is determined by the decay time of the longest-lived mode, a quantity that increases in magnitude and becomes progressively more peaked as the threshold is approached.

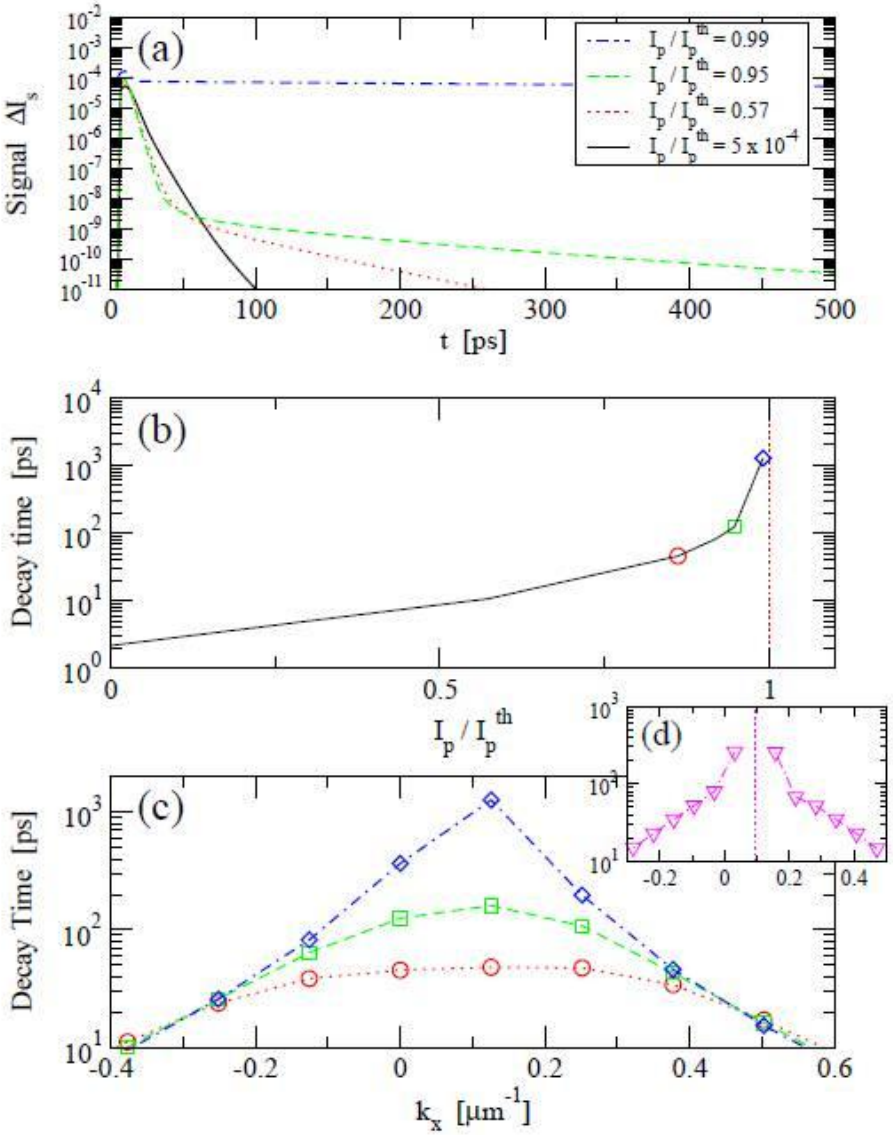

Fig. 6.11: Results of numerical calculations. Upper (a) panel: time dependence of k-integrated signal emission ΔI_s for different values of I_p; integration is performed over the k-space region surrounding k_s. Central (b) panel: decay time of ΔI_s as a function of the *Pump* intensity. Lower (c) panel: k-dependence of the decay rate for

different values of $I_p/I_p^{th} = 0.57,\ 0.95, 0.99$ below threshold. Inset (d): k-dependence of the decay time for $I_p/I_p^{th} = 1.15$, above threshold; the vertical dotted line indicates the coherent signal emission wavevector k_s, at which the decay time is infinite.

This theoretical result is in good agreement with the experimental observations for *Pump* intensities in the vicinity of the threshold, but some specific attention has to be paid at the experimental data for very low pump power. In this regime, the theoretical calculations predict that the decay time should go back to the bare polariton lifetime, while a quite long decay time is observed in the experiment, even well below the oscillation threshold and at wavevectors far from the signal emission. To explain this behavior, one can mention the spatial inhomogeneity of the system that smoothens the k-space distribution, as well as the presence of residual excitons that have accumulated into long-lived states and that relax down on a long time scale. Clearly, these incoherent scattering processes are most important for low pump powers, while coherent parametric processes take it over as the threshold is approached.

As we already mentioned, the decay time above threshold is too long to be quantitative measured with the present setup. Numerical simulations do not suffer from such a difficulty, and we summarize here the main features that one expects for this regime. As a consequence of the spontaneously broken U(1) symmetry, the spectrum of the elementary excitations is characterized by the presence of a soft Goldstone mode: as the wavevector $q = k - k_s$ of the excitation tends to zero, both its frequency and decay rate tend to zero.(41) This prediction is confirmed by the numerical results for the k-dependent decay rate that we show in Fig. 6.11(d): once again, the peaked structure of the decay rate as a function of $k - k_s$ is apparent.

6.8 – Summary

In this Chapter we have presented experimental results on the time-resolved PL in GaAs microcavities, at $\delta = 0$, under resonant excitation. Increasing the excitation power, strong optical nonlinearities appear in the k=0 emission due to the instabilities in the pump only solution and the onset of parametric oscillations between pump, signal and idler states. The emission from the signal is resolved in time and its momentum distribution is analyzed as a function of the *Pump* intensity: when I_p is close or above the parametric oscillation threshold, lifetimes orders of magnitude longer than the intrinsic polariton lifetime are observed for polariton modes in the

vicinity of the signal emission. The changes in the polariton dynamics are well described by a polariton Gross-Pitaevskii equation and in particular the long decay time is related to the appearance of a Goldstone mode in the excitation spectrum around the signal.

Bibliography:

1. Savvidis, P. G., Baumberg, J. J., Stevenson, R. M., Skolnick, M. S., Whittaker, D. M. & Roberts, J. S. (2000) *Phys. Rev. Lett.* **84,** 1547-1550.
2. Stevenson, R. M., Astratov, V. N., Skolnick, M. S., Whittaker, D. M., Emam-Ismail, M., Tartakovskii, A. I., Savvidis, P. G., Baumberg, J. J. & Roberts, J. S. (2000) *Phys. Rev. Lett.* **85,** 3680-3683.
3. Ciuti, C., Schwendimann, P. & Quattropani, A. (2003) *Semicond. Sci. Technol.* **18,** S279 - 293.
4. Ciuti, C., Schwendimann, P., Deveaud, B. & Quattropani, A. (2000) *Phys. Rev. B* **62,** R4825-R4828.
5. Stevenson, R. M., Astratov, V. N., Skolnick, M. S., Whittaker, D. M., Emam-Ismail, M., Tartakovskii, A. I., Savvidis, P. G., Baumberg, J. J. & Roberts, J. S. (2000) *Phys. Rev. Lett.* **85,** 3680.
6. Baumberg, J., Savvidis, P. G., Stevenson, R. M., Tartakovskii, A. I., Skolnick, M. S., Whittaker, D. M. & Roberts, J. S. (2000) *Phys. Rev. B* **62,** R16247-R16250.
7. Whittaker, D. M. (2001) *Phys. Rev. B* **63,** 193305.
8. Whittaker, D. M. (2005) *Phys. Rev. B* **71,** 115301-7.
9. Dang, L. S., Heger, D., André, R., BÅŧuf, F. & Romestain, R. (1998) *Phys. Rev. Lett.* **81,** 3920.
10. Senellart, P. & Bloch, J. (1999) *Phys. Rev. Lett.* **82,** 1233-1236.
11. Richard, M., Kasprzak, J., Romestain, R., Andre, R. & Dang, L. S. (2005) *Phys. Rev. Lett.* **94,** 187401.
12. Richard, M., Kasprzak, J., Andre, R., Romestain, R., Dang, L. S., Malpuech, G. & Kavokin, A. (2005) *Phys. Rev. B* **72,** 201301-4.
13. Kasprzak, J., Richard, M., Kundermann, S., Baas, A., Jeambrun, P., Keeling, J. M. J., Marchetti, F. M., Szymanska, M. H., André, R., Staehli, J. L., Savona, V., Littlewood, P. B., Deveaud, B. & Dang, L. S. (2006) *Nature* **443,** 409-14.
14. Deng, H., Press, D., Gotzinger, S., Solomon, G. S., Hey, R., Ploog, K. H. & Yamamoto, Y. (2006) *Phys. Rev. Lett.* **97,** 146402.
15. Balili, R., Hartwell, V., Snoke, D., Pfeiffer, L. & West, K. (2007) *Science* **316,** 1007.
16. Christopoulos, S., Baldassarri_Hoger_von_Hogersthal, G., A.J.D.Grundy, Lagoudakis, P. G., Kavokin, A. V., Baumberg, J. J., Christmann, G., Butte, R., Feltin, E., Carlin, J. F. & Grandjean, N. (2007) *Phys. Rev.Lett.* **98,** 126405.
17. Keeling, J., Marchetti, F. M., Szymanska, M. H. & Littlewood, P. B. (2007) *Semicond. Sci. Technol.* **22,** R1-26.
18. Sanvitto, D., Whittaker, D. M., Skolnick, M. S. & Roberts, J. S. (2005) *phys. stat. sol. (a)* **202,** 353.
19.

20. Shelykh, I. A., Vina, L., Kavokin, A. V., Galkin, N. G., Malpuech, G. & Andre, R. (2005) *Solid State Commun.* **135,** 1.
21. Balili, R., Hartwell, V., Snoke, D., Pfeiffer, L. & West, K. (2007) *Science* **316,** 1007-1010.
22. Keeling, J., Eastham, P. R., Szymanska, M. H. & Littlewood, P. B. (2004) *Phys. Rev. Lett.* **93,** 226403.
23. Boeuf, F., André, R., Romestain, R., Dang, L. S., Péronne, E., Lampin, J. F., Hulin, D. & Alexandrou, A. (2000) *Phys. Rev. B* **62,** R2279-R2282.
24. Alexandrou, A., Bianchi, G., Péronne, E., B. Hallé, F. Boeuf, André, R., Romestain, R. & Dang, L. S. (2001) *Phys. Rev. B* **64,** 233318.
25. Senellart, P., Bloch, J., Sermage, B. & Marzin, J. Y. (2000) *Phys. Rev. B* **62,** R16263-R16266.
26. Huang, R., Tassone, F. & Yamamoto, Y. (2000) *Phys. Rev. B* **61,** R7854.
27. Christopoulos, S., Baldassarri Höger von Högersthal, G., Grundy, A. J. D., Lagoudakis, P. G., Kavokin, A. V. & Baumberg, J. J. (2007) *Phys. Rev. Lett.* **98,** 126405.
28. Bajoni, D., Senellart, P., Lemaître, A. & Bloch, J. (2007) *Phys. Rev. B* **76,** 201305(R).
29. Rubo, Y. G. (2007) *Phys. Rev. Lett.* **99,** 106401.
30. Lagoudakis, K. G., Wouters, M., Richard, M., Baas, A., Carusotto, I., André, R., Dang, L. S. & Deveaud-Plédran, B. (2008) *Nature Physics* **4,** 706.
31. Amo, A., Sanvitto, D., Ballarini, D., Laussy, F. P., Del Valle, E., Martin, M. D., Lemaitre, A., Bloch, J., Krizhanovskii, D. N., Skolnick, M. S., Tejedor, C. & Vina, L. (2007) *arXiv:0711.1539v1*.
32. Savvidis, P. G., Baumberg, J. J., Stevenson, R. M., Skolnick, M. S., Whittaker, D. M. & Roberts, J. S. (2000) *Physical Review Letters* **84,** 1547 LP - 1550.
33. Savvidis, P. G., Baumberg, J. J., Stevenson, R. M., Skolnick, M. S., Whittaker, D. M. & Roberts, J. S. (2000) *Phys. Rev. B* **62,** R13278.
34. Messin, G., Karr, J. P., Baas, A., Khitrova, G., Houdré, R., Stanley, R. P., Oesterle, U. & Giacobino, E. (2001) *Phys. Rev. Lett.* **87,** 127403.
35. Baumberg, J. J., Savvidis, P. G., Stevenson, R. M., Tartakovskii, A. I., Skolnick, M. S., Whittaker, D. M. & Roberts, J. S. (2000) *Phys. Rev. B* **62,** R16247.
36. Saba, M., Ciuti, C., Bloch, J., Thierry-Mieg, V., Andre, R., Dang, L. S., Kundermann, S., Mura, A., Bongiovanni, G., Staehli, J. L. & Deveaud, B. (2001) *Nature* **414,** 731.
37. Baas, A., Karr, J.-P., Romanelli, M., Bramati, A. & Giacobino, E. (2006) *Phys. Rev. Lett.* **96,** 176401.
38. Romanelli, M., Leyder, C., Karr, J. P., Giacobino, E. & Bramati, A. (2005) *arXiv:0505639 v2*.
39. Savasta, S., Di Stefano, O., Savona, V. & Langbein, W. (2005) *Phys. Rev. Lett.* **94,** 246401.
40. Krizhanovskii, D. N., Sanvitto, D., Love, A. P. D., Skolnick, M. S., Whittaker, D. M. & Roberts, J. S. (2006) *Phys. Rev. Lett.* **97,** 097402.
41. Wouters, M. & Carusotto, I. (2007) *Phys. Rev. A* **76,** 043807-9.
42. Wouters, M. & Carusotto, I. (2007) *Phys. Rev. Lett.* **99,** 140402-4.
43. Baumberg, J. J. & Lagoudakis, P. G. (2005) *phys. stat. sol. (b)* **242,** 2210-2223.
44. Carusotto, I. & Ciuti, C. (2004) *Phys. Rev. Lett.* **93,** 166401.
45. Freixanet, T., Sermage, B., Bloch, J., Marzin, J. Y. & Planel, R. (1999) *Phys. Rev. B* **60,** 8509-8512.
46. Houdré, R., Weisbuch, C., Stanley, R. P., Oesterle, U. & Ilegems, M. (2000) *Phys. Rev. B* **61,** R13333.
47. Deveaud, B. (2005) *Special Issue: Physics of Semiconductor Microcavities* (volume **242** (11) of Phys. Stat. Sol. (b).
48. Carusotto, I., Wouters, M. & Ciuti, C. (2007) *J. Low Temp Phys* **148,** 459-464.
49. Sermage, B., Malpuech, G., Kavokin, A. V. & Thierry-Mieg, V. (2001) *Phys. Rev. B* **64,** 081303.

50. Freixanet, T., Sermage, B., Tiberj, A. & Planel, R. (2000) *Phys. Rev. B* **61,** 7233 - 7236.
51. Langbein, W., Shelykh, I., Solnyshkov, D., Malpuech, G., Rubo, Y. G. & Kavokin, A. (2007) *Phys. Rev. B* **75,** 075323.
52. Amo, A., Sanvitto, D., Ballarini, D., Laussy, F. P., Del Valle, E., Martin, M. D., Lemaitre, A., Bloch, J., Krizhanovskii, D. N., Skolnick, M. S., Tejedor, C. & Vina, L. (2007) *arXiv:0711.1539v1 [cond-mat.mes-hall]*.
53. Wouters, M. & Carusotto, I. (2007) *Phys. Rev. B* **75,** 075332-12.
54. Ciuti, C., Savona, V., Piermarocchi, C. & Quattropani, A. (1998) *Physical Review B* **58,** 7926.
55. Ciuti, C., Savona, V., Piermarocchi, C., Quattropani, A. & Schwendimann, P. (1998) *Phys. Rev. B* **58,** R10123-R10126.
56. Baumberg, J. J. & Viña (editors), L. (2003) *Special Issue on microcavities* (volume **18** (10) of Semiconductor Science and Technology.
57. Baas, A., Karr, J. P., Romanelli, M., Bramati, A. & Giacobino, E. (2004) *Phys. Rev. B* **70,** 161307.
58. Skolnick, M. S., Sanvitto, D., Krizhanovskii, D. N., Love, A. P. D., Whittaker, D. M. & Roberts, J. S. (2006) *physica status solidi (b)* **243,** 3741.
59. D. Pines and P. Nozieres (1966) *The Theory of Quantum Liquids* (Vols. 1 and 2 (Addison-Wesley, Redwood City).
60. Pitaevskii, L. & Stringari, S. (2003) *Bose Einstein Condensation* ((Oxford University Press, Oxford).
61. Deng, H., Solomon, G. S., Hey, R., Ploog, K. & Yamamoto, Y. (2007) *Phys. Rev. Lett.* **99,** 126403.
62. Wouters, M., Carusotto, I. & Ciuti, C. (2008) *Phys. Rev. B* **77,** 115340.
63. Huynh, A., Tignon, J., Larsson, O., Roussignol, P., Delalande, C., André, R., Romestain, R. & Dang, L. S. (2003) *Phys. Rev. Lett.* **90,** 106401.
64. Ciuti, C. & Carusotto, I. (2005) *phys. stat. sol. (b)* **242,** 2224-2245.

Chapter 7

General conclusions

We have presented a wide study of the polariton dynamics and many-body physics in semiconductor planar microcavities by means of time-resolved photoluminescence spectroscopy. We will now summarize the main results.

Non resonant experiments

The polariton dynamics is studied as a function of the polariton density and in particular the polarization properties have been analyzed in CdTe- and GaAs- based samples.

- CdTe-based microcavities

The linear polarization degree of the emission from $k = 0$ has been studied under non-resonant linear polarized excitation. At low excitation density the linear polarization degree of the emission is frozen (lifetime longer than $2\ \mathrm{ns}$) at a constant value of $\wp_{lin} = -0.3$. At higher excitation densities, stimulated scattering accelerates the polariton dynamics and increases the polarization degree ($\wp_{lin} = -0.5$). The stimulated scattering takes place in the strong coupling regime, since higher excitation powers are required to reach the transition to the weak coupling regime. The linear polarization is pinned along one of the crystallographic axis of the structure and it is independent on the orientation of the linear polarization of the exciting beam.

- GaAs-based microcavities

In semiconductor GaAs based microcavities, under non-resonant excitation and low temperature, the light emission properties are greatly determined by the excitation density. The exciton-exciton interactions lead to a renormalization of the polariton energies: the emission energy of the LPB from $k = 0$ shows a blueshift with increasing the excitation intensity, and eventually the system undergoes a transition to the weak-coupling regime. The threshold is determined by a critical density of polaritons, which in GaAs samples is always smaller than that required to activate the stimulated scattering. Under circular polarized excitation, two different polariton populations with opposite spin are present, and, if one population is bigger than the other, the renormalization effects are stronger for the majority polariton population. The emission energies of the polarized polaritons, and consequently their coupling regime, are determined by the occupation factor of the polaritons with a given spin, due to the different carriers distributions for each spin orientation and to phase space filling effects.

The spatial distribution of the strong- to weak-coupling transition shows that high density phases of polaritons accumulate in islands non-uniformly distributed all over the laser excited area, and that strong- and weak-coupled polaritons coexist within regions smaller than 10 μm.

Resonant experiments

- GaAs-based microcavities

Non-equilibrium effects and quasi-particle interactions complicate the theoretical description of the high density phase of polaritons under resonant pumping, but, on the other side, fundamental new physics can be investigated under such conditions. The most important many body effects in microcavities are related to the bosonic nature of polaritons, which manifests itself in the spontaneous appearance of long-range order, Bose-Einstein condensation and quantum hydrodynamics effects such as superfluidity or vortices. Many of these properties are related to the excitation spectrum on the top of the high density phase of polaritons.

We presented a novel experimental configuration which allows for the observation of the excitation spectrum of the steady state of an optical parametric oscillator. The excitation is performed with a cw laser at resonance with the LPB in order to observe the OPO formation for high enough pump intensities. A probe pulse, set near resonance with the idler state, produce a perturbation that is observed

through the signal state emission. The response of the system in its stationary state to a weak probe perturbation provides information about the decay time of the excited states.

A strong slowing down of the dynamics is observed as the excitation power approaches the threshold for the switching-on of the OPO, and the decay time can become orders of magnitude longer than the typical life time of polaritons. Good agreement between the experimental results and the theoretical model based on the generalized polariton Gross-Pitaevskii equation is found. In particular, the changes in the polariton dynamics are related with the behavior of the imaginary part of a Goldstone mode in the excitation spectrum on the top of a high density phase of polaritons, and support the theoretical description of polariton OPO as an example of spontaneous symmetry breaking.

Conclusiones generales

Hemos presentado un amplio estudio de la dinámica de polaritones y física de muchos cuerpos en microcavidades semiconductoras planares por medio de espectroscopia de fotoluminiscencia resuelta en tiempo.

Experimentos no resonantes

Hemos estudiado la dinámica de polaritones en función de la densidad de polaritones y en particular hemos analizado las propiedades de la polarización de la emisión de la luz en muestras basadas en CdTe y GaAs.

- Microcavidades basadas en CdTe

Se ha estudiado el grado de polarización lineal de la emisión desde $k = 0$ bajo excitación no-resonante linealmente polarizada. A bajas densidades de excitación el grado de polarización lineal de la emisión está congelado (tiempo de vida más largo que 2 ns) a un valor constante de $\wp_{lin} = -0.3$. A densidades de excitación mayors, el "scattering" estimulado acelera la dinámica de los polaritones y aumenta el grado de polarización ($\wp_{lin} = -0.5$). El "scattering" estimulado tiene lugar en el régimen de acoplamiento fuerte, dado que se requieren potencias de excitación mayores para alcanzar la transición al acoplamiento débil. La polarización lineal se ancla a lo largo de un eje cristalográfico de la estructura y es independiente de la orientación de la polarización lineal del haz de excitación.

- Microcavidades basadas en GaAs

En microcavidades basadas en GaAs, bajo excitación no-resonante y a bajas temperaturas, las propiedades de la emisión de luz se vem fuertemente determinadas por la densidad de excitación. Las interacciones excitón-excitón llevan a la

renormalización de las energías de los polaritones: la energía de emisión de la rama polaritónica inferior desde $k = 0$ muestra un corrimiento hacia el azul al aumentar la intensidad de excitación y finalmente el sistema sufre una transición al régimen de acoplamiento débil. El umbral está determinado por una densidad crítica de polaritones que en muestras de GaAs es siempre menor que la que se requiere para activar el "scattering" estimulado. Bajo excitación polarizada circularmente, dos poblaciones de polaritones diferentes con spin opuestos están presente, y, si una de las poblaciones es mayor que la otra, los efectos de renormalización son más fuertes para la población de polaritones mayoritaria. Las energía de emisión de los polaritones polarizados, y consecuentemente su régimen de acoplamiento, están determinadas por los factores de ocupación de los polaritones con un spin determinado, debido a las diferentes distribuciones de los portadores para cada una de las orientaciones de spin y a efectos de llenado de fase.

La distribución especial de la emisión en la transición del régimen de acoplamiento fuerte al débil muestra que las fases de alta densidad de los polaritones se acumulan en islas no distribuidas uniformemente a lo largo del área excitada por el láser, y que polaritones acoplados fuertemente coexisten con otros acoplados débilmente en regiones menores que 10 µm.

Experimentos resonantes

- Microcavidades basadas en GaAs

Efectos de no-equilibrio e interacciones entre las cuasi-partículas complican la descripción teórica de la fase de alta densidad de polaritones bajo bombeo resonante, sin embargo, por otra parte, es posible investigar nuevos aspectos fundamentales de la física de los polaritones bajo estas condiciones. Los efectos de muchos cuerpos más importantes en microcavidades están relacionados con la naturaleza bosónica de los polaritones que se manifiestan en la aparición espontánea de orden de largo alcance, condensación de Bose-Eisntein y efectos hidrodinámicos cuánticos tales como superfluidez y vórtices. Muchas de estas propiedades están relacionadas con el espectro de excitaciones generadas en la fase de alta densidad de los polaritones.

Hemos presentado una nueva configuración experimental que permite la observación del espectro de excitación del estado estacionario de un oscilador paramétrico óptico (OPO). La excitación se realiza con un láser continuo en resonancia con la rama polaritónica inferior para poder observar la formación del OPO con intensidades de bombeo suficientemente altas. Un pulso de prueba, situado en resonancia con el estado inactivo (en inglés "idler"), produce una perturbación que se

observa a través de la emisión del estado señal (en inglés “signal”). La respuesta del sistema en su estado estacionario a una perturbación pequeña (prueba) da información acerca del tiempo de decaimiento de los estados excitados.

Hemos observado una fuerte desaceleración de la dinámica cuando la potencia de excitación se acerca al umbral del encendido del OPO, y que los tiempos de decaimiento pueden llegar a ser órdenes de magnitud mayores que el tiempo de vida típico de los polaritones. Hemos encontrado un buen acuerdo entre los resultados experimentales y el modelo teórico basado en la ecuación generalizada de Gross-Pitaevskii para polaritones. En particular, hemos visto que los cambios en la dinámica de los polaritons están relacionados con la parte imaginaria de un modo de Goldstone en el espectro de excitación sobre una fase de polaritones de alta densidad y que éstos ratifican la descripción teórica de un OPO de polaritones como un ejemplo de rotura de simetría espontánea